POLITECNICO
MILANO 1863

Attosecond dynamics in molecules: Theoretical and experimental study of a bio-molecular source

Supervisors:
Prof. Mauro NISOLI
Prof. Fabrizio GIORGIS
Co-Supervisors:
Dr. Rocío BORREGO VARILLAS

Author:
Daniele MOCCI
Student ID: *942287*

Master degree in Physics Engineering
Photonics and Nano Optics

Academic year 2020-2021

The truth. It is a beautiful and terrible thing, and should therefore be treated with great caution.

J.K. Rowling

Attosecond dynamics in molecules

Theoretical and experimental study of a bio-molecular source

Daniele Mocci

Abstract

Attosecond pulses ($1\ as = 10^{-18}s$) can be exploited to monitor and control the electron motion inside atoms, molecules or solids. In particular, triggering photoinduced electron transfer and charge transfer processes in molecules has a growing interest for potential applications in optoelectronic and biochemistry. Pioneering works in this field exploited two color laser pulses: a first attosecond Extreme Ultraviolet (XUV) pulse behaved as a pump pulse and a delayed infrared (IR) femtosecond pulse ($1\ fs = 10^{-15}s$), acting as a probe, shaped the electron localization in H_2 and D_2 molecules. The astonishing results paved the way toward more complex structures that culminate with the electronic control in phenylalanine in a pump-probe experiment. However, many outstanding questions remain to be resolved, among which the interaction between the analyte, typically in the gas phase, and the short laser pulses. In fact, one of the major difficulties for extending attosecond spectroscopy towards complex molecules concerns their generation in the gas phase. Due to the low photon flux of XUV pulses, the detection of the charged particles requires a considerable density of target molecules: current experimental setups, based on supersonic gas valves, are yet to produce satisfactory amount to conduct a sound analysis.

The main purpose of this work is to characterize the bio-molecular source present in the ELYCHE (ELectron-scale dYnamics in CHEmistry) laboratory, highlighting its strengths and deficiencies compared to analogous setups. The core of the work aims at interconnecting the experimental performances with a sound theoretical background based on the Direct Simulation Monte-carlo (DSMC) software, which allow us to understand the origin of the limitations related to the gas valve.
In particular, this thesis is organized as follows:

- In the first chapter, a brief review of the attosecond dynamics in molecules in the gas phase is presented, specifying the choice of the observables and the related techniques.
- In the second and third chapter, after having outlined the main gas sources for attosecond applications, the experimental setup is described in its main traits.
- In the fourth chapter, the experimental characterization of the gas source is presented, drawing meaningful conclusions.
- In the fifth chapter the base of the DSMC theory is briefly analyzed, focusing on the most common models and choices that will be later used.

- The sixth chapter regards the actual implementation and study of the simulation, aimed at modeling the gas source. This analysis, which represents the central part of the work, ends with an attempt of solution.
- The last chapter shows the experimental proof of the previous theoretical simulations.

It will be shown that instead of focusing on changing the downstream parameters of the setup, it would be better to shape in a different way the nozzle sources, although it is not as direct as it may appear.

Attosecond dynamics in molecules

Theoretical and experimental study of a bio-molecular source

Daniele Mocci

Sommario

Gli impulsi ad attosecondi ($1\ as = 10^{-18}s$) possono essere utilizzati per monitorare e controllare il moto elettronico all'interno di atomi, molecole o solidi. In particolare, l'attivazione di tali trasporti elettronici foto-indotti ha un interesse crescente per potenziali applicazioni in ambito opto-elettronico e biochimico. Studi pioneristici in questo campo hanno utilizzato impulsi laser a due colori: il primo, nell'Estremo Ultravioletto (XUV), come impulso di pompa, mentre il secondo, nell'infrarosso (IR) e della durata di qualche femtosecondo ($1\ fs = 10^{-15}s$), come impulso sonda. Tali studi sono stati condotti su molecole di idrogeno (H_2 e isotopo D_2) e hanno consentito il controllo del moto elettronico. Si tratta di risultati sorprendenti precursori nello studio di molecole più complesse il cui culmine, allo stato dell'arte, è rappresentato dal controllo elettronico nella molecola di fenilalanina. Rimangono, tuttavia, numerosi problemi da risolvere, tra i quali, di primaria rilevanza per questo studio, l'interazione tra l'analita, tipicamente in fase gassosa, ed i brevi impulsi laser. Una delle maggiori difficoltà per estendere la spettroscopia ad attosecondi verso molecole più complesse riguarda, infatti, la loro generazione in fase gassosa. A causa del basso flusso di fotoni nell'XUV, il rilevamento di molecole cariche necessita di un'elevata densità della molecola target. Gli odierni setup sperimentali, basati su valvole a gas supersoniche, sono ben lontani dal generare i flussi adatti a condurre una solida analisi.

Il principale obiettivo di questo lavoro di tesi è quello di caratterizzare la sorgente bio-molecolare presente nel laboratorio ELYCHE (ELectron-scale dYnamics in CHEmistry), mettendo in evidenza i punti di forza e le principali carenze, comparati ad analoghi setup. La parte centrale del lavoro ha come obiettivo quello di collegare le performance sperimentali con una solida base teorica modellata sul metodo *Direct Simulation Monte-carlo (DSMC) software*, che permette di capire le origini di tali limiti. In particolare, la tesi è organizzata come segue:

- Nel primo capitolo, viene presentato un breve riassunto delle dinamiche ad attosecondi in molecole in fase gassosa, specificando la scelta delle osservabili legate a queste tecniche.
- Nel secondo e terzo capitolo, dopo aver descritto le principali sorgenti gassose per applicazioni ad attosecondi, viene illustrato il setup sperimentale nei suoi tratti principali.
- Nel quarto capitolo, viene presentata la caratterizzazione sperimentale della sorgente gassosa, traendo le principali conclusioni.

- Nel quinto capitolo, viene brevemente descritta la teoria DSMC, analizzando i principali modelli e descrivendo le scelte utilizzate successivamente.
- Il sesto capitolo riguarda l'implementazione e lo studio di varie simulazioni, atti a modellizzare la sorgente gassosa. Tale analisi, che rappresenta il fulcro del lavoro, propone un tentativo di soluzione.
- Nell'ultimo capitolo, la prova sperimentale della precedente simulazione teorica viene implementata.

Il lavoro mette in evidenza come sia strettamente necessario cambiare i parametri del setup sperimentale a monte dell'interazione laser, in modo tale da modellare diversamente la sorgente bio-molecolare.

Acknowledgments

I am infinitely grateful to prof. Mauro Nisoli for giving me the opportunity to enter the Attosecond laboratory and learn part of this new reality, to Dr. Rocío Borrego Varillas for her assistance in writing my thesis and all the support during the time spent in the laboratory, to Dr. Matteo Lucchini for his continuous supervision and his valuable advice.

I truly thank you all the students that work in the laboratory for having shared their knowledge with me and having welcomed me. In particular, Yingxuan and Federico for their continuous support, help and encouragement.

I thank you very much my mom and dad, who supported me during all these years in any occasion, together with my sister Paola and my brother Stefano with which I share a sincere friendship and brotherhood: without my family, this journey would not have even started. I need to mention my beautiful Nonna, who left me too soon at the beginning of this journey, but who loved me until the end.

I thank you all my friends, both the "historical" ones that I know since my childhood and adolescence, those that I met at the university here in Milano and those friends that are the most recent but have changed my life for the better. In particular, a huge thanks to Virginia, my university mate with whom I shared all the anxieties, joys, the study days and the evenings playing. I thank Iacopo, for his psychological and tech support, in particular for the help in running my simulations. I cannot fail to mention my closest friends group: Abishekh, Diego, Federico, Gabriele, Giovanni that I know since my childhood; Chiara, Claudia, Stefania and Daniela who have always been there for ten years.

Dulcis in fundo, a special thank you to Thomas, who has supported, encouraged, helped, listened to me and believed in me more than anyone else. Always.

Contents

List of Figures

Chapter 1

Introduction

With the introduction of photography in the late 1800s, it was possible to explore dynamics that previously were forbidden due to the limited time resolution of human eyes and brain processing: the most famous example is the portrayal of the horse galloping [28]. Moving forward in time, with the advent of the laser a new era begins: relying on similar principle, short laser pulses allowed the investigation of ultrafast molecular dynamics that characterize chemistry, exploiting femtosecond pulses ($1\ fs = 10^{-15}s$) [39]. Though this technique is a well-established discipline, it is limited to only part of molecular processes that could be considered "slow"compared to certain dynamics. The electronic motion cannot be investigated through femtosecond pulses due to their extremely high speed, therefore shorter laser pulses are required. In the last decades, thanks to the scientific and technological development, attosecond laser pulses ($1\ as = 10^{-18}s$) opened the door to a new branch of physics, able to investigate extremely high speed processes with the required time resolution. To understand this statement, it is necessary to underline the close relationship between the "quantum motion"and the coherent superpositions of states. If we consider two stationary generic states $|u_1\rangle$ and $|u_2\rangle$, with energy E_1 and E_2 respectively the time dependent wavefunction for the single state can be written as

$$|\psi_1\rangle = |u_1\rangle\, e^{-i\omega_1 t}$$

where $\omega = \frac{E_1}{\hbar}$ is the frequency and $\hbar = 6.582 \cdot 10^{-16} eV \cdot s$ is the reduced Planck constant. An analogous expression holds for the time dependent state $|\psi_2\rangle$. If the system is in one of these two stationary states, the probability density function (proportional to $|\Psi|^2$) is not time dependent. A quantum superposition between two stationary states is sufficient to generate a time dependence in the probability density function. In fact, let's assume that these two states generate a coherent superposition, the global wavefunction reads as:

$$|\psi\rangle = c_1\, |u_1\rangle\, e^{-i\omega_1 t} + c_2\, |u_2\rangle\, e^{-i\omega_2 t}$$

the physical observables, as mentioned, are related to the density function which is proportional to the $|\Psi|^2$, which in this simple case is:

$$|\Psi|^2 = \langle\Psi|\Psi\rangle = (c_1^*\, \langle u_1|\, e^{i\omega_1 t} + c_2^*\, \langle u_2|\, e^{i\omega_2 t}) \cdot (c_1\, |u_1\rangle\, e^{-i\omega_1 t} + c_2\, |u_2\rangle\, e^{-i\omega_2 t}) =$$

$$= |c_1|^2|u_1|^2 + |c_2|^2|u_2|^2 + 2\,\mathrm{Re}\{c_1^* c_2 u_1^* u_2 e^{-i(\omega_2-\omega_1)t}\}$$

Hence, if c_1 and c_2 are time independent, the first two terms are time independent too, while the last one is oscillating with a frequency related to the difference in energy between the two involved states. The period of oscillation is:

$$T = \frac{2\pi\hbar}{|E_1 - E_2|}$$

Increasing the energy gap between the states, the period of oscillation will decrease: by specifying these two states, it is possible to have an estimation of the order of magnitude of relevant physical phenomena. For example, the energy gap between two vibrational levels is $\Delta E \approx 100\ meV$, thus producing an oscillation period in the order of 40 fs. For valence electrons with energy separation in the order of $\Delta E \approx 10\ eV$, the period $T \approx 400\ as$; this value decreases inasmuch one considers core electrons. Thus, it is clear that, in order to investigate the electronic motion, attosecond pulses are required. Amidst the variety of application of the attosecond techniques, the electronic motion in large molecules is one of the main challenging topics. Such experiments, require the molecules to be in the gas phase in order to interact with the short laser pulses. In order to balance the low photon flux density, a large amount of analyte is coveted, though its production and handling requires further improvements.
In this chapter, I will review the fundamentals of attosecond spectroscopy and will present the main bottlenecks of these techniques.

1.1 Steps towards Attosecond Science

The most common technique for the generation of single attosecond pulses (SAP) or trains of attosecond pulses (TAP) employs short pulses in the infrared (IR) region, typically coming from commonly available femtosecond lasers, which are now a very stable and durable technology.
The core physical phenomenon is the *High Order Harmonic Generation* process (HHG) [23], which involves the generation of a broad light spectrum due the extreme non-linear response of a gas medium following its interaction with a short and intense IR laser pulse. Typically, the resultant spectrum presents three regions: a first one in which the intensity of the harmonics drops sharply, an intermediate region in which the harmonics' intensity is almost constant (plateau) and finally a region of cutoff in which the harmonic intensity drops to zero. It is worth noticing that the usual gas media, in which this phenomenon is observed, are noble gasses which are characterized by being *centro-symmetric*: the polarization P can be expanded in series as a function of the electric field E and it contains only the odd terms of the electric susceptibility $\chi^{(i)}$

$$P = \epsilon_0 \left(\chi^{(1)}E + \chi^{(3)}E^3 + \chi^{(5)}E^5 + ...\right) \tag{1.1.1}$$

Following this condition, only the odd harmonics of the fundamental are produced. Though intrinsically quantistic, this phenomenon can be outlined through a semi-classical model which gives the taste of a solution in spite of being formally inaccurate. This model is divided into three steps, under two substantial assumptions:

- *Single Active electron*: the electric field interacts with only one electron, coming from the ionization process.
- *Strong Field approximation*: once emitted, the free electron is subject to the external field only.

Let's consider a femtosecond laser pulse which is impinged into a gas medium: its electric field modifies the potential that the external electrons are experiencing. The first step corresponds to the tunneling of such electron due to the lowering of the potential barrier in correspondence of the peak of the external electric field, as depicted in fig. 1.1.1 A. This initial stage is thus a purely quantum effect: the electron tunneling through a potential barrier.
After the ionization, the unbounded electron is moving in the continuum, but still its motion is shaped by the external electric field (fig. 1.1.1 B): when it changes sign it modifies the electron trajectory by reversing its motion, carrying it close to the parent ion. As a first order approximation, this phenomenon can be described classically through the Newton's law.
The last step corresponds to the re-collision of the unbounded electron with the parent ion: if it has acquired sufficient kinetic energy in the continuum it can release it in form of high-energy photons of short duration (fig. 1.1.1 C).

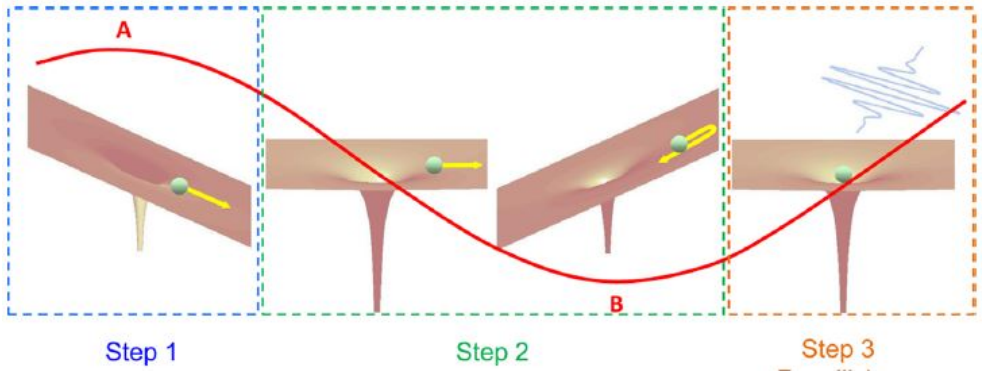

Figure 1.1.1: Schematic representation of the Three step model for Attosecond pulse generation. This process repeats every half period, resulting in a train of attosecond pulses, figure adapted from [23].

This three-step model is repeated every half optical cycle: without any precautions it leads to the generation of a train of attosecond pulses (TAP). More detailed models exist, but for the scope of this work this semi-classical approach is sufficient and thus it will be briefly analyzed.

First Step: Ionization

This first step can be described only by a pure quantum approach, since it is involving the tunneling of a particle through a potential barrier, nevertheless by comparing the frequency of the impinging radiation ω_0 with the "tunneling time "τ_t it is possible to predict whether the potential barrier is stationary or not:

- If $\tau_t \lll 1/\omega_0$ the potential barrier is stationary during tunneling,
- If $\tau_t \ggg 1/\omega_0$ the potential barrier is oscillating, producing a multi-photon ionization.

In reality, these two regimes mix up. In the following, after this phase we will consider the electron to be ionized by the atom.

Second Step: Motion after ionization

After ionization, the classical picture depicts the electron as a particle under the effect of an external electric field. Let's assume that the electron is ionized with a final velocity $\boldsymbol{v}_0 = 0$ (i.e., the impinging electric field has given the electron the exact energy to be in the continuum) and the external electric field is monochromatic with frequency ω_0 and amplitude E_0, furthermore it is polarized along the x direction ($\boldsymbol{u}_x$). Thus, the external electric field can be written as:

$$\boldsymbol{E}(t) = E_0 \cos(\omega_0 t)\ \boldsymbol{u}_x \tag{1.1.2}$$

Following the second Newton law, the electron, with mass m, satisfies the following equation:

$$m\boldsymbol{a} = \boldsymbol{F} = -e\boldsymbol{E}(t) \tag{1.1.3}$$

where $\boldsymbol{a}$ is the acceleration and $e \approx 1.602 \cdot 10^{-19} C$ is the electric charge.
By integrating this equation from the instant t_0, corresponding to the instant of ionization, to a generic instant t one obtains:

$$\boldsymbol{v}(t) - \boldsymbol{v}(t_0) = -\frac{eE_0}{m\omega_0}[sin(\omega_0 t) - sin(\omega_0 t_0)]\boldsymbol{u}_x \tag{1.1.4}$$

where $\boldsymbol{v}$ is the electron velocity and by assumption $\boldsymbol{v}(t_0) = \boldsymbol{0}$. By integrating the following expression, it leads to:

$$x(t) - x(t_0) = \frac{eE_0}{m\omega_0^2}[cos(\omega_0 t) - cos(\omega_0 t_0) + \omega_0(t - t_0)sin(\omega_0 t_0)] \tag{1.1.5}$$

To simplify this expression one can choose $x(t_0) = 0$, corresponding to the center of the parent ion. This equation is just along the x direction, due to the fact that the electric field is polarized along the x direction, thus to calculate the instant of recombination between the electron and the ion, it is sufficient to ask for t such that $x(t) = 0$. Even though it may appear easy to solve, this equation does not have an analytic solution but two constraints on the instant of ionization can be found:

$$0 \leq t_0 \leq \frac{4\pi}{9\omega_0}$$

and

$$\frac{\pi}{\omega_0} \leq t_0 \leq \frac{13\pi}{9\omega_0}$$

Calculating the solution numerically, it is possible to fit the following expression

$$\frac{t}{T_0} = \frac{1}{4} - \frac{3}{2\pi} sin^{-1}\left(\frac{4\ t_0}{T_0} - 1\right) \tag{1.1.6}$$

where $T_0 = 2\pi/\omega_0$ is the period of oscillation of the electric field. It is interesting to notice that the recombination instant t is determined uniquely by the ionization instant t_0: upon increasing t_0, the recombination instant decreases and the velocity acquired by the ionized electron varies, according to eq 1.1.4, leading to different properties in the recollision step. For example, if $t_0 = 0$, following eqn. 1.1.6, $t = T_0$ and substituting in eqn. 1.1.4, one gets $\boldsymbol{v}(t) = \boldsymbol{0}$. In other words, short ionization time corresponds to long recombination time, while long ionization time corresponds to short recombination time. This behaviour is shown in fig. 1.1.2.

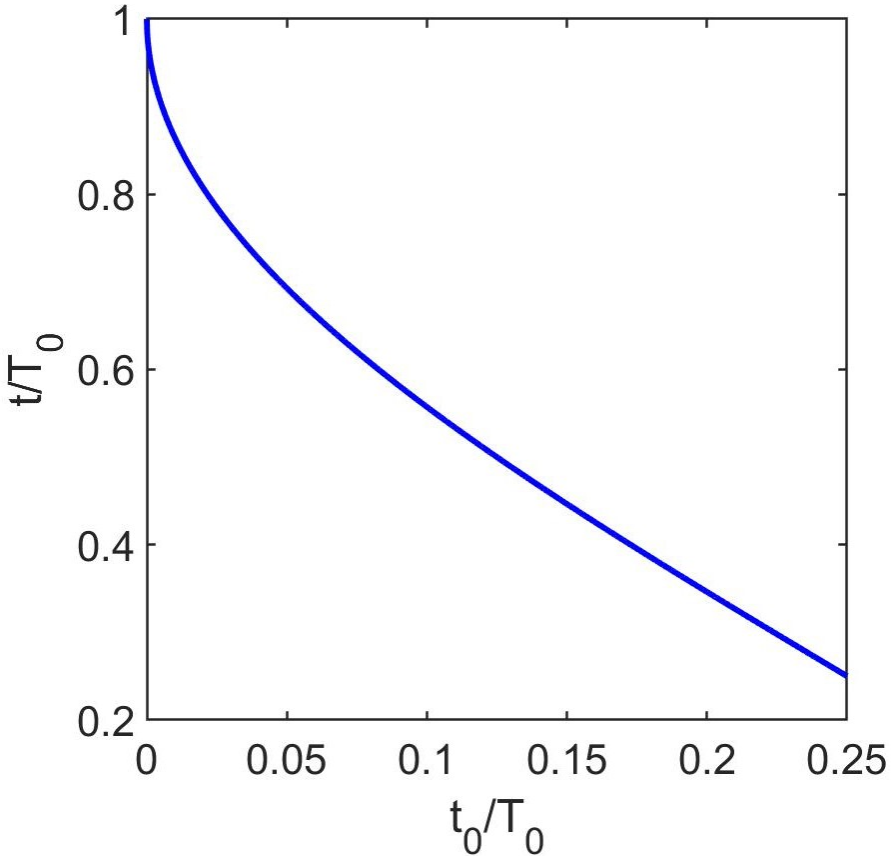

Figure 1.1.2: Recollision time (t), normalized over the period of oscillation T_0, as a function of the ionization time t_0, normalized over T_0, [23]

Hence, it is interesting to understand with how much kinetic energy the electron will recollide with the parent ion:

$$E_k = \frac{1}{2}mv(t)^2 = \frac{1}{2}m\left(\frac{eE_0}{m\omega_0}\right)^2[sin(\omega_0 t) - sin(\omega_0 t_0)]^2 = 2U_p[sin(\omega_0 t) - sin(\omega_0 t_0)]^2 \tag{1.1.7}$$

Usually written in terms of the *ponderomotive energy* $U_p = \frac{e^2E_0^2}{4m\omega_0^2}$.
By substituting the expression of t as a function of t_0, one gets the expression of the kinetic energy that can be plotted, in U_p units, as a function of the ionization time t_0/T_0.

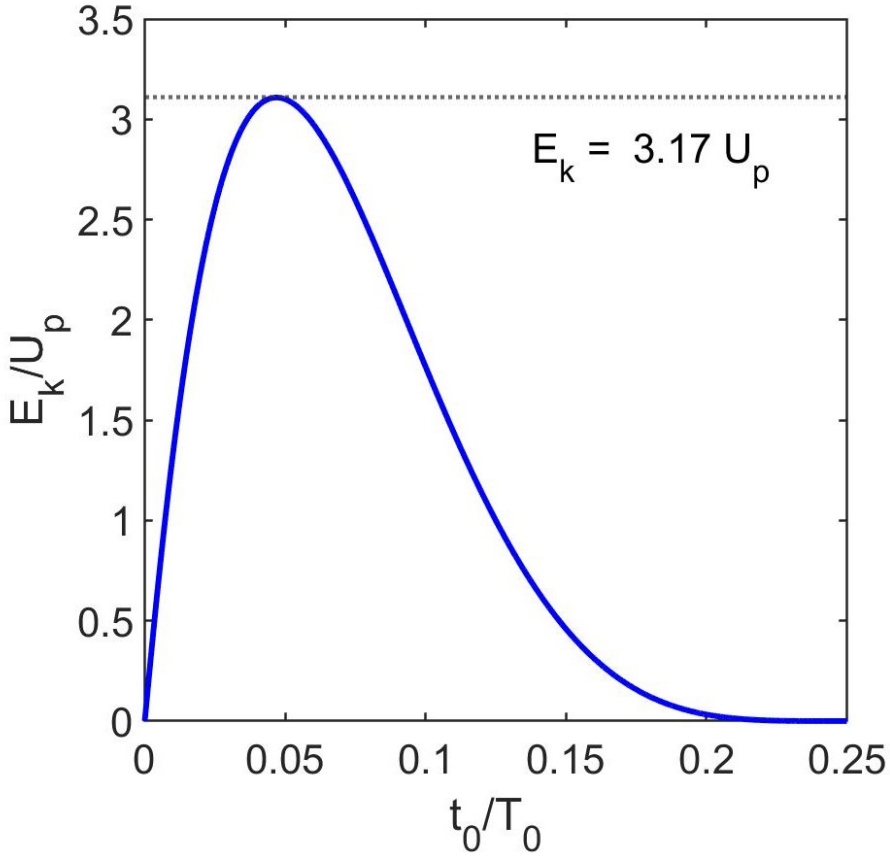

Figure 1.1.3: Kinetic Energy of the ionized electron E_k, normalized over the ponderomotive energy U_p, as a function of the ionization time t_0, normalized over the period of oscillation T_0 [23]

It is interesting to notice that the maximum kinetic energy is $E_{k,max} \approx 3.17U_p$ for ionization time $t_0 \approx 0.05\ T_0$, corresponding to recombination time $t \approx 0.7T_0$. In this way the maximum energy of the emitted photon is

$$\hbar\omega_{max} = I_p + 3.17U_p \tag{1.1.8}$$

where I_p is the ionization potential. This maximum of energy, corresponding to $t_0 \approx 0.05T_0$, identifies two kind of recolliding electron, that, even though have the same energy, are recolliding at different instant. From eqn 1.1.6, for smaller t_0 correspond larger t and vice-versa, hence for $t_0 < 0.05T_0$ the so-called "long trajectories "electrons are present which recombine at $t > T_0$, while for $t_0 > 0.05T_0$ the so-called "short trajectories "electrons are present which recombine at $0.3T_0 < t < 0.7T_0$. This condition is depicted in fig. 1.1.4

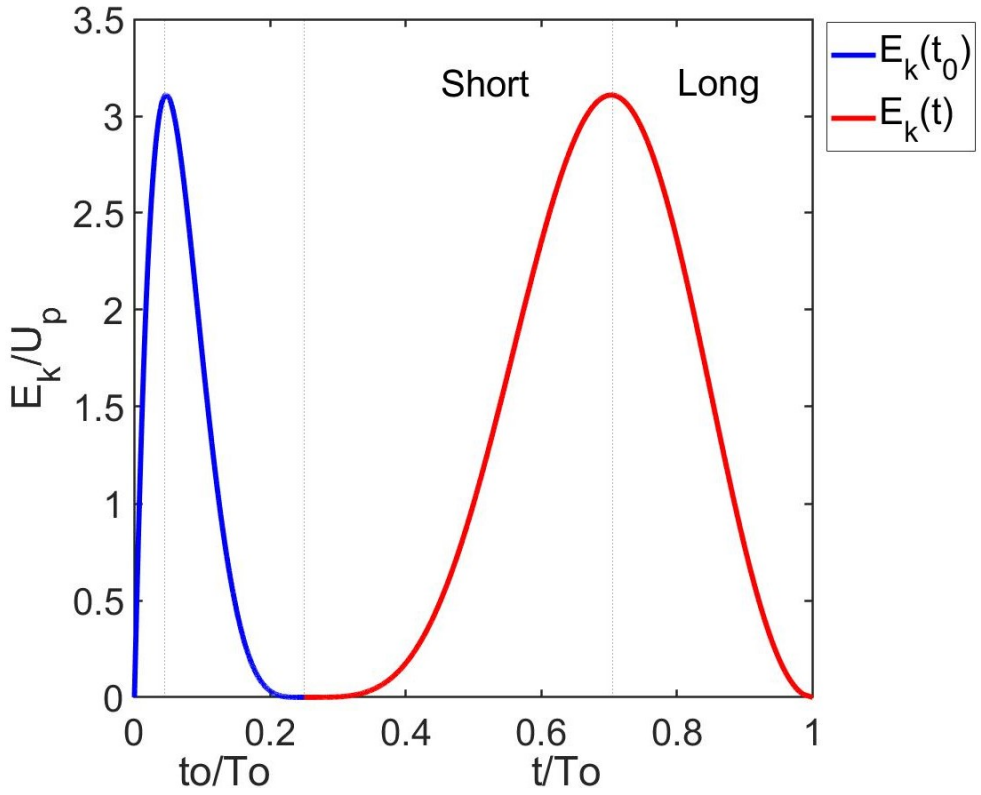

Figure 1.1.4: Kinetic energy E_k, normalized to the ponderomotive energy U_p, representing the"short trajectories"corresponding to "late electrons"and the "long trajectories"corresponding to "early electrons", as a function of the ionization time t_0 and the recombination time t, both normalized to the period of oscillation T_0 [23]

Hence, for two different instant of ionization, the emitted electrons have the same kinetic energy but have different physical characteristics: short trajectories electrons give rise to positive chirped photons ($d\omega/dt > 0$), while long trajectories to negative chirped photons ($d\omega/dt < 0$).

Third Step: Recollision

The last stage of this three-step model is represented by the recollision, which can be described in terms of the radiation emitted by an electric dipole. In the previous section, the electron has been modelled as a classical particle that "quantistically"overcomes the potential barrier. In reality, the electron is described by its wave function ψ_e, during the ionization process part of the wave function diffuses in the continuum (ψ_c) and part of it remains bounded to the ion (ψ_b), the quantistic interference between these two component ($|\psi_b + \psi_c|^2$) gives rise to an electric dipole, which oscillates as the wavefunction in the continuum propagates. This phenomenon acts as a microscopic antenna which generates high energy photon.
This whole process lasts for half of the optical cycle of the incoming electric field T_0, thus by using a linearly polarized electric field a train of attosecond pulses (TAP) is

generated, in which each pulse is separated by $T_0/2$, hence in a single optical cycle two pulses are generated. To obtain isolated single attosecond pulses it is necessary to limit the harmonic generation to a single event. The gating techniques pursue this aim exploiting spectral, temporal or spatial gating, but they will not be explored in this thesis.

1.1.1 Choice of the observable and techniques

Once the short pulses are generated, it is necessary to make them interact with the sample of interest. Typical sources for gas-phase samples will be described in chapter 2. Depending on the molecular dynamics, different observables could be chosen together with associated techniques to measure them. In general, after the interaction of XUV pulses (pump pulse), the sample is ionized, leading to the releasing and propagation of one or more electrons. The sample is thus in a non-stationary state and, by using a second pulse, it is possible to probe its dynamics. While in previous years the second pulse was usually a femtosecond IR beam, nowadays the research is moving toward the exploitation of two XUV pulses as both pump and probe [22].
The most common observables selected for molecule samples are listed in the following:

- The time variation of the quantum yield of a molecular fragment as a function of the pump-probe delay.
- The time distribution of the photoelectron coming from the ionized molecules as a function of the pump-probe delay and/ or the time variation of the angular asymmetry of the velocity distribution of a molecular fragment.
- The spectral characteristics of the emitted High Order Harmonic spectrum.
- The attosecond transient absorption spectroscopy which studies how the absorption changes when it is previously excited by an IR pulse.

Such observables can be measured according to precise experimental techniques that are analyzed in the following sections.

Attosecond cation chronoscopy

The quantum yield of one or more molecular fragments are measured as a function of the pump-probe delay. To this aim a Time of Flight (TOF) spectrometer is exploited: when the positive ions are measured, they are known as ion mass TOF [36]. This device allows for measuring the time required for a charged particle to travel along a certain distance. In particular, the ions are generated due to the interaction of the intense laser pulses with the sample, they are accelerated. Out of this region, they are accelerated thanks to constant electric fields, that can be either applied in a continuous way or in a pulsed mode and finally they are collected by a detector. The main constraint is that the electric field should be applied for all the time required for the ions to be produced: thus, all the ions receive the same energy. Furthermore, to make them receiving the same momentum, the previous

electric field should be turned off before the next ionization event has taken place. Hence, the velocity of the ions is a function of their charge q to mass m ratio (q/m). The arrival time is therefore function of this ratio: the lightest charged ions will arrive before the heaviest ones. The main advantages of this technique relies on the speed in the spectrum detection along with the selective spectrum recording for each ionization event: in this way, all the ions have the same condition if generated in a single event. Last, its accuracy is not affected by precise alignment but rather on the electronic circuit. A typical mass spectrum is reported in fig. 1.1.5. Ideally, every charge-to-mass ratio is characterized by a single line, however each peak presents a certain width due to the different initial conditions: the time spread is caused by the spatial separation in the ionization region (i.e., the fragments are produced in a slightly different position) and the initial kinetic energy distribution (i.e., the ions do not have the same velocity after the ionization event). This technique has been used in the work done by Calegari et. al. [9] to measure the ionization of the amino acid phenylalanine and the subsequent detection of ultrafast dynamics on a sub–4.5-femtosecond temporal scale.

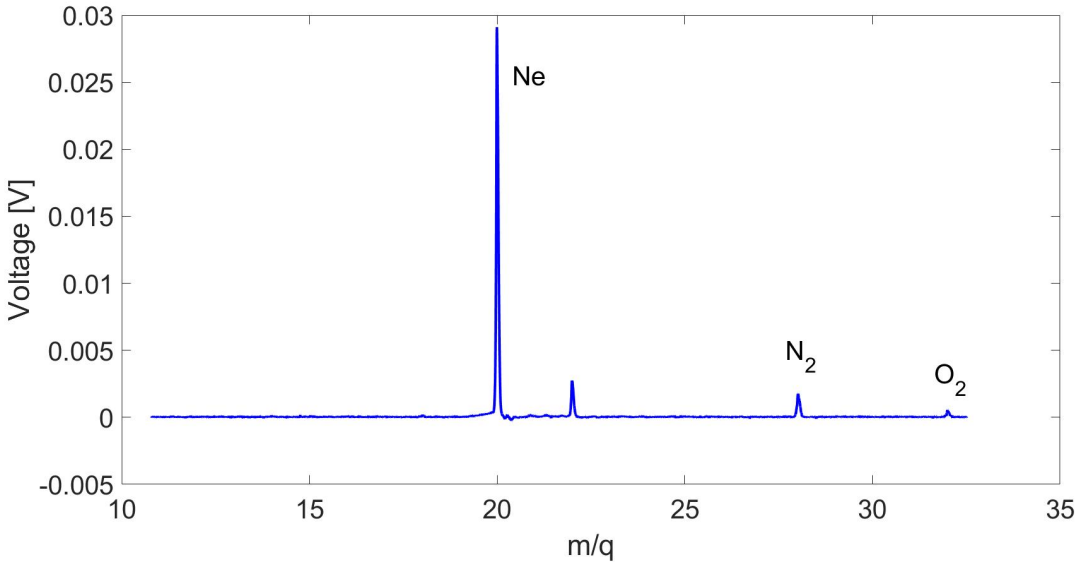

Figure 1.1.5: Example of a Ion yield, obtained after XUV ionization of Neon in the gas phase, performed in the ELYCHE laboratory. Several contaminants inside the vacuum chambers can be detected (N_2 and O_2). The second peak close to the Neon represents its isotope ^{22}Ne

Further details will be specified in sec. 3.2, where a particular TOF spectrometer will be described.

Angle- resolved photoemission spectroscopy

Although the exploitation of TOF spectrometers allow for obtaining high spatial and temporal resolution, they are limited in the angular resolution, since they cannot resolve the fragments' orientation. To this aim, a Velocity Map imaging (VMI) should be employed, allowing to achieve a 3D velocity distribution of the scattered particles [12]. This device is composed of a certain electrode configuration, creating an electric field that shapes the charged particles' trajectories and make them impinge onto a detector (typically one or more microchannel plates (MCP)) followed by a phosphor screen and a camera to record their impacts. These two dimensional (2D) images are sufficient to obtain information on the velocity and angular distribution of the ions, through inverting the Abel transform of the three dimensional (3D) distribution. The former transformation allows us to project 3D to 2D images, if spherical or axial symmetric functions are involved. Though different techniques have been proposed to invert the Abel transform, the most promising one relies on the measure of the angular and radial distribution of the 2D projection [35]; nevertheless, the ultimate resolution is given by the one of the spatial image, which usually appears to be lower then the one achievable with a TOF spectrometer. Thus, there exists a trade off between the recoverable information and the maximum accomplishable resolution. Even these experiments lean on the variation of the pump-probe delay which could fix the electron distribution and the produced image on the phosphor screen could present asymmetric features. An example is reported in fig. 1.1.6.

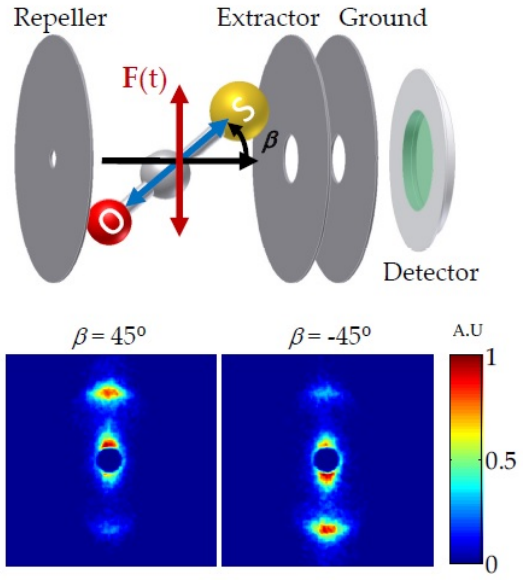

Figure 1.1.6: Example of a VMI spectrum (bottom): by varying the laser polarization is possible to align the molecule orientation (in this case carbonyl sulfide molecule (OCS)), obtaining different images as a function of the β angle described in figure. The electric field of the spectrometer breaks the symmetry preferring the O-end toward the repeller, re-adapted from [11]

Photoelectron spectroscopy

After the pump-probe interaction and the subsequent sample's ionization, one could choose to measure the emitted photoelectrons, obtaining, with a high spatial resolution, information on where the ionization event has taken place. To this aim an electron TOF spectrometer can be exploited, but instead of measuring the arrival time of charged particle, information on the energy distribution are analyzed [33]. In fact, let's consider the time T for an electron to reach travel for a certain distance L, as a first order approximation, considering its speed to be constant, the electron energy is:

$$E_0 = \frac{1}{2} m_e v^2 = \frac{1}{2} m_e \left(\frac{L}{T}\right)^2 \tag{1.1.9}$$

where m_e is the electron mass. Thus by measuring the travel time T, it is possible to retrieve the electron energy E_0. Actually, the emitted electron has a certain energy distribution which is related to the time width ΔT_1, related to its generation. After traveling for a distance L, the electron energy distribution is spread, as shown in fig. 1.1.7.

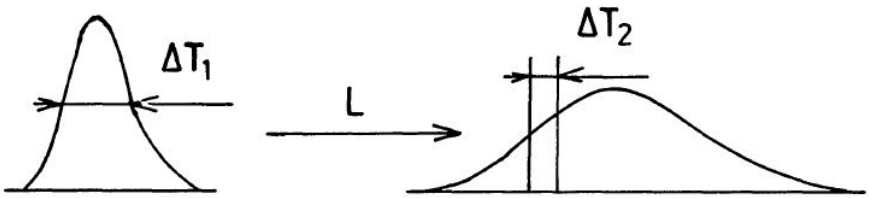

Figure 1.1.7: Electron energy spreading during propagation of length L

Thus, by measuring the time interval ΔT_2, it is possible to retrieve the electrons with energy given by eqn. 1.1.9, with a resolution of:

$$\Delta E = 2 \left(\frac{m}{2}\right)^{-1/2} E_0^{3/2} (\Delta T_1 + \Delta T_2) L^- 1 \tag{1.1.10}$$

To get reliable results, one should prevent magnetic interference which disturb the electrons trajectories by proper magnetic shielding.

High order harmonic Spectroscopy

Even though the HHG technique is used to generate attosecond pulses, the characteristics of the resultant spectrum highlights features on the molecular dynamics involved in such process. By detecting the emitted photons or the diffracted ion useful information can be extracted, in the framework of the pump-probe techniques. In fact, following the three step model described in section 1.1, the time between the ionization and recollision process can be seen as the pump-probe delay. The emitted photon spectrum contains information on the ionization-recombination process, on the on the molecular gas structure and its time evolution. Since a single photon

energy corresponds to two possible trajectories, by selecting only a single set, there is a bi-univocal correspondence between the photon energy and the electron travelling time. By acquiring the photon spectrum, it is possible to retrieve information on the different time intervals in which the electron appears to be in the continuum.

Attosecond transient absorption spectroscopy (ATAS)

The last technique that will be explored is the ATAS. The typical implementation regards a femtosecond pulse (in the visible or near-infrared (NIR)) that excite the sample, followed by an attosecond pulse used to probe its dynamics. The first pulse induces variation in the absorption cross-section of the sample that for this reason are said to be transient. The spectrum of the transmitted attosecond pulse is then measured using an appropriate spectrometer, as a function of the NIR and XUV delay. Compared to previous techniques, it enables to obtain a higher temporal and spectral resolution together with a higher data collection.

1.1.2 Attosecond spectroscopy in molecules

The main aim of attosecond techniques in molecules is to investigate and eventually control the electron dynamics: in chemical reactions, before the re-arrangement of the nuclei there exist ultra fast electron dynamics, known as "charge migration". This process can be described as the electron motion and transfer between distant sites within the molecule of interest, which affects the subsequent molecular dissociation. As a first approximation, one could think that, following the Born-Oppenheimer approximation, the electron motion, being much faster then the nuclear motion, can be completely decoupled; in reality, these attosecond electron dynamics and the slower nuclear process are tightly bounded, affecting each other reciprocally causing the undermining of the adiabatic approximation. Nevertheless, it is still in progress the acknowledgment of the dynamics control that could lead to the interruption and guidance of electrons to handle particular fragmentation or reactions. Up to now, these studies have been performed using an intense (XUV) attosecond pulses, (SAP or TAP) that act as pump, followed by (IR) femtosecond pulses that act as probe. However, this nomenclature is inappropriate and ambiguous. Commonly, pump-probe techniques are exploited in the femtosecond physics to characterize slower process: an intense femtosecond pump pulse is send toward the sample, which is excited, and a femtosecond probe is sent as a function of the delay τ between the two pulses. The second pulse is much weaker than the first one and acts as an effective probe, that explore the sample and thus can be modelled in a perturbative regime. The main assumption of weak probe pulse in the perturbation framework breaks down in the attosecond pump-probe techniques. The delayed (IR) pulse does not act as a probe, since it is almost as intense as the first one (this actually depends on the experiment one wants to perform), but rather it can control the electronic and the coupled nuclear motion. It is clear that the pump-probe terminology is incorrect and erroneous, nevertheless it has been established as the most common one.

H_2 and D_2 attosecond dynamics

Initially, attosecond pump-probe techniques have been applied to very simple molecules. The first example is represented by the most simple diatomic sample: molecular hydrogen H_2 and its isotope D_2. Since the nuclei are particularly light, containing at most one proton and one neutron for each atom, their motions are particularly fast and cannot be decoupled from the electronic one in the ionization processes.
One of the first work that investigated such motion exploited XUV "pump"pulse and an IR "probe"pulse [27]. The first pulse was measured to be in the order of few hundreds of attoseconds, while the last at about $6fs$. The observable of this experiment is the asymmetry in the momentum distribution of the ion D^+, detected with a VMI spectrometer (as described in sec. 1.1.1), being modulated as a function of the XUV-IR delay. The attosecond pulse, ranging from 20 to 40 eV, can trigger the direct ionization that leaves the ion D_2^+ in the state $1s\sigma_g$ or $2p\sigma_u$, that are related to different nuclei energies. By making the quantum overlap between the ground state of D_2 and the excited state of D_2^+, it is possible to show that the most probable transitions are those involving as final states $1s\sigma_g$ for low nuclear kinetic energies ($< 1eV$) and the $2p\sigma_u$ for larger nuclear energy ($\approx 5 - 10eV$), where the subscript g identifies orbitals with *gerade* symmetry, while u with *ungerade* symmetry. If one would consider only the XUV pulse, due to the selection rule, starting from the ground state (which has *gerade* symmetric) the final state of the system Ψ, composed of both the ejected electron and the ionized molecule, would be in an *ungerade* symmetry. Hence, if the ion is in the $1s\sigma_g$, the ejected electron would have an *ungerade* momentum, the other way around, if the ion is in the $2p\sigma_u$, the free electron would have a *gerade* momentum. After the measurement, the ionized molecule can collapse in one of these two final states.
The matter changes when there is an the interaction with the pump (XUV) and probe (IR) pulses. In particular, varying the delay between the XUV and the IR, it is possible to change the asymmetry of the ejected electron and localize the other electron on the left or on the right proton. This can happen according to two mechanisms, shown in fig. 1.1.8:

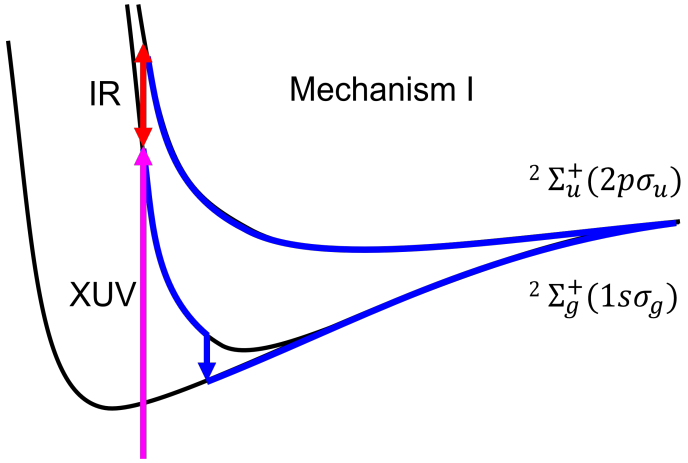

(a) Simultaneous absorption of the XUV pulse (pump) and IR pulse (probe) for the D_2 molecule

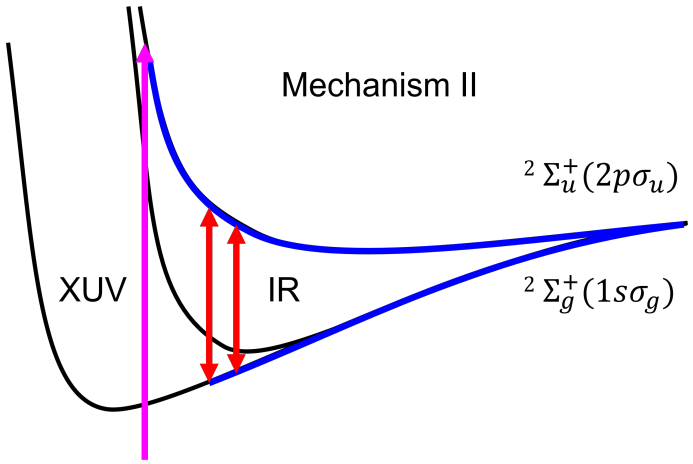

(b) First absorption of the XUV pulse (pump) and then the delayed IR probe for the D_2 molecule, readapted from [23]

.

Figure 1.1.8: Mechanisms of absorption of IR (probe) and XUV pulses (pump) for the D_2 molecule, readapted from [23]

- The simultaneous absorption of the XUV and IR pulses, which leads to the interference between the $2p\sigma_u$ state and the autoionization of the $1s\sigma_g$ state.
- The absorption of the XUV pulse, which populate the $2p\sigma_u$ and a late absorption of the IR pulse which coherently populate the $1s\sigma_g$ state.

In both cases, the final state is a coherent superposition of the $1s\sigma_g$ and $2p\sigma_u$. Hence, the final wavefunction can be written as:

$$\Psi(t) = c_1(t)[1s\sigma_g(1) + \epsilon l_g(2)]_g + c_2(t)[1s\sigma_g(1) + \epsilon l_u(2)]_u + c_3(t)[2p\sigma_u(1) + \epsilon l_u(2)]_g + c_4(t)[2p\sigma_u(1) + \epsilon l_g(2)]_u$$

where (1) represents the first electron, bounded to the ion, (2) the ionized electron in the continuum with energy ϵ and angular momentum $l_{u,g}$. Furthermore, the amplitude coefficients are time dependent on the pump-probe delay. The bounded electron can be measured on the left or right nucleus: if the final wavefunction collapsed onto the $\Psi_L = [1s\sigma_g(1) + 2p\sigma_u(1)]\epsilon l_{g,u}(2)$, the electron is bound to the left nucleus, otherwise on the right one if $\Psi_R = [1s\sigma_g(1) - 2p\sigma_u(1)]\epsilon l_{g,u}(2)$. What is experimentally measured is the asymmetry in these two measurement, which depends on the projection of the initial wavefunction $\Psi(t)$ on the Left or Right Wavefunction $\Psi(t)_{L,R}$, modulus square. In mathematical terms:

$$N_L - N_R = \Sigma_{i=g,u}[|\langle\Psi_{L,i}|\Psi(t)\rangle|^2 - |\langle\Psi_{R,i}|\Psi(t)\rangle|^2] \tag{1.1.11}$$

Hence, by expressing the inner products

$$N_L - N_R = 4Re[c_1 c_4^* + c_2 c_3 *] \tag{1.1.12}$$

While the coefficient c_2 and c_4 are controlled by the XUV pulse (which overall will give an *ungerade* final wavefunction), the other two coefficients are non zero due to the interaction of the IR pulse. Thus, the asymmetry coefficient $N_L - N_R$ varies with the periodicity given by the IR pulse: by delaying it, it is possible not just to "probe"the electron but to control its position and the asymmetry of the ejected electron. The final states are nothing but an entangled state between the bounded and the free electron, with a strong dependence on the nuclei distance.
This work opened the way to new experiments, that first involved diatomic molecules (O_2, N_2, CO) [29][9][40], and then more complex structure such as the aminoacid phenylalanine $(C_9H_{11}NO_2)$ which represents the only study in the attosecond dynamic of a complex molecule in the gas phase.

Phenylalanine attosecond pump-probe

The aminoacid phenylalanine is composed of a carbon atom linked to a carboxylic group $(-COOH)$, an amine $(-NH_2)$, a hydrogen and a simpe aromatic ring (in this case benzene).

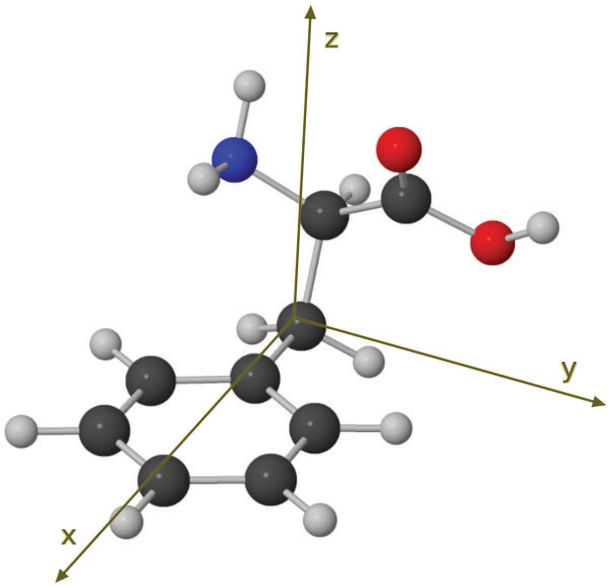

Figure 1.1.9: Phenylalanine Molecular structure.Dark gray spheres represent carbon atoms; light gray spheres, hydrogen atoms; blue sphere, nitrogen; and red spheres, oxygen, [9].

In this study [9], as pump an XUV pulse was used, with duration lower than $300as$ and as probe an IR pulse with duration in the order of $4fs$. The observable of the experiment is the variation of the immonium dication ($^{++}NH_2 - CH - C_6H_6$) quantum yield ($m/q = 60$) as function of the pump-probe delay. In particular, this doubly charged ion is present only when both the pump and probe pulses are present: it is a hint of the fact that the only XUV pulse is not able to produce it, but the combined action of the XUV and IR pulses does. Its rise time is about $10fs \pm 2fs$ and it shows an exponential decay in the order of $25fs \pm 2fs$ (fig.1.1.10 A). Furthermore, after subtract an exponential fitting that matches the decay (fig. 1.1.10 B), it has been shown that, for delays lower than $10fs$, this quantum yield oscillates with two frequency components are recognized at about 0.12 and $0.29PHz$, while for delays from 10 to $30fs$, it oscillates $\approx 0.234PHz$ (corresponding to a period of oscillation of $4.3fs$) (fig. 1.1.10 C). From this behaviour, two main conclusions can be derived:

- These oscillations cannot be caused by the nuclear motion, which correspond to larger period (the highest vibrational frequency of this molecule is at $\approx 9fs$ and corresponds to the $X - H$ stretching),
- Changes in the molecule's conformation can affect the charge migration process. At the working point temperature ($430K$), only six conformers are present.

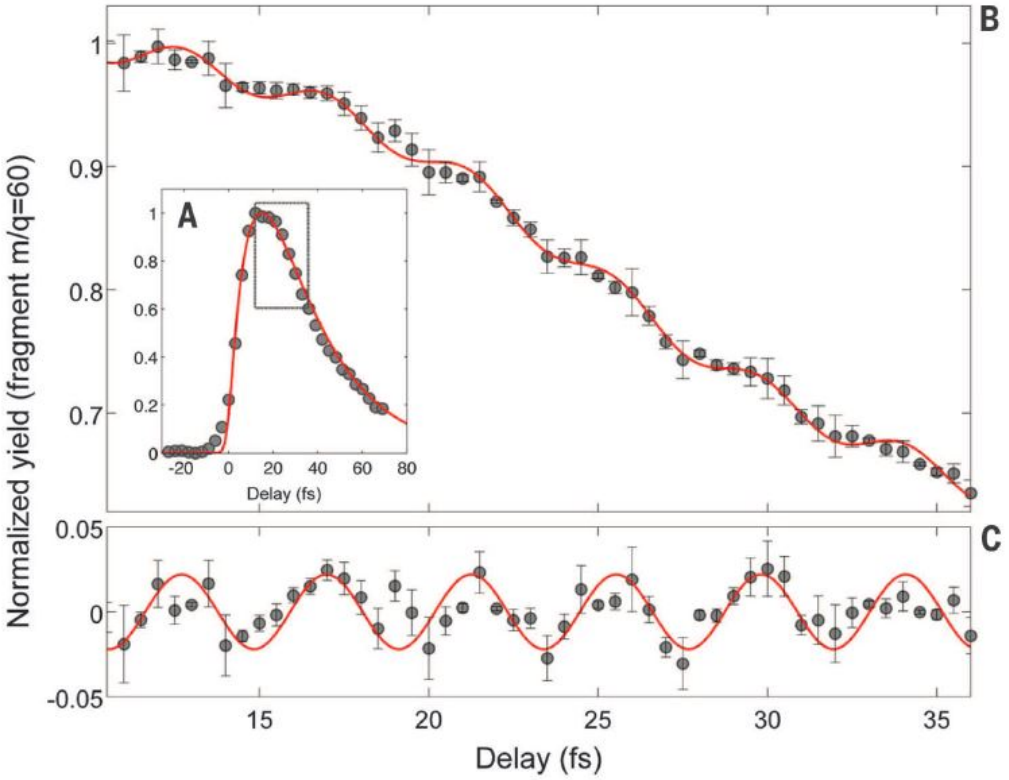

Figure 1.1.10: A) Normalized immonium dication ($m/q = 60$)quantum yield from $-20fs$ to $80fs$, measured with $3fs$ temporal step
B) Normalized immonium dication quantum yield from $10fs$ to $35fs$, measured with temporal step of $0.5fs$
C) Normalized immonium dication quantum yield from $10fs$ to $35fs$ after subtraction of exponential decay [9]

The very short oscillations at $4.3fs$ have been attributed to the charge migration processes from the amine ($-NH_2$) to the aromatic ring and back to the amine group. These mechanisms have been depicted in a very intuitive and captivating way in fig. 1.1.11.The starting of this mechanisms ($0fs$) corresponds to the end of the XUV pulse: for delays between 1.7 and $6.1fs$, the period of oscillation is about $4.4fs$, in which it is recognized the migration of the hole density from the amine to the benzyl group; similar behaviour, but with different dynamics, are present for delays from 7 to $11fs$

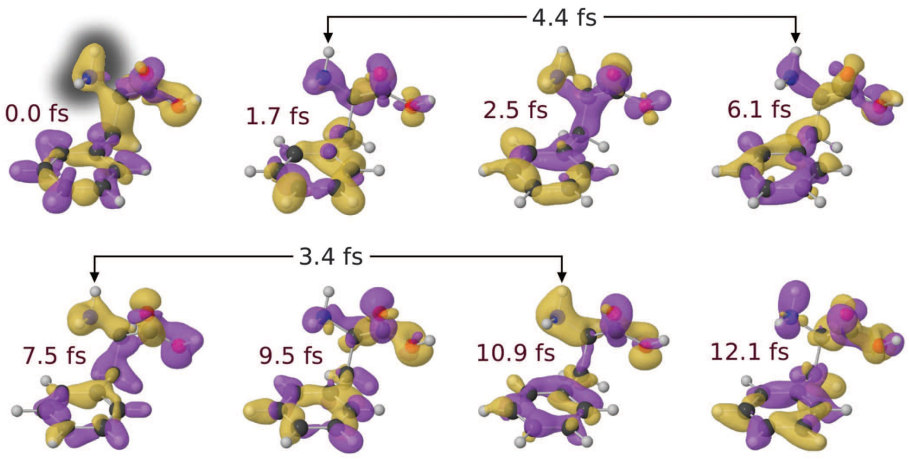

Figure 1.1.11: Relative variation of the hole density as a function of the pump-probe delay with respect to its time-averaged values, purple isosurfaces correspond to hole density with cutoff $\approx -10^{-4}$ a.u., while yellow isosurfaces to $\approx +10^{-4}$ a.u., Time is referred to the end of the XUV pulse [9]

By now, this work remains the only experiment which show charge migration in complex molecules and it remarkably paves the way to a series of new experiments involving charge migration processes in bio-molecules which can have an impact in the medical as well as the high-technological area.

1.2 Scope of this work

It has been shown that the interaction of attosecond pulses with molecules paves the way to a new branch of physics that highlights exotic and advanced mechanisms. Due to its relative new development, the experimental setups are custom and "home-made"built: one of the main issues is related to the way in which the sample, in the gas phase, is brought to the interaction region with the laser pulses. Due to the low photon flux of XUV attosecond sources, it is necessary to design and build molecular sources capable to achieve high target densities in order to improve the signal to noise ratio. Nevertheless this is not a trivial task since its design involves a fine control of large number of parameters. The most common setups employ a supersonic gas-jet, typically constituted by a noble gas, that transport a sublimated analyte toward the interaction region. The fine tuning of the gas properties (its pressure and temperature), the design of the nozzle and the interaction chamber shape the gas flow, which should ideally be spatial and temporal confined. All these critical parameters requires a deep knowledge of fluid dynamics.

The aim of this work is to characterize the valve, present in the ELYCHE (ELectron-scale dYnamics in CHEmistry) laboratory, which is responsible to carry such samples, presenting its state-of-the-art and its working condition. In order to achieve this goal, I have performed mathematical simulations of its performance and properties by means of the Direct Simulation Montecarlo (DSMC) software. Such program enables to verify current issues and, varying parameters of interest, suggesting improvement based on a solid mathematical background, in order to obtain repeatable working conditions that allow to carry out reliable pump-probe experiments. Such simulations have been complemented by an experimental characterization of the gas-phase source. Varying the physical properties of the gas and shaping the interaction region, it is possible to derive important conclusions from the numerical data that are then combined with the parameters' simulation, enabling to explain the gas source performances. In the last chapter, a real pump-probe experiment is performed by implementing one of the proposed solutions, coming from the simulation perspective.

Chapter 2

Gas sources for Attosecond applications

In this chapter, a review of the main types of molecular sources for attosecond pump-probe applications are presented. For each source its main advantages and drawbacks are critically analyzed and compared with one another.
Traditionally, there exists a large variety of techniques that allow the production of molecules in the gas form for spectroscopic research. Initially, large molecules of biological interest were directly ionized through *spray ionization* [14], which produced intact ions starting from solute species, being directly ready for mass spectroscopy. The main advantage of this "historical"procedure relied on the fact that it is almost non-destructive, in the extent that it allows the generation of ions starting from fragile biological molecules. Within this area three main categories can be recognized: thermospay (TS), aerospray (AS) and electrospray (ES); all of them rely on the application of a field to disperse small charged droplets of the molecule, in the liquid phase, into a bath gas.
Other approaches rely on the exploitation of an auxiliary laser field to induce the desorption (LD) of the molecules that are allocated onto an appropriate substrate. It is worth describing the general principle of these methodologies, because they are the ancestors of more sophisticated techniques that were developed specifically for the attosecond spectroscopy in the gas phase.
Nevertheless, it will be shown that LD techniques have been abandoned due to their intrinsic low efficiency, in favor of supersonic gas-jet that act as carrier, usually noble gas, that transfer large molecules. Typically, these carrier gases expand at high pressure in specific vacuum chambers and the bio-molecules are heated up to their evaporation temperature: in this way they can be easily conveyed to an interaction region.

2.1 Matrix-Assisted Laser Desorption/Ionization (MALDI)

In Laser Desorption (LD) techniques, large molecules are embedded in a matrix substrate. A pulsed laser, with duration in the order of tens to hundreds of nanoseconds, is employed to free the molecules in form of ions, being ready to enter in a TOF spectrometer [17]. The principle is schematized in the following picture.

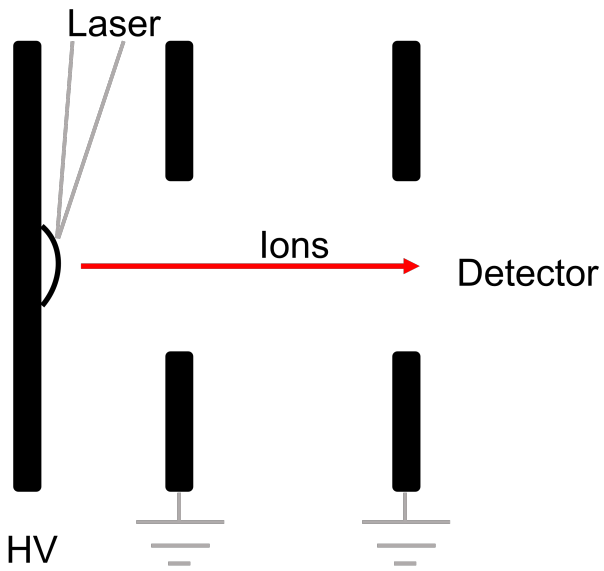

Figure 2.1.1: Matrix-Assisted Laser Desorption/Ionization (MALDI) scheme. A laser source impinges onto a matrix substrate where the molecules are embedded. The produced ions are then collected by a detector, readapted from [17]

.

Typical laser sources are constituted by UV excimer, Nd:YAG lasers but also IR lasers that are focused onto the matrix substrate according to different geometries and angle of incidence: the critical parameter of such process is not represented by the beam size, but rather by the irradiance deposited on the sample. In fact, there exists a threshold for which the production of ions increases abruptly and a region where the process is almost insensitive to its increase.
From our perspective, it is interesting to analyze how the molecules are embedded in the substrate which aims at two conditions:

1. Absorb the laser energy efficiently.

2. Isolate the large molecule from one another.

The matrix substrate is prepared as a solution with water or other organic solvent, mixed with the analyte and dried at room temperature. The sample is thus ready to be irradiated by the laser beam in appropriate condition, that may vary according to the matrix substrate, the molecule of interest and its rate of production. Different

matrix materials have been chosen to operate at different wavelength for peculiar classes of molecules.
The main restriction of this class of techniques is represented by the fact that the sample is already produced in form of ions, hence the charged molecules have different properties with respect to the neutral one. Furthermore, the analyte shows addiction of protons (protonation) leading to altered results in the mass spectra: such chemical reactions are unavoidable and their presence increases with the sample mass and it is strongly subjected to the matrix material. For this reason a similar technique was developed, aimed at overcoming these drawbacks.

2.2 Laser induced acoustic desorption (LIAD)

The evolution of previous techniques applies on the Laser Induced Acoustic Desorption (LIAD) [10] approach whose main idea appears to be very similar to its former methodologies but it is intrinsically different. Similarly, a pulsed or continuous (CW) laser source irradiates the sample that is freed by matching phonons excitations to the binding energies of molecules to the surface. However, the laser is not directly applied to the surface that contains the analyte but rather on the opposite side of its deposition. The produced sample is in form of neutral molecules and thus can be appropriately ionized through other sources of interest (ideally attosecond pulses).

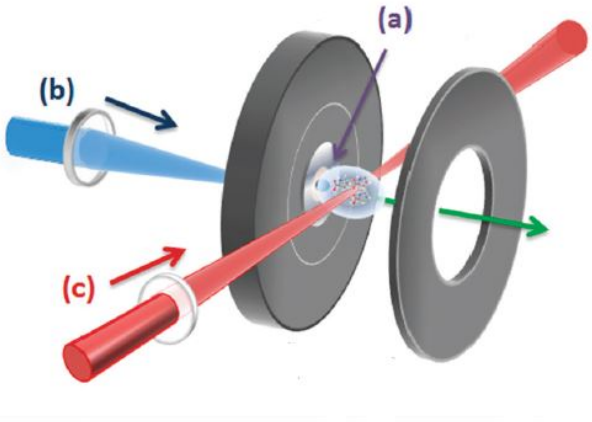

Figure 2.2.1: LIAD scheme: (a) analyte deposited on a surface matrix, (b) ns XUV laser pulse, (c) ionizing laser pulse, [10]

.

The main difference is thus related to the less energy deposition that is acquired by the molecules, which result to be less fragmented and compromise. The condition of applicability is that the pulsed laser length should be shorter than the thermal relaxation time, ensuring that the phonons have enough time to propagate through the material [24]. Furthermore, one has to take into account the delay between the energy deposition and the acoustic wave propagation in the material, that for thin layers is in the order of the microseconds [10]. The core difference between LD techniques and LIAD is that the former the analyte was liberated by impinging with an appropriate irradiance which caused a thermal stress, leading to the partial destruction of the molecule [15]. The latter is instead relying on both thermal and acoustic waves propagation, being less disruptive per se [38]. This consideration is consistent with the experimental characteristic of the independence of this process from the laser power deposition, hence depending mainly on the stored energy of the crystal. Furthermore, the yield of this process strongly depends on the combination of the analyte and the substrate material and thickness. As an order of magnitude, neutral plumes of isolated molecules can be generated with density up to $10^{-16}m^{-3}$. For instance, this technique was used by Calegari et. al [9] to produce a plume of neutral phenylalanine molecules from a thin metallic substrate being warmed up

by a CW laser and later ionized, as described in sec. 1.1.2. This result is actually quite surprising, since it has been proved that this technique, though providing a non-destroying way of producing large molecular jets, is poor efficient and contains large variation from one measurement to the other. This could in principle prevent to appreciate the fast oscillations observed in pump-probe experiments.
Due to its natural instability and its low density production, other methodologies have been studied which mainly rely on the exploitation of a noble gas that acts as a carrier to transfer the sublimated biological molecules, appropriately heated up at reasonable temperature.

2.3 Molecular Beams and Jets

Changing category of bio-molecular sources, the last and more promising typology seems to be the exploitation of gas sources to carry large molecules in the sector of interest. Two fundamental categories can be analyzed:

- Effusive source: the gas comes out from a pinhole, with diameter d, into a high vacuum chamber. The gas pressure should be sufficiently low to reach the condition of getting the gas mean free path in the order of the hole diameter.
- Nozzle source: the gas exits from a nozzle as a supersonic jet, involving much higher pressure and more narrow and localized stream. In this configuration, a skimmer is used to shape the gas jet and reduce its velocity distribution.

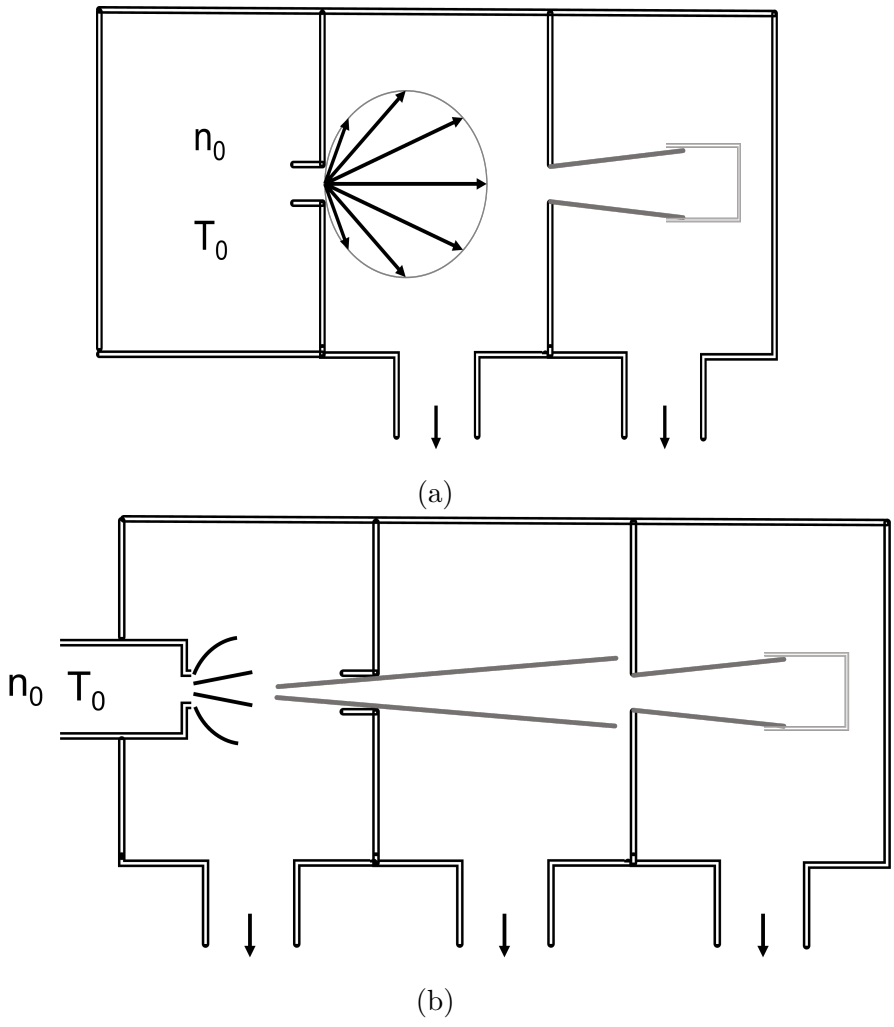

Figure 2.3.1: Schematic representation of two classes of gas sourced: the effusive (a) and nozzle sources (b) setup, readapted from [26]

This work will focus on the analysis of nozzle sources, specializing it to the description of two of the most used valves in the gas phase spectroscopy: the "Even-Lavie valve"[13] and the "Parker valve"[25], that can operate either in continuous or in pulsed mode.
The main restriction for operating in the supersonic regime is given by the vacuum pumps connected to the chambers: when operating in continuous mode the gas jet could have significant good properties in terms of spatial confinement and propagation. However, to have a larger sample for the analysis, the back-pressure needs to be increased: this implies the formation of sudden blocking structures and discontinuity (such as Mach disk and shock wave). For this reason, pulsed gas valves have gained popularity, being able to deliver the sample only when strictly necessary (i.e, synchronized with the laser pulses), still allowing the propagation at lower pressure with lower sample consumption, thus with more viable gas properties. As an order of magnitude, the gas pressure should be lower than 10^{-5} mbar in the vacuum chamber, to have a proper gas jet shape: this requirement can be matched exploiting low repetition rates ($\approx$ tens of Hz) with small vacuum pumps ($\approx$ hunderds of l/s), otherwise as the repetition rate increases larger pumps are needed (up to thousands of l/s) [13].

2.3.1 The Even-Lavie Valve

The Even-Lavie valve is a commercial valve that has been constructed to work in pulsed mode (with repetition rate from 0 (CW) to $600Hz$) with very short pulse duration ($\approx 20\mu s$). It allows us to have a very large range as back-pressure (up to 100 *bar*), hence it is sufficiently versatile to cover many applications but still it is a pre-packaged device that does not allow many customized adaptations [13]. It is interesting to notice that powder molecules can be inserted in this valve, since it already takes into account this possibility.
The working principle is rather intuitive: a pulsed current can flow into a coil, inducing a magnetic field that modulates a plunger's movement. Ideally, when the plunger is at rest, the valve is closed and the gas cannot flow (this corresponds to zero current flowing). By tuning the current (fig. 2.3.2), the plunger would follow it, regulating its behaviour, with a certain delay.

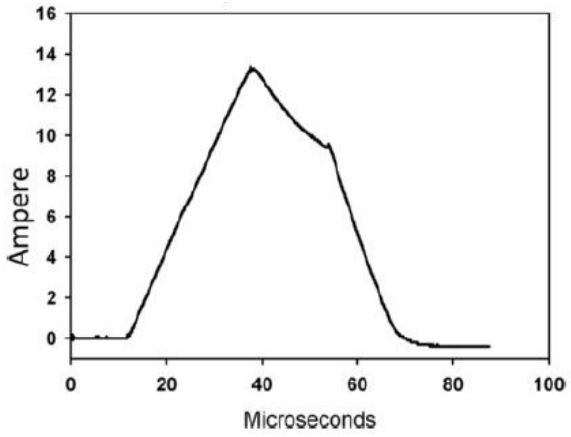

Figure 2.3.2: Plot of the pulsed current applied to the Even Lavie Coil as a function of time [13]

In practice, the coil is made of six layers of copper, which give account for $4\mu H$ and a resistance $< 0.2\Omega$, their combination results in a time constant of the current pulse equal to $\tau = L/R = 20\mu s$. This current induces a magnetic field, corresponding to a force acting on the plunger of $10N$, tolerating the fast opening and closure of the valve. As an order of magnitude, one has to apply a voltage of $24V$ which corresponds to a current flowing in the coil of $20A$, for about $20\mu s$, thus repeating this movement with high frequency would require the heat dissipation and corresponding increasing temperature of the device (for frequency of $500Hz$, the emitted power is almost $3W$). Overall, several trade off should be mentioned:

- High speed valve requires a fast changing driving current, which is at least limited by the combination of its inductance and resistance.
- The mechanical parts are intrinsically slower than the electronic one, if one increases too much the repetition rate the mechanical movement does not have time to follow it.

- Even though the driving current is in the range of applicability for the mechanical part to follow it, several bumps have been simulated to happen if oscillating too fast (fig. 2.3.3), causing the gas to flow even when the driving current is zero.
- If the frequency of the valve is high, the heat dissipation would increase much during the operation, causing mechanical deformation and introduction of other non-ideality.

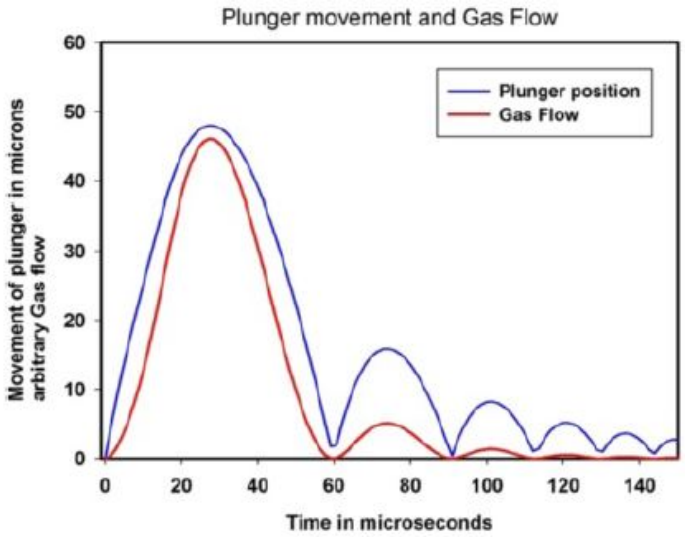

Figure 2.3.3: Plunger bumping and subsequent gas flow simulation, solving the equation of motion under simplifying assumptions [13]

These requirements and trade off have brought to the construction of several valve types, starting from the simplest "Room temperature unmounted valve", through valve that can operate at extremes temperature (cryogenic or high temperature) up to the full mounting system and manipulator, created ad-hoc for this kind of valve. The overall scheme of the simplest valve is reported in fig. 2.3.4, where it can be recognized the above-mentioned plunger which modulates the gas jet that exits from a conical nozzle. Its shape is a critical parameter to obtain a confined gas jet in the radial coordinate, without much broadening. This study shows that the combination of a conical (or parabolic) shape nozzle, with appropriate pressure can lead to the generation of a supersonic gas jet.
As a final remark, this valve represents a tremendous option for gas phase spectroscopy, thanks to its confined gas jet production, high repetition rate and broad temperature range; nevertheless it is a commercial product for which little can be done do adapt to already existing setup.

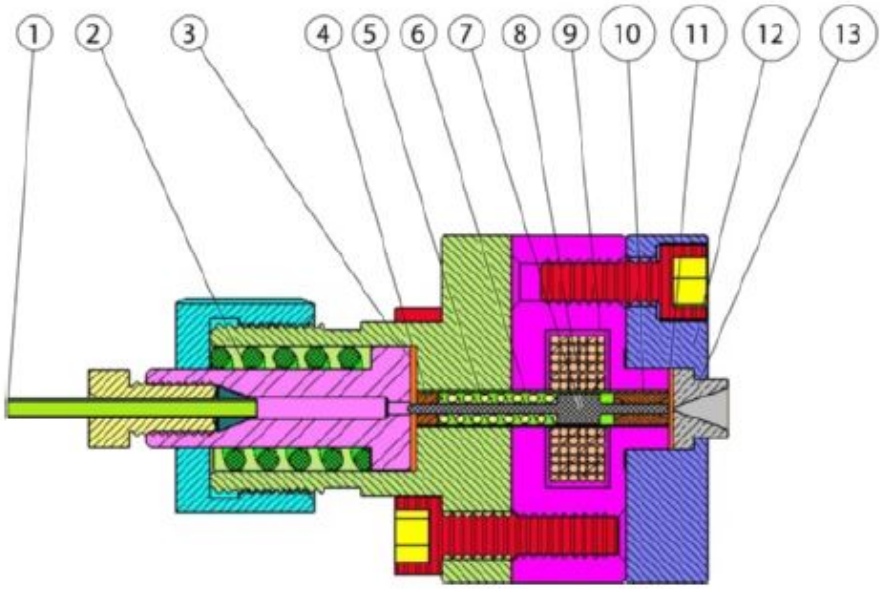

1. Stainless gas inlet tube (1/16").
2. Tightening spring (100N) and pressure relief valve.
3. Kapton foil gasket (rear, 0.125 mm. thickness).
4. Ruby rear guiding ferrule.
5. Return spring (Nimonic 19 alloy).
6. Thin walled pressure vessel (Inconel 625 alloy).
7. Reciprocating plunger (magnetic stainless steel alloy 750).
8. Kapton insulated copper coil (0.6 mm wire diameter 6x6 winding).
9. Magnetic shield (alloy 17/4PH) and field concentrator.
10. Ruby front guiding ferrule.
11. Kapton foil gasket (front, 0.125 mm. thickness).
12. Front flange (stainless or copper).
13. Conical (or trumpet) shape expansion nozzle (Zirconia ceramic or hardened stainless steel).

Figure 2.3.4: Room temperature Even-Lavie valve scheme cross section [13]

2.3.2 The Parker Valve

Another example of valve that can be exploited for the attosecond spectroscopy is the *General Valve Corporation Series 9*, from Parker. In the following it will be simply defined as Parker valve.
It is a pulsed valve driven by a solenoid that can operate with a minimum aperture time of $160\mu s$. The repetition rate is slower than the previous valve (up to $100Hz$) and the supported back-pressure can reach almost $90bars$. It is interesting to notice that the exit nozzle is constituted by a conduct which presents 2 conical end that can be closed, from one side with a tip that matches this shape (fig. 2.3.5,[1]).

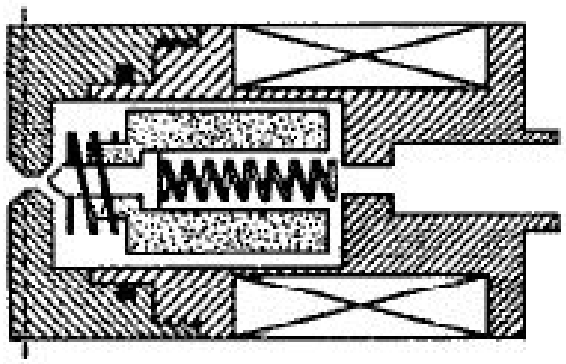

Figure 2.3.5: Section of General Valve Corporation Series 9 [1]

In particular, the exit nozzle has the most narrow part with a diameter of $0.5mm$, that widens with an half-angle of 45° for other $0.5mm$, shaping a cone of a total aperture of $1.5mm$. Overall, it can stand temperature up to 110°.
Less technical details can be found for this valve, but it is much more versatile and the different pieces can be modeled to match already existing setups: what is interesting is the operating range of this valve, in fact it can work in continuous or in pulsed mode but only up to $100Hz$. Furthermore, it does not allow for inserting powder molecules and an additional structure is needed. This is the valve that has been used in the experiments for this work.
At this point the overall setup can be analyzed in details.

Chapter 3

Experimental Setup

In this section, the experimental beamline of the ELYCHE laboratory will be briefly presented, with a focus on the biomolecular source specifications. An overall scheme is reported as a block diagram, in fig. 3.0.1.

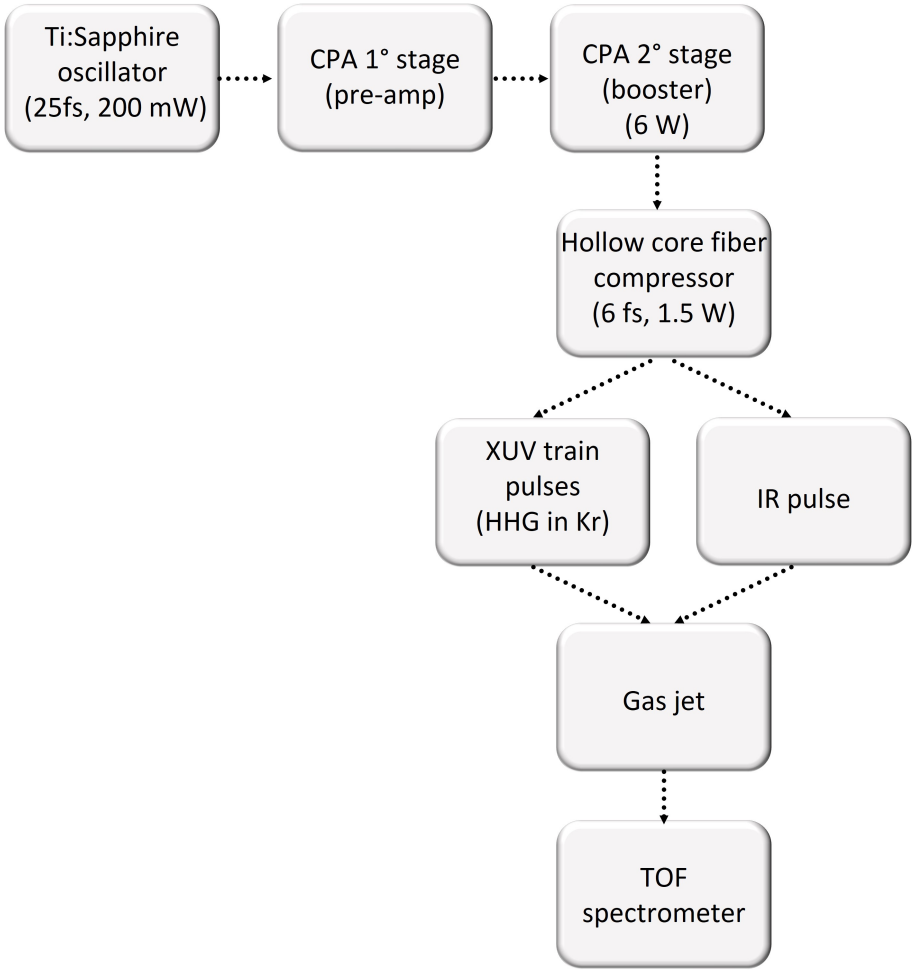

Figure 3.0.1: Schematic representation of the ELYCHE setup through simple boxes

3.1 Beamline

The first stage uses a Ti:Sapphire oscillator which emits short pulses ($\approx 25fs$) with a power of $200mW$, working in mode-locking with a repetition rate of $80MHz$. In order to shorten the pulse duration and increase the laser power different steps are analyzed and described in the following.

Laser amplifier

In order to generate attosecond pulses and probe efficiently the molecular sample, amplification stages are required. Two subsequent Chirped Pulsed Amplification (CPA) Stages are used to amplify these laser pulses. In both cases, the pulses are firstly stretched in time and then they are amplified in a Ti:Sa crystal pumped by a frequency-doubled Nd:YAG laser. The first stage (pre-amplifier) consists of a multi-pass amplifier (9 amplification stages). At the output of this stage the power is about $2.3W$. The second amplification stage (booster) is achieved in a 2-pass configuration. To achieve the transform limited duration after amplification, a pair of grating pairs are used to synchronize the different frequency components (introducing negative second order dispersion). At the output of this stage the laser power is $\approx 5 - 6W$, with a duration in the order of $30fs$.

Hollow core fiber

The laser pulses are then focused into a Hollow core fiber where, exploiting a third order non-linear effect (Self-Phase Modulation SPM), the light spectrum is widen depending on the gas pressure within the fiber itself. In this setup, the fiber has a length of $1m$ and a diameter of $300\mu m$. A feedback system constituted by two motorized mirrors and two photo-detectors allows to reach a sub-micrometers precision in the stabilization of the beam pointing toward the fiber (Automated Laser Beam Alignment and Stabilization System- ALIGNA). There is a trade-off between the widen of the spectrum and the photon losses due to absorption and scattering within the fiber: for this reason the fiber input is maintained in low vacuum ($10^{-1}mbar$), while the output is filled with Helium at high pressure ($< 1bar$). In this way a pressure gradient is generated aimed at balancing these two effects: the power output, with the filled fiber, is about $1.5W$. Nevertheless, the pulses are stretched in time and a set of chirped mirrors are used for pulse compression. At this stage the transform limited pulse duration can reach up to $4.5fs$.

XUV-IR interferometer

At this point, the laser pulses are divided into two branches with the exploitation of a beam-splitter ($70:30$). One branch (70%) is used to produce the attosecond pulses, the other branch (30%)is used as probe for pump-probe experiments, fig. 3.1.1.

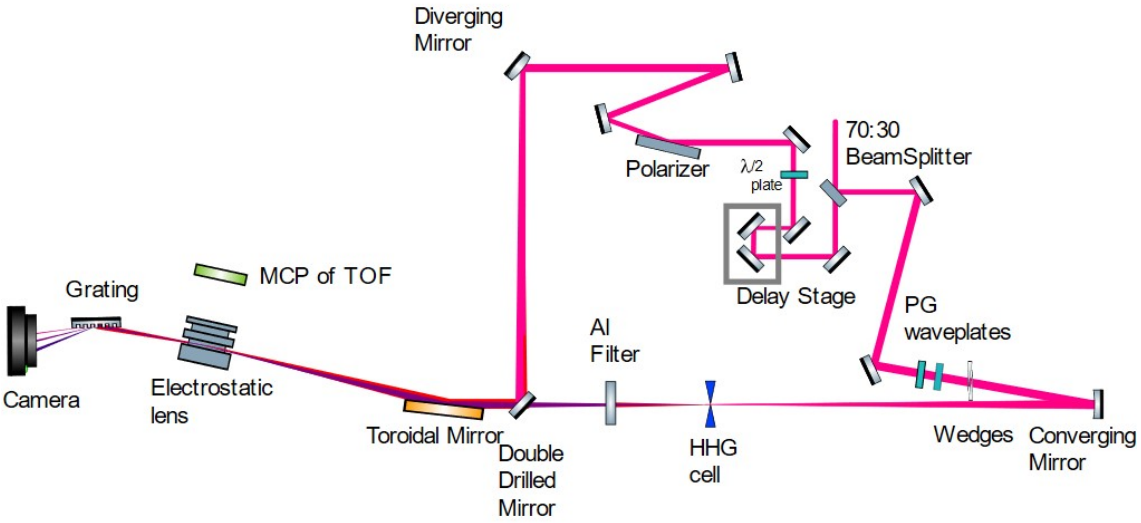

Figure 3.1.1: XUV-IR interferometer schematic representation of the ELYCHE laboratory, after the hollow core fiber compression step

In particular, the first branch, reflected by the beam splitter, is needed to generate the XUV train pulses (pump pulses), through HHG in Krypton as described in sec.1.1. The pressure gas is about $2.2 \cdot 10^{-3} mbar$ and the cell is motorized and can be finely tuned to match the beam focus. A couple of two fused silica wedges are present to compensate the dispersion and allow for tuning the generation. After the HHG chamber, an Aluminum filter is used to clean the residual IR, so that only the XUV can go through the line and being focused by a toroidal mirror to the interaction region, fig. 3.1.2.

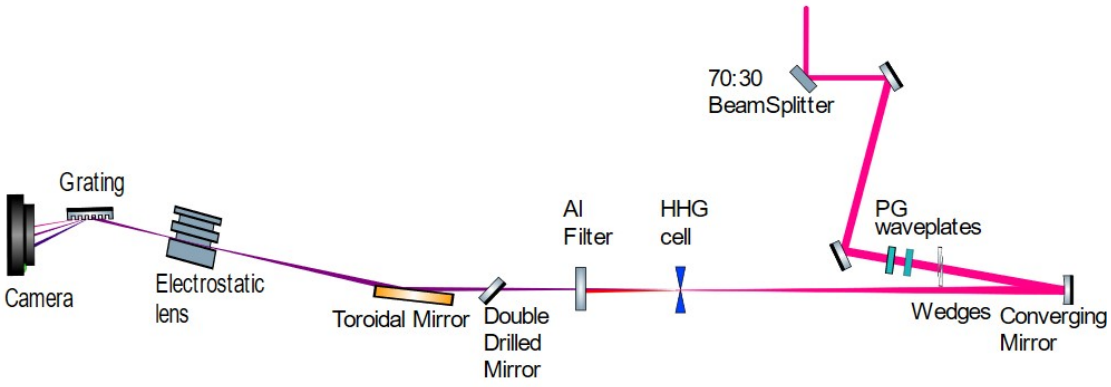

Figure 3.1.2: XUV branch generation schematic representation, highlighted from the XUV-IR interferometer setup of the ELYCHE laboratory, after the hollow core fiber compression step

The other branch, contains the part of the beam splitter that is transmitted, is retarded with a delay stage, allowing fine tuning for attosecond spectroscopy, and is used as probe pulse. Also the IR pulses are focused thanks to the toroidal mirror into the interaction region, fig. 3.1.3.

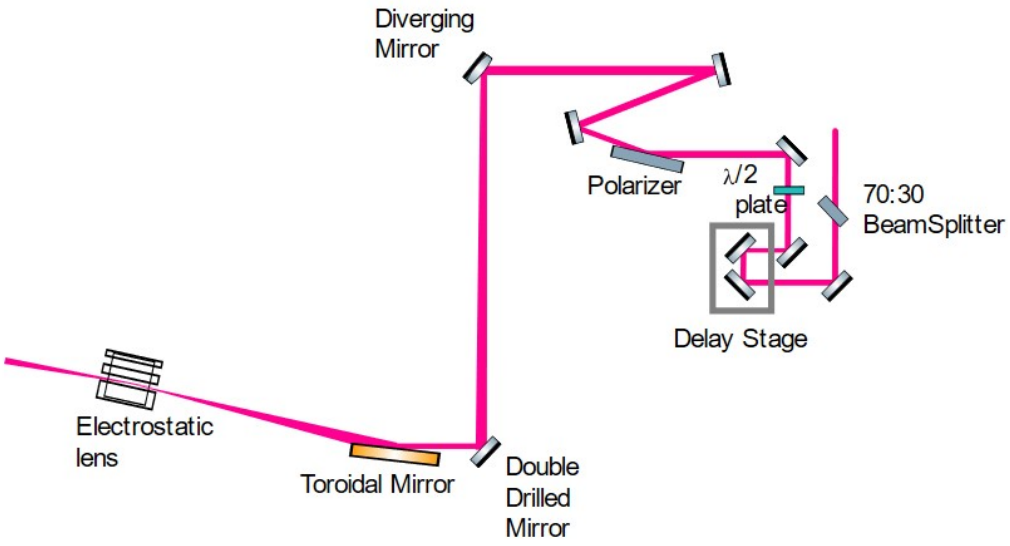

Figure 3.1.3: IR branch schematic representation, highlighted from the XUV-IR interferometer setup of the ELYCHE laboratory, after the hollow core fiber compression step

These two branches are spatially and temporally aligned to make them interact in the region of interest. Also in this case, a stabilization mechanism is needed to compensate variation between the XUV and the IR branches: this is achieved using a He-Ne laser ($\lambda = 633nm$) that follows the IR and the XUV paths. In particular, the mechanism exploited is the one of the Michelson interferometer. The He-Ne is split into two branches: one follows the IR path and the other the XUV, if the difference between the two paths changes the interference pattern is varied, thus by stabilizing its phase one could set the difference in length between the two paths. Hence, their variations are used to compensate unwanted path movements, exploiting a photo-detector that records the fringes and a feedback loop. This procedure is particularly interesting because it is independent from the lasers wavelength and can be reproduced with a high reliability, fig.3.1.4, [21].

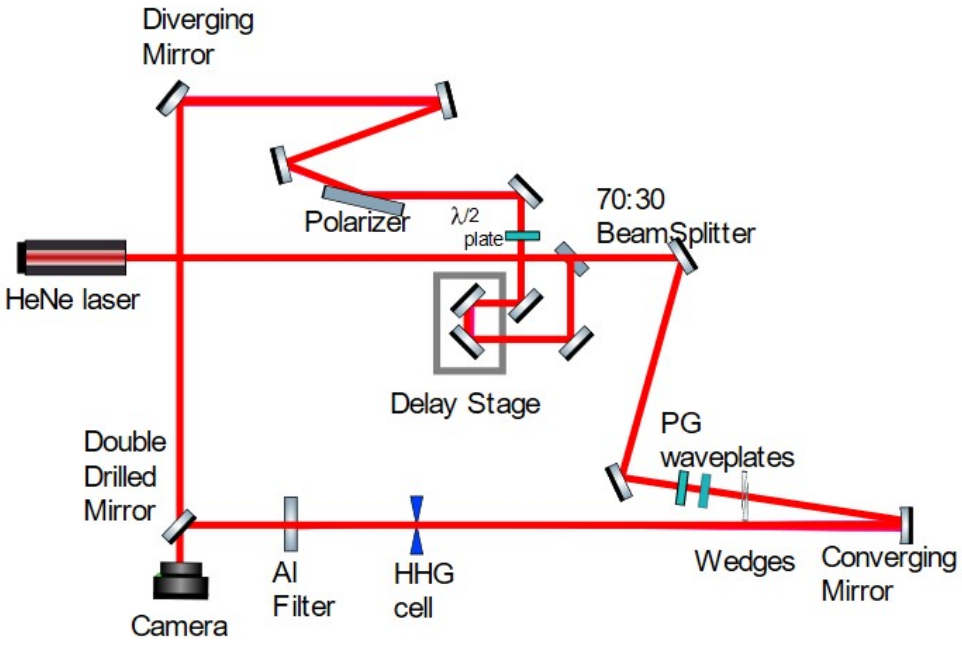

Figure 3.1.4: He:Ne stabilization line schematic representation of the XUV-IR branch present in the ELYCHE laboratory

Both branches present $\lambda/2$ plates that allow for changing light polarization to suitably trigger photoions or photoelectrons.
At this stage, the bio-molecular source is presented in details.

3.2 Bio-molecular source

In order to bring the analyte to the interaction region, a noble gas (typically Helium, Neon or Argon) is used as a carrier. One can control the back pressure of this carrier and the amount of gas that flows through the tubes connected to the Parker valve, described in sec. 2.3.2. The valve is then followed by an oven made of stainless steel, that can be heated up to hundreds of Celsius degree, in order to reach the molecule sublimation temperature. The analyte is inserted in the oven through an hollow core screw, filled with molecule powder: in order to allow its vapour expansion, a small expansion volume ($0,2cm^3$) follows the screw. Since the operative temperature range of the valve can vary up to 110° and the oven, for particular molecules, it needs to be heated up to 200°, a ceramic insulator is inserted in between, to allow heat dissipation, fig. 3.2.1. The exit nozzle from this structure is a conical one with an inner diameter of $1mm$, an half angle of 45° and an outer diameter of $2mm$.

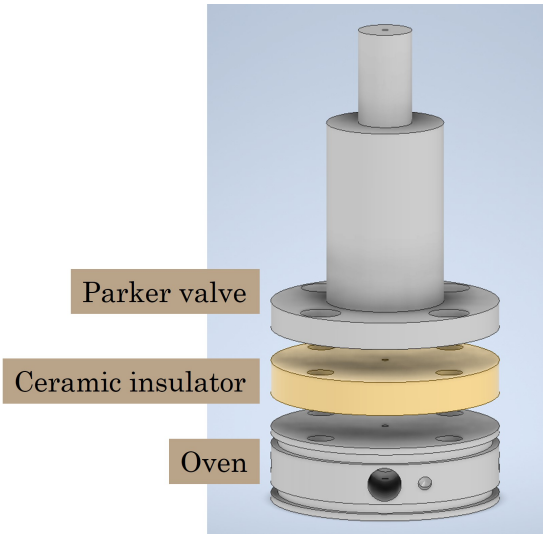

Figure 3.2.1: Valve-Ceramic insulator-Oven structure of the Biomolecular source, of the ELYCHE laboratory (expanded view)

Since this valve can operate in continuous and in pulsed mode, two regimes have been identified (CW or pulsed). Nevertheless, the pulsed mode is limited by the maximum operation rate of the valve ($100Hz$), which is lower than the laser repetition rate ($1kHz$). This translates into a loss of the number of laser pulses that can be exploited for the measurement (fig. 3.2.2).

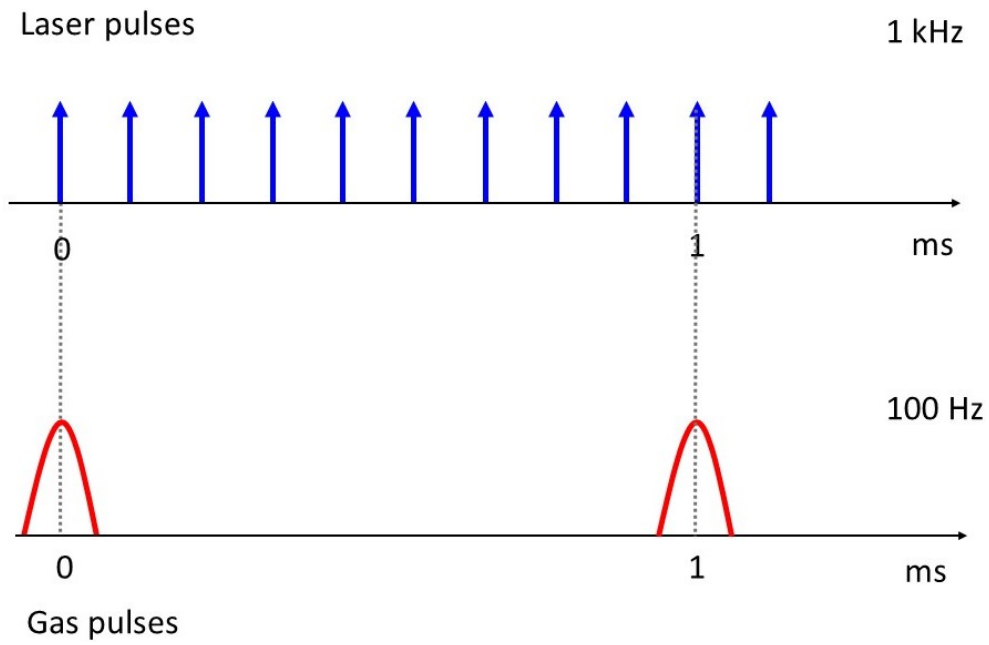

Figure 3.2.2: Schematic representation of the laser pulses ($1kHz$)and gas jet ($100Hz$) synchronization over $1ms$ time

The valve is separated from the interaction chamber by a skimmer (provided by Beam Dynamic Inc.) with a $1.5mm$ diameter that separates two vacuum chambers, the "biomolecular chamber"(or "source chamber") and the "interaction chamber"(or"TOF chamber"), where the molecules are ionized by the laser pulses and the photofragments are collected by a TOF spectrometer that can work either collecting photo-electrons or photo-ions. An overall scheme is reported (fig. 3.2.3).

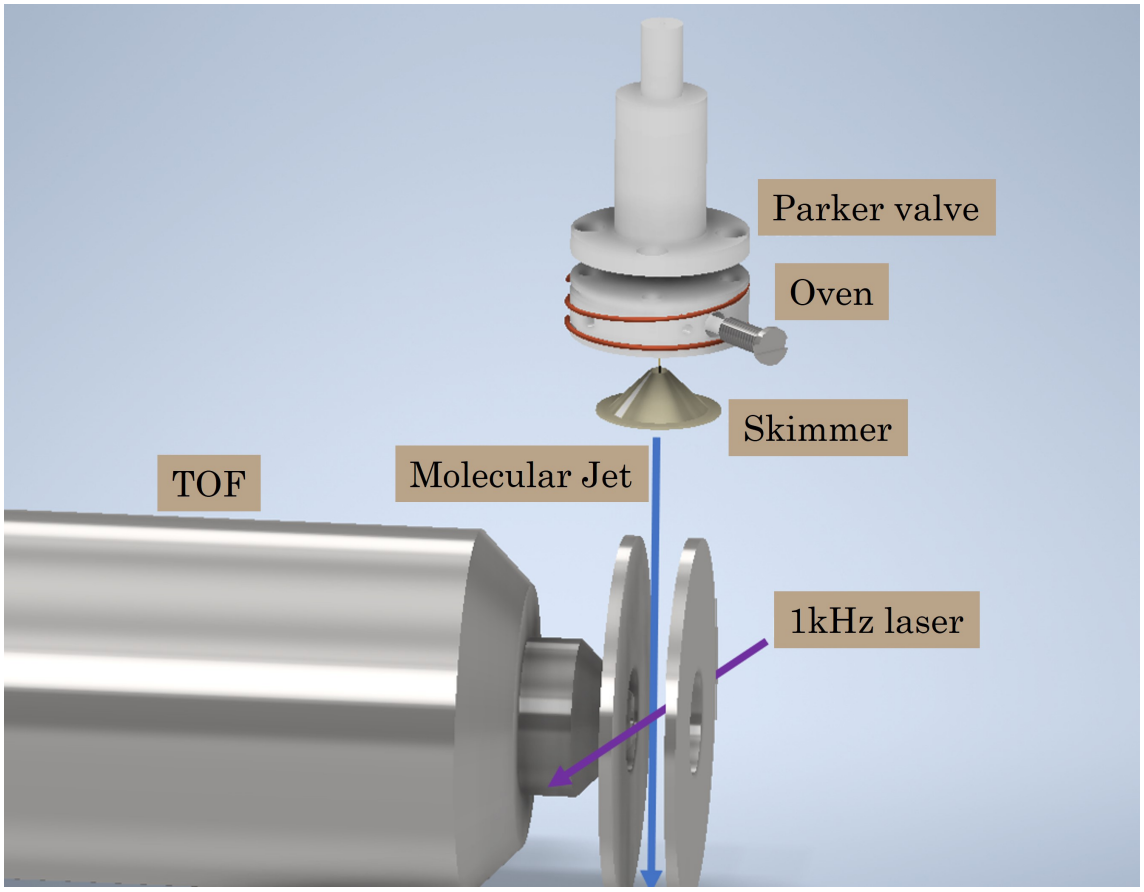

Figure 3.2.3: Scheme of the bio source interaction with the laser: the carrier gas exits from the Parker valve, it transports the analyte in the gas phase (which has been generated in the oven) toward the skimmer. The molecular jet interacts with the laser pulses (at $1kHz$ frequency). The generated charged particles (ions or electrons) are collected by the TOF spectrometer

The skimmer should fulfils a two-fold objective:

- It should maintain a differential pumping between the the "biomolecular chamber"and the "interaction chamber", since the TOF is equipped with a Micro Channel Plate (MCP) and cannot reach extreme pressure (no more than 10^{-5} $mbar$).
- It should shape the gas jet to provide a well spatially confined gas jet.

In order to match the skimmer position, that is previously moved to be aligned with the pump-probe pulses, the valve structure is mounted on a manipulator that allows for tuning its position in the three spatial dimensions, thus changing the position in a plane perpendicular to the gas jet, to match the skimmer entrance hole and in the axis perpendicular to it, that enables to vary the distance between the valve exit and the skimmer entrance. Instead, the distance between the skimmer and the laser

is 4.5cm and is fixed in this configuration.
A section of the overall scheme, fig. 3.2.4, shows the shape of the vacuum chambers. In particular, the "source chamber"is equipped with two vacuum pumps, each of which with a capacity of $450 L/s$.

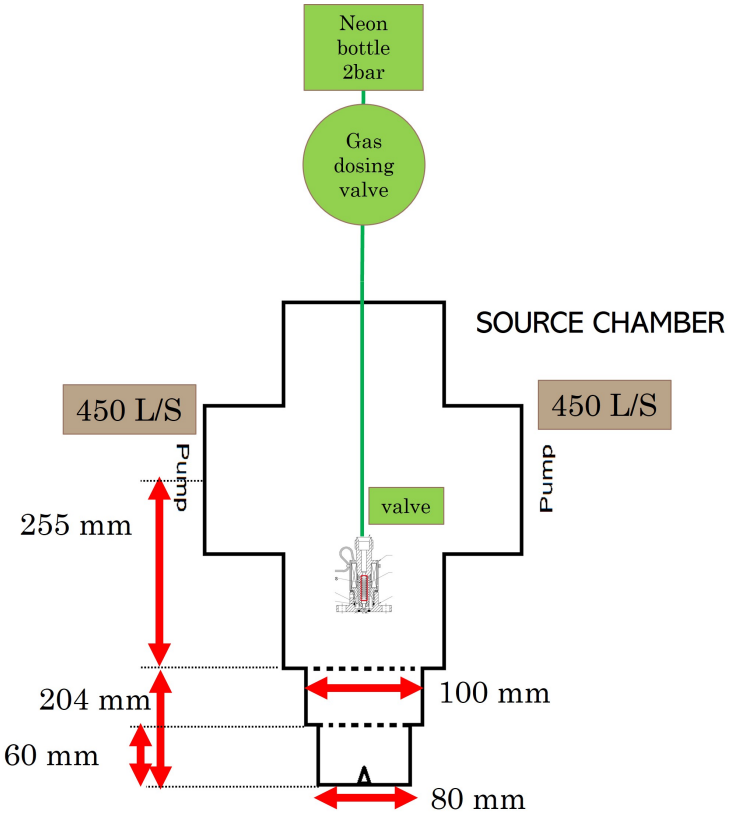

Figure 3.2.4: Schematic section of the source chamber, highlighting its geometrical parameters

After the interaction with the laser pulses, photoions or photoelectrons are collected by a TOF spectrometer. From the experimental point of view, the TOF spectrometer exploited for this work is depicted in fig. 3.2.5 as a longitudinal section. It is composed of an extraction optics, a drift tube and a post-acceleration stage where the detector is placed.

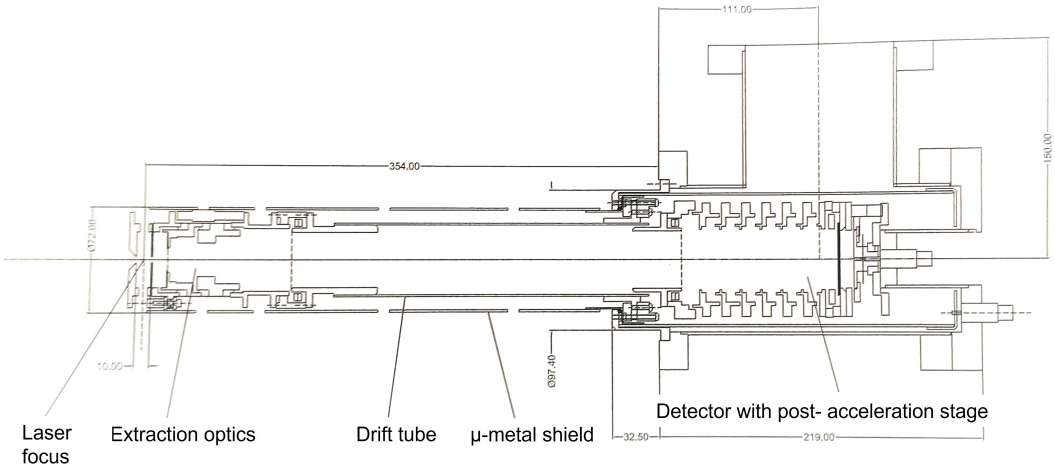

Figure 3.2.5: TOF scheme longitudinal section, used in the ELYCHE laboratory

In particular, the TOF can work either in ion or electron modes.
The extraction optics is constituted of two electrodes, the *repeller* and the *extraction*, fig. 3.2.6: when working for positive charges, the first electrode is kept at positive voltage, while the second one at negative voltages, typically at $\pm 155V$. As the names suggest, the *repeller* is able to reject the positive charges, while the *extractor* is pulling them toward the next region: the ionization takes place in between these two electrodes. Then, the charged particles are shaped by the lens, which is kept at $-2.0kV$, that works as an electrostatic Einzel lens: it focuses the beam without changing its energy. Then the drift tube, usually kept at $-2.0kV$ too, anticipates the post-accelerating region.
When working in electron mode, the *repeller* and the *extraction* are on ground potentials. The lens is kept at positive potential allowing to increase the acceptance angle of the electrons (typically at $10V$), while the drift can be kept either at positive or negative voltages: if kept at negative voltages it is able to slow down the electrons and thus allowing to measure particles with energy larger than $200eV$, otherwise if kept at positive voltages it allows to accept lower signals, in fact the electrons are accelerated into the drift tube reaching higher kinetic energies than when they were expelled. In these experiments, since the electrons' energies are poor, positive voltages are applied to the drift tube. Furthermore, in order to diminishing the effect of the external magnetic field a μ metal shield encapsulate the drift tube.

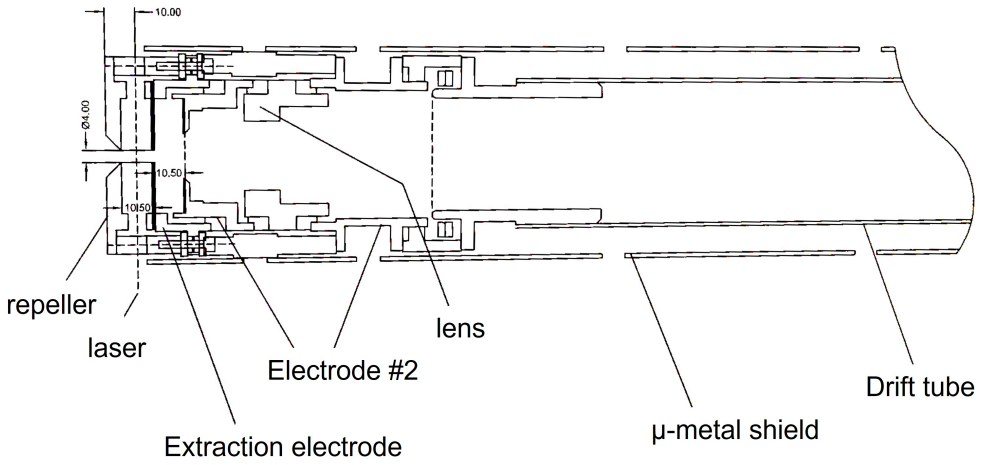

Figure 3.2.6: Schematic representation on the extraction TOF optics, used in the ELYCHE laboratory

Finally, after a post-accelerating stage, the charges particles hit a micro channel plate detector and are analyzed with a common computer.

Chapter 4

Characterization of the biosource valve

After the description of the setup, different tests have been made to characterize the biomolecular source.
First of all, it is necessary to characterize the valve, without the presence of the oven, that usually hosts the powder biomolecules. The main aim is to understand how the carrier gas expands in different physical conditions. Since the main objective is to use the valve in pulsed mode, to reduce the load on the pumps and the waste of biomolecules, the main characterization regards the synchronization of the laser train of attosecond pulses and the gas jet. Furthermore, different valve-skimmer positions will be studied together with different pulse durations to understand the most suitable operative conditions.

4.1 Test of the Parker valve without the oven

Since the valve itself provides a certain gas shape propagation, the first test that we have done is the characterization of the gas carrier without the oven attached to the valve (fig. 3.2.1).
The working conditions are described as follows:

- Neon has been used as carrier gas.
- The overall back-pressure is 2 *bar* exiting from the gas bottle, but the pressure injected in the source chambers can be adapted using a needle valve that allows for tuning the gas pressure as desired. Unfortunately, it is not possible to read the value of the gas pressure after this valve, hence the conditions are varied according to the needle value that can range from 0 (close valve) up to 999 (completely open valve). Its working principle is intuitive: as an handle is rotated, a plunger is moved and let the gas flow with a very fine tuning. The closing position corresponds to the complete grip of the plunger to a pointed end, that completely accommodates its tip [31].
- Due to previous considerations, only the pressure in the source and TOF chambers can be monitored. Hence, different needle values will be tested and their corresponding pressure will be analyzed. In order to not destroy the MCP detector, a pressure in the TOF chamber below $10^{-5} mbar$ is desired.
- The valve can work either in continuous or in pulsed mode. In the last configuration the time aperture can be varied to suitably choose the one that gives the best signal.
- The distance between the skimmer and the valve can be varied to obtain the most performing working conditions.

4.1.1 Alignment optimization

In order to first optimize the alignment between the valve and the skimmer and between the skimmer and the laser pulses, the valve has been made running in continuous mode to avoid unwanted effects between the gas jet and the laser pulses train. The manipulator allows to tune such alignment with a discrete reliability that can be monitored by looking at the TOF chamber pressure: its maximization corresponds to a good matching.
With a needle value $n.v. = 302$, a back-pressure of 2 *bar* and fixing the distance to the skimmer to $2mm$, in continuous mode, it appears that the gas could not have a directed gas jet but could be much more spatially broaden, and the skimmer is not able to intercept the central part of the gas jet. This is also confirmed looking at the ion yield and moving the laser beam with respect to the gas jet. Moving the entire TOF structure orthogonal to the beam, no big changes in the ion yield are detected in the range of $3.5mm$, fig. 4.1.1. However, these hypotheses will be proved in the following.

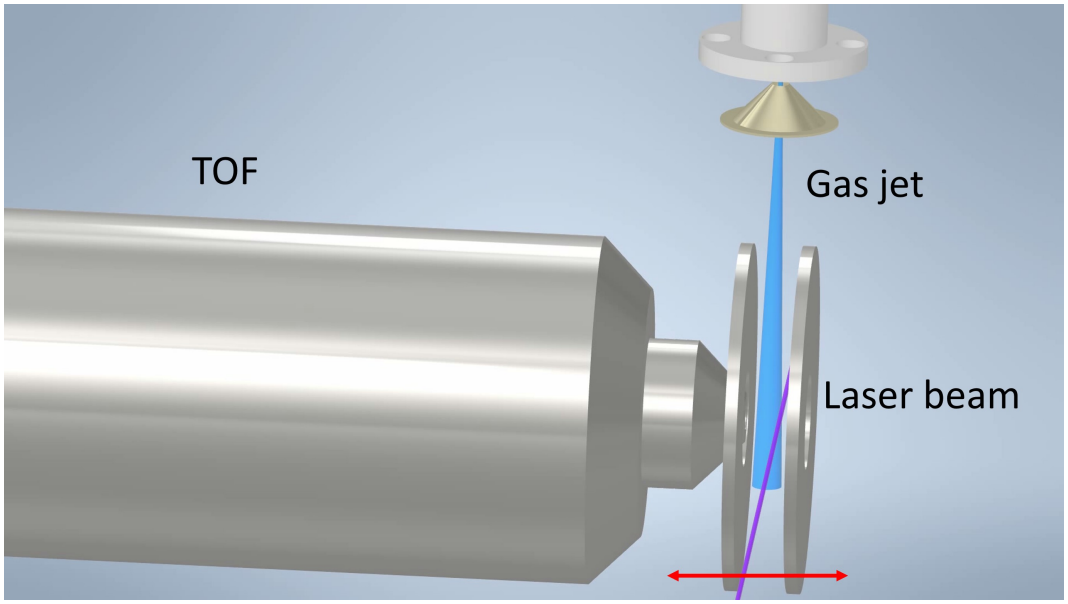

Figure 4.1.1: Schematic representation of the relative orthogonal motion of the gas jet with respect to the laser beam as performed during the experiment

To finely optimize the alignment, the electron signal of the TOF spectrometer is acquired. In particular, a train of attosecond pulses, generated in Krypton at pressure $1.4 \cdot 10^{-3}$ $mbar$, has been used to ionize the carrier gas. This spectrum has been acquired with a MCP detector (fig. 4.1.2 bottom panel), where two voltages have been set: high voltage $HV = 2.73kV$ and low voltage $LV = 0.68kV$. During all these experiments these two voltages will be maintained fixed. The electron signal is optimized by looking both at the shape of the photo-electrons, that should match the XUV spectrum, as well as the total counts (fig. 4.1.2 top panel). The labels in both panels refer to the harmonic order.

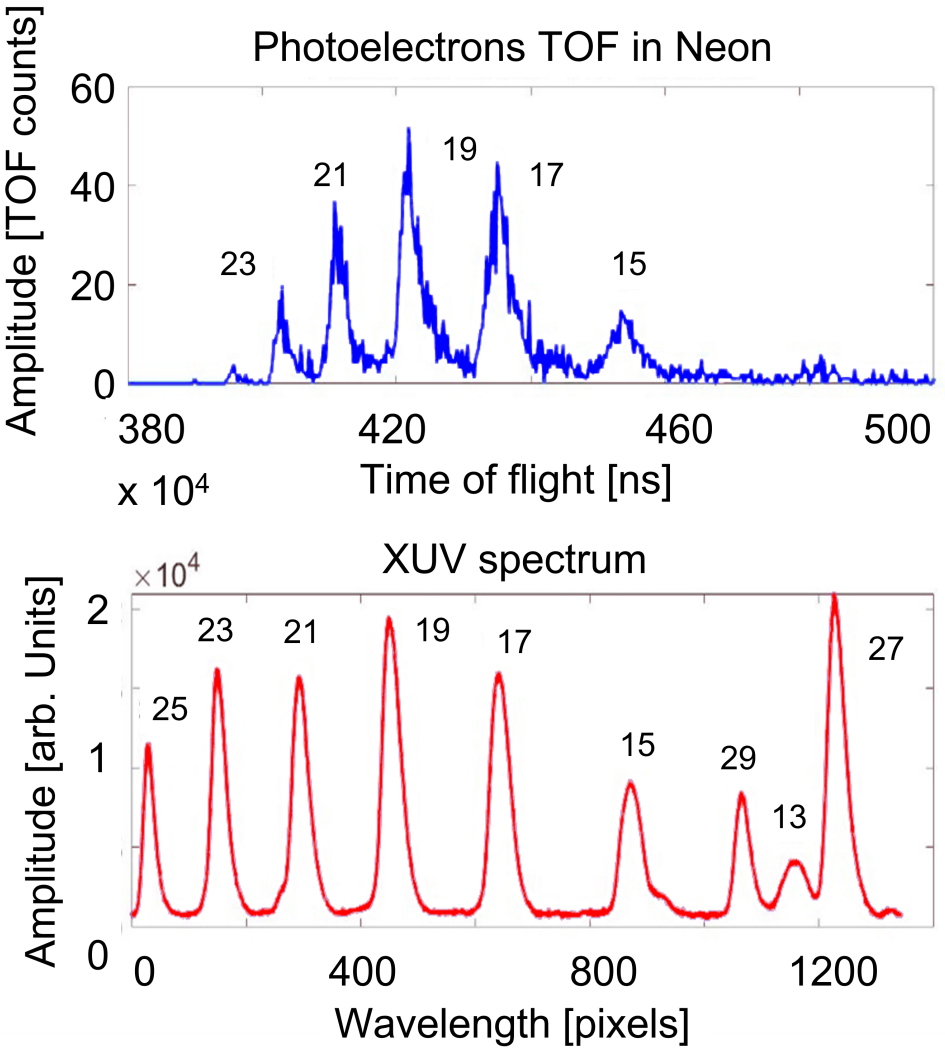

Figure 4.1.2: Photo-electron spectrum acquired for 20 seconds (top panel) generated by the interaction of XUV pulses and Neon, for values of MCP voltage= 2.2kV, lens/drift= 10 V.
XUV spectrum generated in Krypton at pressure $1.4 \cdot 10^{-3}$ $mbar$, starting from an IR pulse (bottom panel). The labels indicate the harmonic orders.

4.1.2 Pulsed valve characterization

At this point, all the components are perfectly aligned and the valve can be tested in pulsed mode. It has been made operating at the maximum speed with an aperture time of $220\mu s$. In order to obtain the perfect synchronization between the train of pulses and the gas jet pulses (as ideally represented in fig. 3.2.2), the delay between the aperture time of the valve and the laser pulses can be varied. The observable that is measured is the ion yield of the carrier gas (Neon) as a function of the laser-valve delay. For a given time, the ion spectra have been acquired for $30s$, under the following conditions:

- MCP voltage= $2.0kV$
- Lens and Drift= $2.0kV$
- Repeller and Extraction electrodes= $155V$

The maximum ion yield has been measured for delays equal to $655\mu s$, the overall scan is reported in fig. 4.1.3, where a Gaussian fit has been performed to characterize the data points. The normalization has been performed with respect to the highest peak detected.

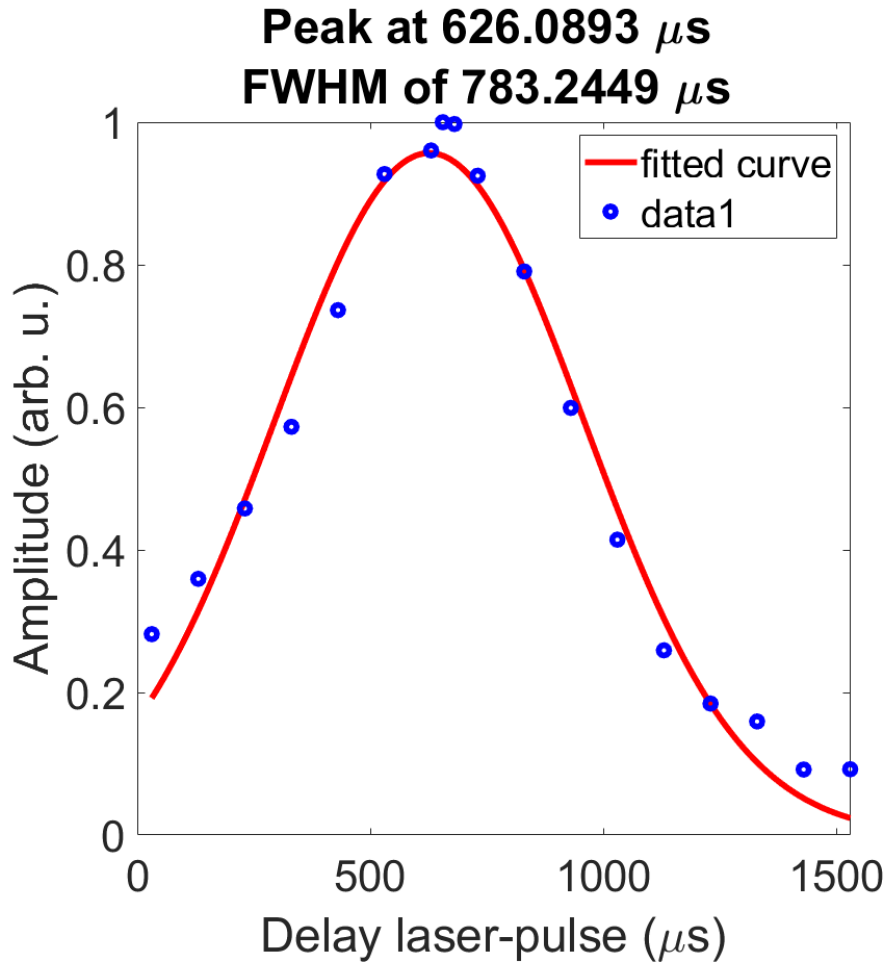

Figure 4.1.3: Neon quantum yield (blue dots) as a function of the aperture time of the valve and the laser pulses delay, along with an estimated duration of the gas-jet for aperture time of $220\mu s$. The values have been normalized with respect to the maximum amplitude.

Through this analysis, it is possible to estimate the gas jet pulse duration (as the *Full Width at Half Maximum* ($FWHM$)) that is in the order of $800\mu s$. It is thus clear that the gas is much broader in time than the required value. Of course, this represents just a broad estimate, without any intention of giving a sound measure of the gas jet

duration. Inevitably, there are sources of fluctuations, first in the harmonics that ionize the sample but also in the electronic acquisition which presents an intrinsic noise as well as a quantization error due to the Analog to Digital converter, which has $8bits$.

Dependence on the time aperture of the valve

The next parameter that can be modified is the aperture time of the valve. Intuitively, if the aperture time decreases less gas can flow through the skimmer, but the contrast between the peak of the Neon quantum yield synchronized with the laser pulses and the other nine peaks can increase, representing an indirect proof of the improved temporal confinement of the gas jet. The experimental conditions are the ones described above ($n.v. = 302$, back-pressure $= 2\ bar$ and valve-skimmer distance $= 2mm$), the only parameters that have been adjusted are the delay between the valve aperture and the laser pulses and the needle value that has been modified to achieve a fixed pressure in the TOF chambers of $P_{TOF} = 9.55 \cdot 10^{-8} mbar$.
Two aperture time have been tested: $220\mu s$ and $120\mu s$, the results are shown in fig. 4.1.4, which represent the signals taken with an oscilloscope. This signal represents the total photo-ions spectrum sampled at each ms: a single peak is a "collapsed"ion spectrum, similar to the one in fig. 1.1.5, but, due to the compression of the time-axis, only the carrier peak stands out. These signals follow the frequency repetitions of the laser: ideally a contrast of $1 : 0$ would mean that the laser and the gas jet are perfectly syncronized and the get is well confined. Similar considerations can be made for the noisy acquisitions.

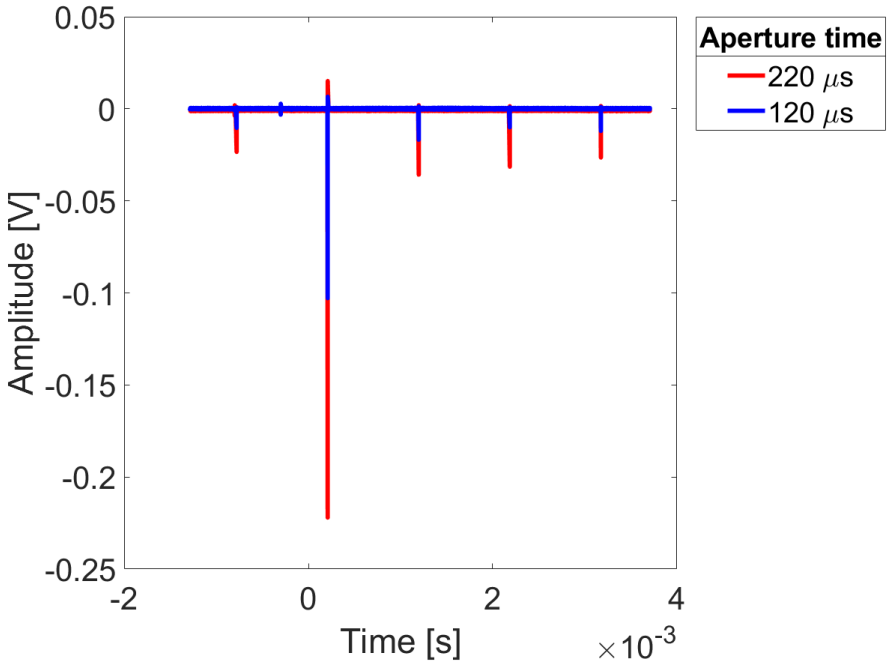

Figure 4.1.4: Ion yield recorded by an oscilloscope as a function of time for different time aperture of the valve ($220\mu s$ (red curve) and $120\mu s$ (blue one)) over a time window of $4ms$

It is represented a time window of $5ms$: while the contrast between the time 0 and the adjacent peak is $1:5$ for $220\mu s$, it rises up to $1:18$ for $120\mu s$ of valve aperture time, only if the pressure in the biochamber is decreased by an order of magnitude. Nevertheless, this improvement is at cost of a lower peak intensity for the shorter time aperture of the valve.
These spectra have been acquired for 30 seconds.

Dependence on the back-pressure

As another case study, the back-pressure has been varied. In particular, even though it is not possible to retrieve their exact values, the pressure values in the biochamber are reported, since they are proportional to the corresponding back-pressure. The first case (green curve) corresponds to a $P_{bio} = 1.17 \cdot 10^{-4} mbar$, the second case (blue curve) to a $P_{bio} = 2.80 \cdot 10^{-4} mbar$ and the last one (red curve) to a $P_{bio} = 4.17 \cdot 10^{-4} mbar$. The corresponding pressure in the TOF chambers are reported in the plot, fig. 4.1.5. In this case, the oscilloscope signal is shown for a time window of $10ms$: the first peak corresponds to the laser pulse that is synchronized to the central part of the gas jet, the other peaks are signals that are the results of the interaction of the other 9 laser pulses with the residual gas. Similar considerations of previous chart can be made even here: the peak that can be monitored as a function of the time delay is the one of the carrier gas that stands out in a collapsed time axis.

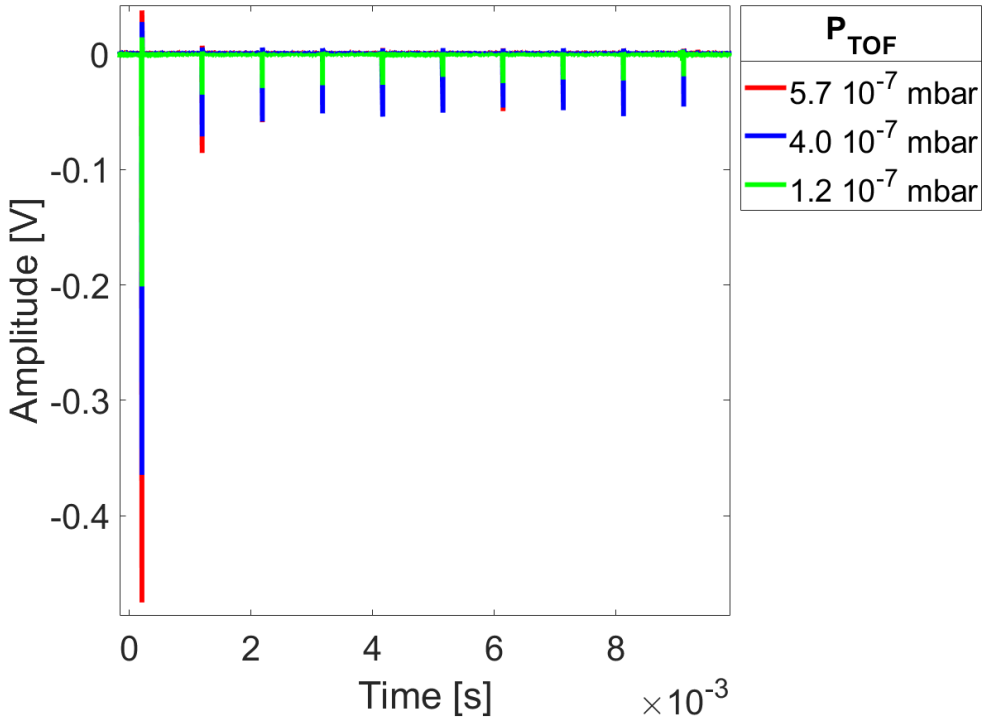

Figure 4.1.5: Ion yield recorded by an oscilloscope as a function of time for different back-pressure (the first case (green curve) corresponds to a $P_{bio} = 1.17 \cdot 10^{-4} mbar$, the second case (blue curve) to a $P_{bio} = 2.80 \cdot 10^{-4} mbar$ and the last one (red curve) to a $P_{bio} = 4.17 \cdot 10^{-4} mbar$), over a time window of $10ms$.

An increase in pressure corresponds to a higher quantum yield peak, but the contrast between the central peak and the adjacent does not change much: for the first case it is 1:6, for the second 1:7 and for the last 1:8.

Comparison between continuous and pulsed modes

At this point, it is interesting to compare the efficiency between the continuous and the pulsed mode for the Parker valve. In particular, three signals can be compared

1. The CW signal, which corresponds to the valve operating in continuous mode and the train of attosecond pulses continuously ionizing the molecules.
2. The "100 Hz signal"corresponds to the valve operating at $100Hz$ and a signal that sums up only the laser shots synchronized with the valve operating at $100Hz$.
3. The "1 kHz signal"corresponds to the valve operating at $100Hz$ and it is an average signal between the single shot synchronized with the gas jet and the remaining nine pulses.

Working at similar P_{TOF}, reported in the chart (fig. 4.1.6), the comparison among these three signals is displayed below. It has to be mentioned that the pressure inside the TOF spectrometer is the limiting parameter. In fact, it cannot reach $10^{-5} mbar$ in order to not damage the MCP detector.

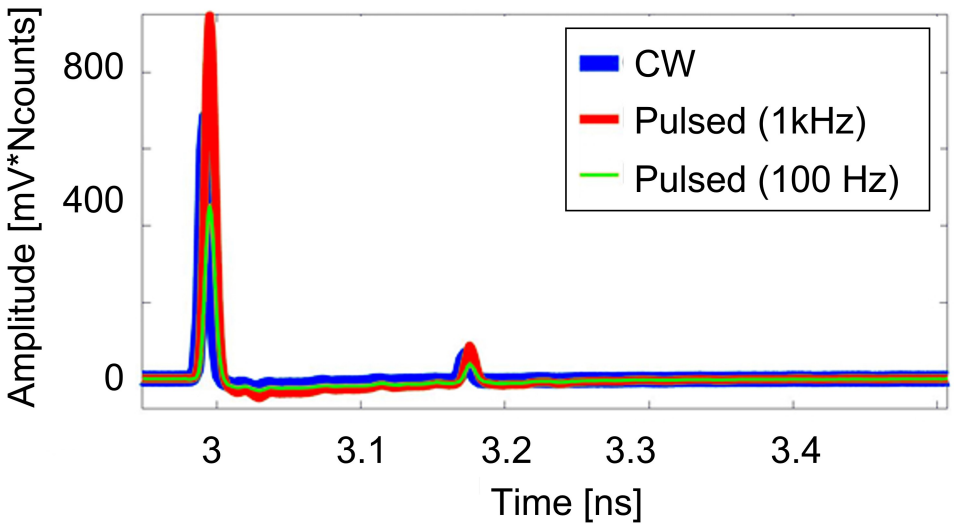

Figure 4.1.6: Ion yield comparison between CW, "100 Hz"and "1 kHz"signals, in terms of number of counts, for the carrier gas (Ne)

For similar pressure in the TOF chamber, the pulsed mode is not significantly better than the CW case. By looking at the carrier gas, both the "100 Hz signal"and the "1 kHz signal"signals are similar, with a small increase in the counts for the third case, prove of the fact that the time behaviour of the gas flow is not satisfactory due to its spread.

Valve-Skimmer distance variation

In all the previous tests, the distance between the valve and the skimmer has been kept at $2mm$. It is interesting to explore the carrier signal and the contrast variation as a function of this distance.

The valve is operating at $100Hz$: a first test has been performed by varying the distance between these two components, keeping the pressure of the bio-source constant ($P_{bio} = 1.6 \cdot 10^{-4} mbar$). For each distance, that has been varied from $2mm$ up to $23mm$, the delays have been optimized. The TOF pressure varies in a range from $1.13 \cdot 10^{-7} mbar$ for $2mm$ to $2.7810^{-8} mbar$ for $23mm$. In order to understand if the time confinement is improved, the contrast, calculated as the ratio between the signal related to the first and the second laser pulses, is monitored. Furthermore, the amplitude of the signal, recorded from the read-out card, is measured. For a single distance, the acquisition time for the read-out card has been $30s$.

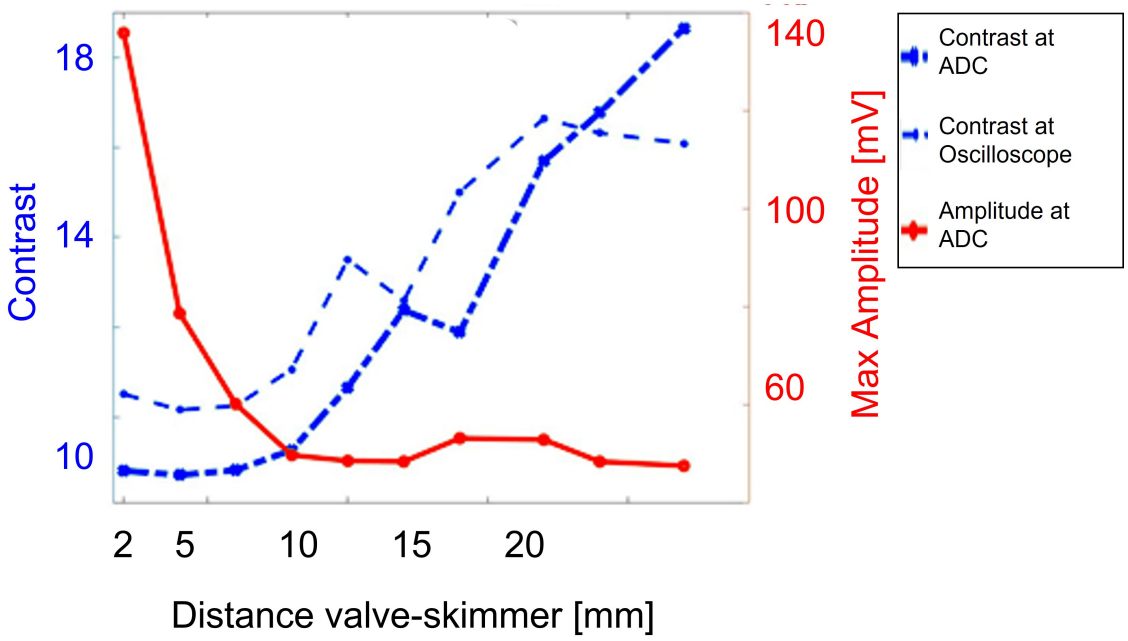

Figure 4.1.7: Amplitude signal and contrasts (at ADC and Oscilloscope) as a function of the valve-skimmer distance (ranging from 1 to 25 mm), for a fixed $P_{bio} = 1.6 \cdot 10^{-4} mbar$

It is interesting to notice that, while the contrast improves for larger valve-skimmer distances, the amplitude signal shows a clear drop, worsening the capability of acquisition. In this plot, two contrasts are mentioned:

- The Contrast at Analog-To-Digital Converter (ADC) represents the ratio between the signals at the acquisition card, that has been made comparing the area of the carrier gas peak, coming from the first and the second laser pulses.
- The Contrast at Oscilloscope, instead, represents the ratio between the peak of the carrier gas at the first and the second laser pulses.

The first parameter is intrinsically less noisy than the second, where an area is computed, instead of the height of the carrier gas peak that is more subject to variations. Nevertheless, both contrasts improve as the distance between the valve and the skimmer increases with the drawback of losing counts on the MCP.
An analogous experiment can be performed but instead of keeping constant the pressure in the bio-chamber, it has been maintained steady the pressure in the TOF chamber ($P_{TOF} = 1.1 \cdot 10^{-7} mbar$) that is effectively the one where the gas interacts with the laser pulses. In this case, P_{bio} varies in a range from $1.57 \cdot 10^{-4} mbar$, at $2mm$, to $1.36 \cdot 10^{-3} mbar$ for $18mm$, indication of the fact that less molecules will pass through the skimmer and remain localize in the bio chamber. The results of the signal amplitude and the contrast (at the read-out card, indicated as ADC, and at the oscilloscope) are displayed in fig. 4.1.8.

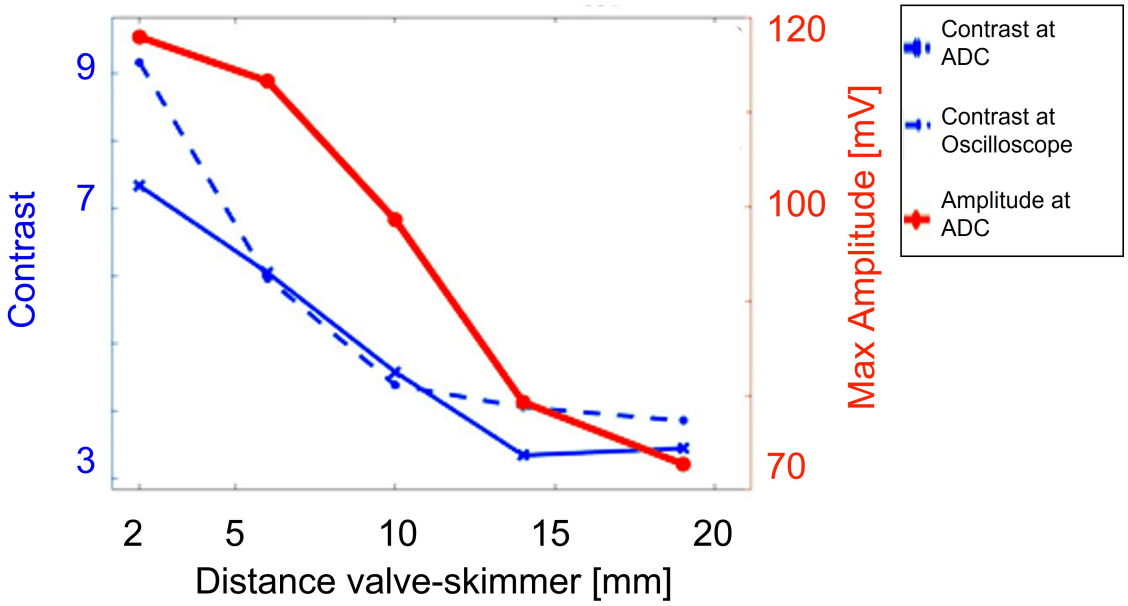

Figure 4.1.8: Amplitude signal and contrasts (at ADC and Oscilloscope) as a function of the valve-skimmer distance (ranging from 1 to 20 mm), for a fixed $P_{TOF} = 1.1 \cdot 10^{-7} mbar$

In contrast with the former case, both the signal and the contrasts show a decreasing trend as the distance increases: this is thus detrimental for any condition and the results are thus unsatisfactory.

4.2 Test of the Parker valve with the oven

After having fully characterized the setup without the oven, it is of high interest to understand if the gas jet behaves differently in presence of the ceramic insulator and the oven structure, (fig.3.2.1). In fact, it is with this configuration that the analyte will be sublimated and transported by the carrier gas for the pump-probe experiments.

4.2.1 Alignment optimizations

Following the procedure described in sec. 4.1.1, the alignment of the valve-oven structure with respect to the skimmer has been roughly performed looking at the pressure in the vacuum chambers, working in CW conditions. As before, Neon was used as carrier gas with a back pressure of $2bar$ and a needle value of 300, then after having analyzed the photo electrons signal, the alignment has been further refined.

4.2.2 Pulsed valve characterization

Also in this case, the valve has been switched to pulsed mode (frequency of $100Hz$). The working conditions are the same as before ($220\mu s$ as aperture time, $2mm$ distance between the skimmer and the valve), and a first analysis on the time gas-jet shape is reported. The delay between the valve aperture and the laser shots have been varied and for each delay the ion spectra have been acquired. Each point represents the Neon peak integrated for 30 seconds.

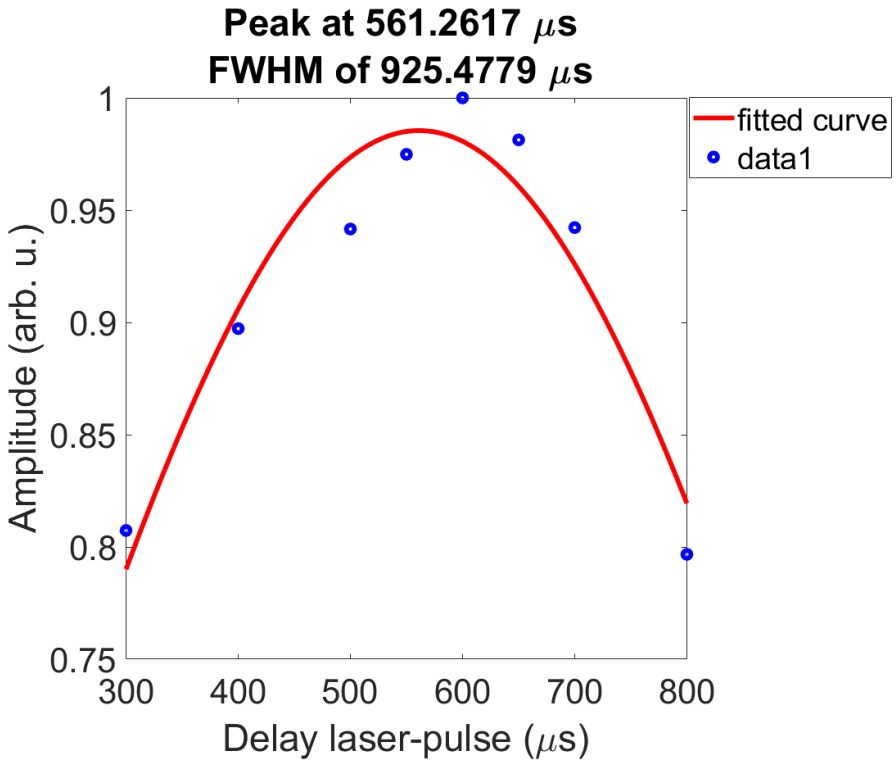

Figure 4.2.1: Neon quantum yield as a function of the aperture time of the valve and the laser pulses delay, along with an estimated duration of the gas-jet for aperture time of $220\mu s$, at $2mm$ from the skimmer. The signal has been normalized to the maximum amplitude.

In this case, it can be noticed that the time shape of the gas jet is worsened: the points look almost constant in a large range of delays (from 400 to $800\mu s$) and the Gaussian fit does not give a good result. The gas jet shape in time has increasingly degraded.
The situation changes when considering a distance between the valve and the skimmer of $12mm$, but at the cost of a decrease in the total amplitude signal. The gas jet shape is shown, as a function of the different delays, in fig. 4.2.2. The duration is consistent with previous experiments but the Gaussian fit is still less satisfactory than the tests with the valve only.

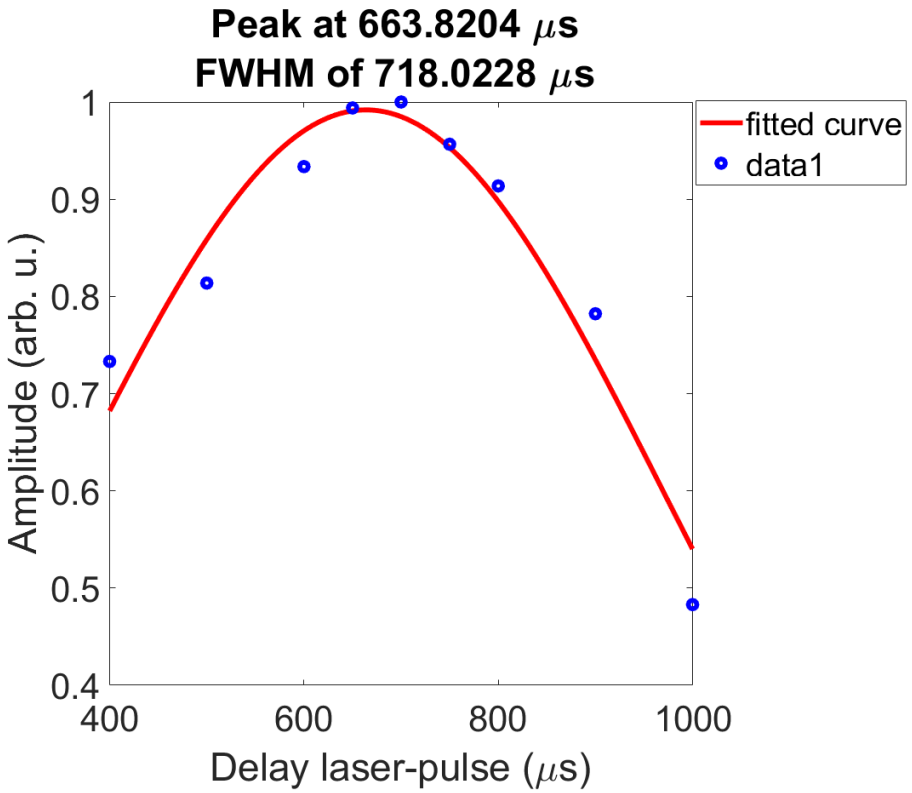

Figure 4.2.2: Neon quantum yield as a function of the aperture time of the valve and the laser pulses delay, along with an estimated duration of the gas-jet for aperture time of $220\mu s$, at $12mm$ from the skimmer. The signal has been normalized to the maximum amplitude.

For this reason, it is pointless to characterize the contrasts as in previous tests, since the asynchronized laser pulses will interact even more with the large tails of the gas jet. Hence, it is interesting only to compare if the total signal increases with the upstream pressure. This is indeed satisfied: in fig. 4.2.3, where two different back-pressure (corresponding to a $P_{bio} = 1.0 \cdot 10^{-4} mbar$ and $P_{bio} = 7.0 \cdot 10^{-4} mbar$) are compared, this behaviour is clearly shown in the chart after an integration time of $30s$ and can be easily understood. This gain only reflects an increase in the number of atoms rather than an improvement introduced by the pulsed valve.

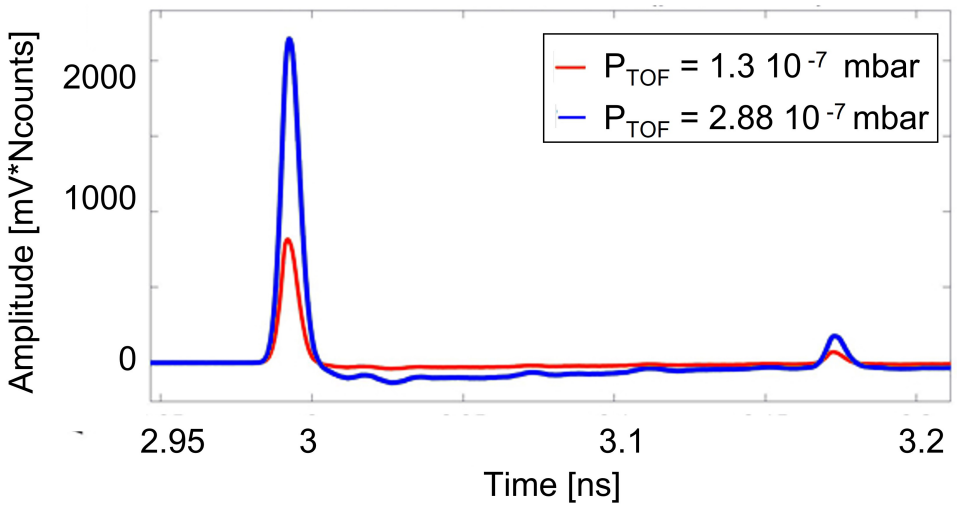

Figure 4.2.3: Comparison in the number of counts of the effect on the increase of the back-pressure in the pulsed mode for $P_{bio} = 1.0 \cdot 10^{-4} mbar$ (red curve) and $P_{bio} = 7.0 \cdot 10^{-4} mbar$ (blue curve), representing the carrier gas peak (Ne)

For completeness, the ion signal comparison in the situation with and without the oven is depicted, fig. 4.2.4. For the same P_{bio}, and integration time ($30s$), looking at the "1 kHz channel", the signals show a slight drop in amplitude in the configuration with the oven.

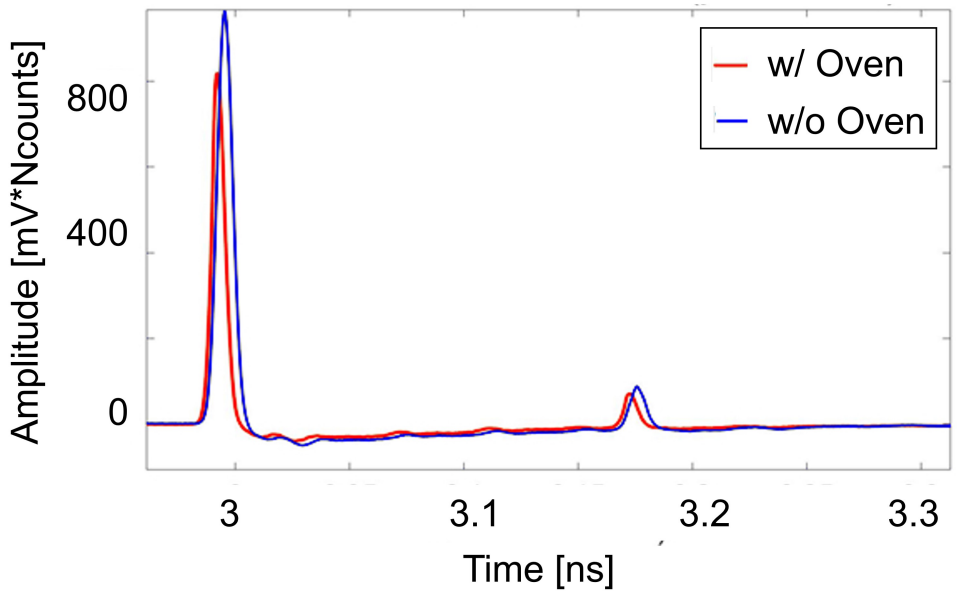

Figure 4.2.4: Comparison of the ion yield signal, recorded at the read-out card with the oven (red curve) and without the oven (blue curve), representing the carrier gas peak (Ne)

An additional degree of freedom that can be tested is the increase in temperature of the oven. The question that may arise is whether heating up the oven, attached downstream to the valve, significantly changes the already unsatisfactory performances of the valve. Since the gas jet temporal shape has been seen to be satisfactory for $12mm$ distance from the skimmer, the comparison has been performed under these conditions. Interestingly, the shape of the gas jet does not change much comparing the oven at room temperature (20°) with respect to 200°. Also in this case, each value represents the peak value of the carrier gas acquired for $30s$.

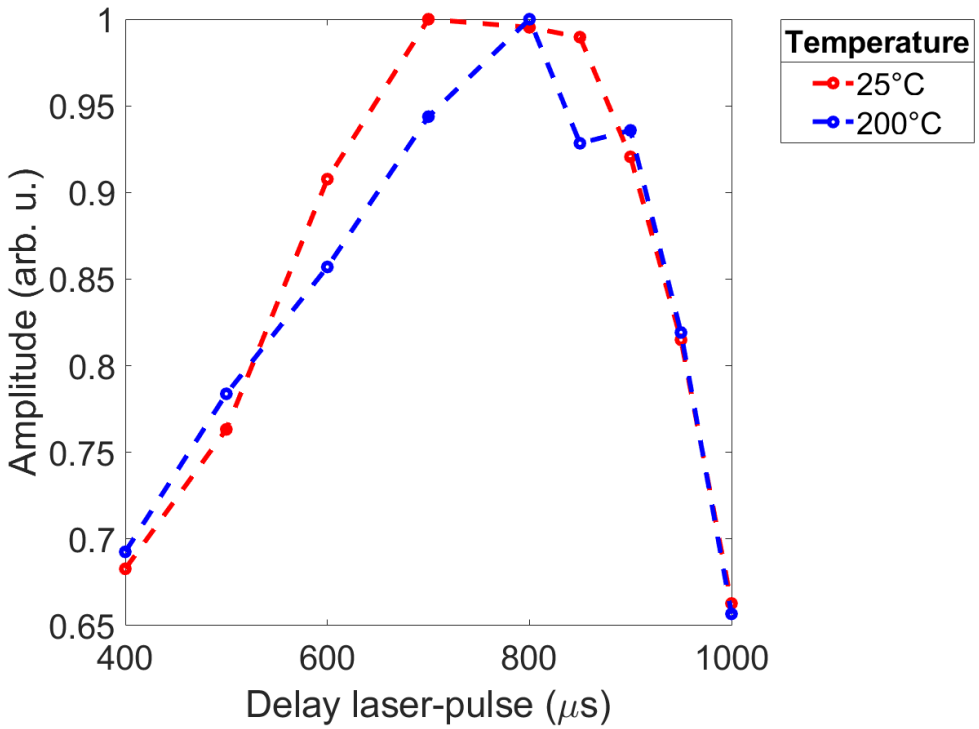

Figure 4.2.5: Comparison between the Neon quantum yield as a function of the aperture time of the valve and the laser pulses delay at $12mm$ from the skimmer for two different temperatures of the oven: 25° and 200°

It is actually not much surprising since the Neon stream is cold and quickly crosses the large channel of the oven at higher temperature.

4.3 Conclusions

In this section, the gas properties exiting from the valve and from the oven have been analyzed. The main conclusions can be listed as follow:

- The gas jet is broad in space, with a width of almost $3.5mm$.
- The gas jet is also broad in time (for about $800\mu s$ in presence of the oven, at a valve-skimmer distance equal to $2mm$, and $800\mu s$, for the same valve-skimmer distance), since the contrast is very poor ($\approx 1:10$ for a valve-skimmer distance equal to $2mm$) if positioned very closed to the skimmer in order to obtain a larger signal.
- At higher distances between the skimmer and the valve, given the pressure where the gas jet expands, we can achieve a better temporal confinement of the gas jet and, hence, a better contrast. This came at the expense of the TOF signal amplitude (less molecules are injected into the TOF chamber). If we try to recover the TOF signal by increasing the bio-chamber pressure, due to turbulence we lose the contrast gained and the overall signal remains unacceptably low.
- The back pressure can be increased in order to improve the experimental signal, but due to the time and space broadening this would translate into an increase amount of molecules that will not interact with the laser pulses. Furthermore, the increase in pressure is limited by the vacuum pump load.

Due to these unsatisfactory results, all these hypothesis should be tested using a well established approach. In order to both verify previous statements and understand what could be improved in the valve-oven design, the Direct Simulation Monte Carlo (DSMC) method should be exploited to simulate the gas flow from the valve and its interaction with the skimmer.

Chapter 5

Direct Simulation Monte-Carlo (DSMC)

To understand how the gas, emitted by the valve, flows into a vacuum chamber, a mathematical modelling of this dynamics is required. Over time, different models have been proposed to mathematically represent the fluid dynamics properties of a gas, the most promising and employed method is the Direct Simulation Monte Carlo (DSMC) proposed by Bird in 1960s [8]. This is one of the most sound theoretical methods that has been used, thanks to its flexibility and versatility.

5.1 Gas flow modeling

In general, a gas can be represented exploiting microscopic or macroscopic models. The Navier - Stokes equations model the gas as a continuum: the macroscopic observables are the dependent variables, while the spatial coordinates and time are the independent ones. The microscopic model, instead, relies on the Boltzmann equation that assigns to the particle a typical probability distribution for its position and momentum.
Based on the rarefaction of the gas, the validity of different models hold or fail: to estimate it, the Knudsen number (K_n) is introduced.
K_n is a dimensionless number defined as the ratio of the molecular mean-free-path (λ) to characteristic dimension (L) [8].

$$K_n = \frac{\lambda}{L} \tag{5.1.1}$$

The mean-free-path represents the average distance between two subsequent molecular collisions, while the characteristic dimension is a length that defines the scale of the system: it could be the dimension of the chamber where the gas expands or the dimension of the nozzle through which the gas is passing. In the free space, it is typically the radius (or the diameter) of the species of interest.
Due to the vagueness in the definition of an overall Knudsen number for the whole flow, it is necessary to introduce a *local* Knudsen number, where the characteristic dimension L is defined as:

$$L = \frac{\rho}{d\rho/dx} \tag{5.1.2}$$

where ρ is the density of the fluid, and $d\rho/dx$ represents the variation of the density (in other words L represents the length of the macroscopic gradients [8]). Depending on the value of K_n different regimes can be identified [19]:

- $K_n < 0.01$: *continuum flow*, the mean free path is extremely small compared to the characteristic dimension, thus collisions between molecules happen very frequently and the fluid can be considered as a continuum.
- $10^{-2} < K_n < 0.1$: *slip flow*
- $0.1 < K_n < 10$: *transitional flow*
- $K_n > 10$: *free-molecular flow*, the mean free path is large compared to the characteristic dimension.

The validity of different models depends on the value of the Knudsen number, a summary of all the possible approaches is reported in fig. 5.1.1, reworked from [8].

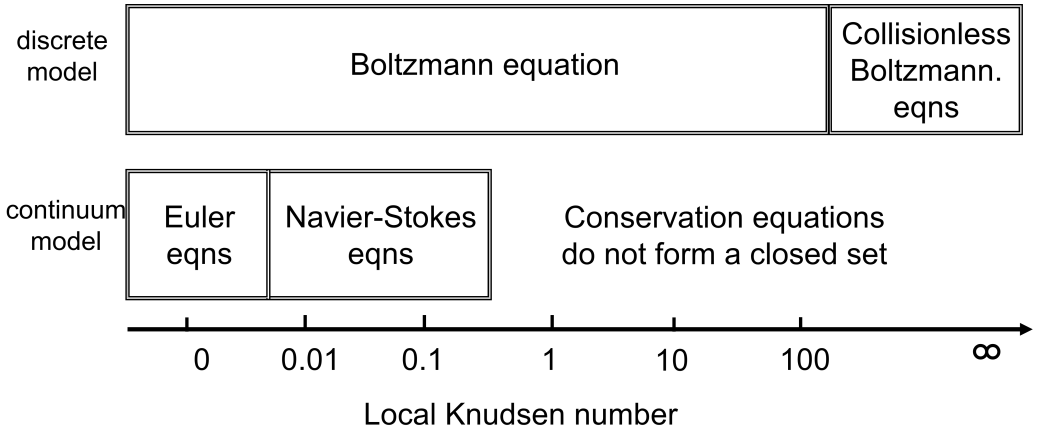

Figure 5.1.1: Schematic representation of the different models validity based on the Knudsen number, adapted from [8]

From this chart, the continuum flow model, represented by the Navier-Stokes equations, is valid only for small local Knudsen number (up to $K_n \approx 0.1$), while when $K_n \to 0$ the fluid can be represented by the Euler equation [7], that is the limit case when the viscosity and the thermal conductivity of the fluid are zero [32]. On the opposite case, if $K_n \to \infty$ the flow is almost free molecular, for which inter molecular collisions are negligible.

In this framework the Direct Monte-Carlo Simulation (DSMC) is a numerical method that treats the gas as a discrete cluster of molecules, whose validity ranges from small to large Knudsen numbers. This methodology was introduced by G.A. Bird in the 60s and it has been applied in many fields, from aerospace engineer [20] to micro fluidity [2] as well as gas flows expanding in vacuum [13]. Even though it can be reasonably applied within a large range of regimes, its robustness has been demonstrated for sufficiently rarefied gas. It is widely believe that the DSMC represents an exact numerical solution of the Boltzmann equation [5], though recent studies suggest that the connection is not direct [30]. For the purpose of this thesis the classical relationship between the DSMC and the Boltzmann equation is presented, in order to give particular emphasis on its functional principle.

5.2 Description of the simulation principle

The DSMC method is a numerical technique that models the gas flow in terms of thousands of *simulated molecules* that embody a certain number of *real molecules*. First of all, one has to define the physical space through which the gas is flowing by specifying the boundary conditions of the space[1]and the nature of the molecular collision. Based on these factors, starting from known initial conditions, for each molecule the position and the velocity coordinates are saved in the computer and they are continuously updated in time. The steady state flow can be reached only if particular conditions are met at large times[2], otherwise unsteady flow is the common state during the simulation.
To properly address the problem with a computer, the physical space is discretized in both space and time. A spatial dimension of the cell Δx is defined, with the condition that the changes in the gas properties between two adjacent cells Δx_i and Δx_j are not abrupt but sufficiently smooth; time is divided into steps Δt, sufficiently smaller compared to the time between two subsequent molecular collisions. Nevertheless, it is not required that Δx or Δt should be fixed in space and time but they can vary freely within previous constraints.
The idea behind the DSMC method is simple and can be summarized in three steps:

1. In a time interval Δt the molecules are moving freely for a distance suitable to the initial velocities.

2. A set of collisions among the molecules is chosen, accordingly to the given Δt: the velocity components of the molecules that have collided are calculated.

3. Such velocity components after the collisions are replaced to the ones before the collision, only to the subset of molecules involved in a collision.

A more refined scheme is reported in fig. 5.2.1 where the flow chart of the DSMC is reported.

[1] vacuum, stream of reference gas, symmetric plane etc...

[2] If the aim of the simulation is to study the steady flow onto a defined volume, the initial state of the simulation should be a uniform stream in which the volume is inserted at time 0

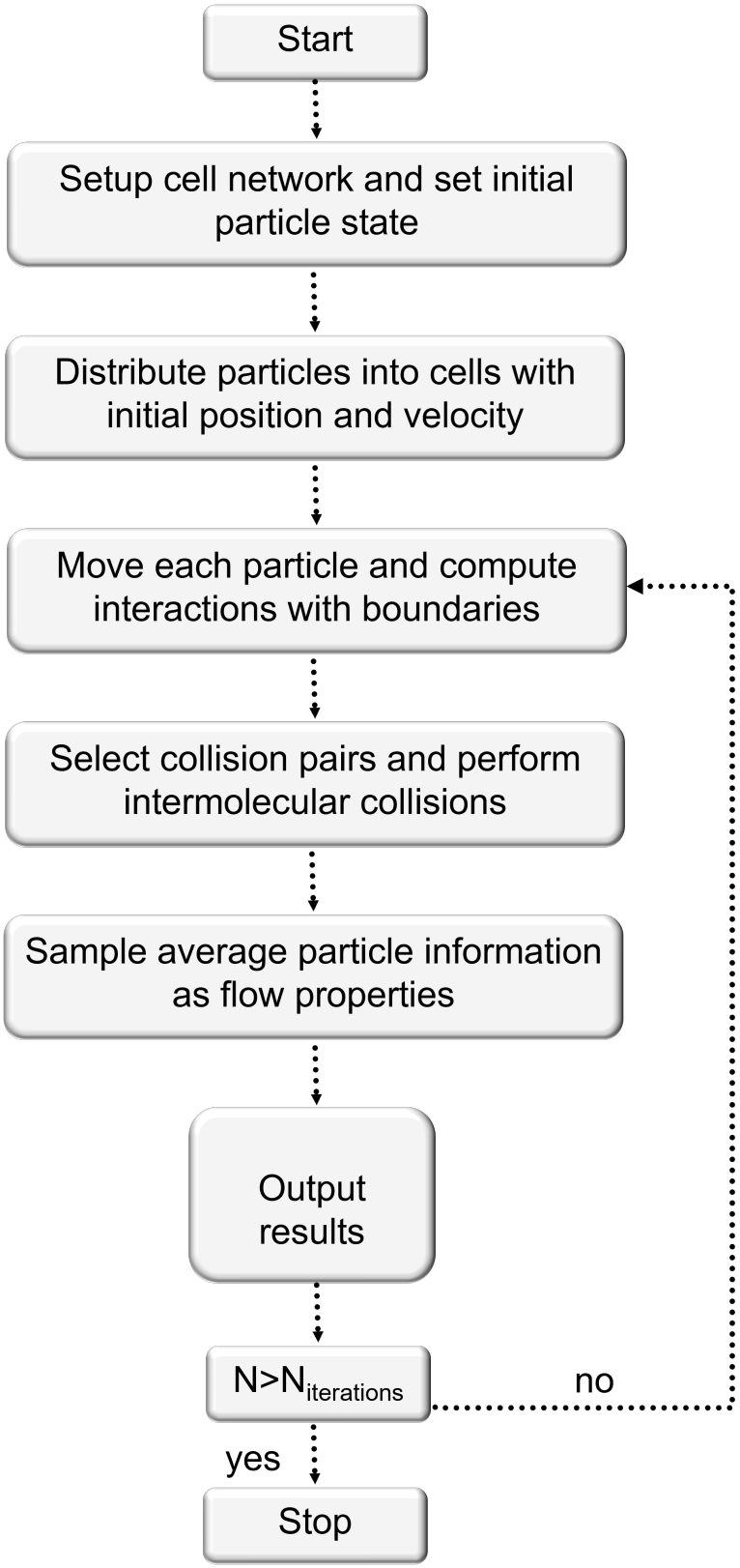

Figure 5.2.1: DSMC scheme flow highlighting its main steps, from [18]

The discretization in time inevitably distort the molecular paths, it is thus clear why the Δt should be sufficiently small compared to the mean free time (i.e., the mean time between two successive collisions for a single molecule).
The toughest part of the simulation is to estimate the subset of molecules that can collide in a time Δt. To make it feasible a collisional model needs to be introduced and studied.
As pointed out at the beginning of this section, this method interprets the gas flow as formed by a certain number of *simulated molecules*: each molecule does not represent a single *physical molecule* but a certain cluster of them. Evidently, the physical properties of a single *simulated molecule* represents the average value of the same physical properties of a certain cluster of *physical molecules* (e.g., the velocity of a *simulated molecule* is the average value of some *physical molecules*).

5.2.1 Binary Collision - Cross Section definition

In order to understand which are the values of the velocities after the collisions, the assumptions and the theoretical models on which the simulations rely on need to be introduced. In general, the force between two *neutral* molecules, as a function of the relative distance r, has a shape similar to the one represented in fig. 5.2.2.

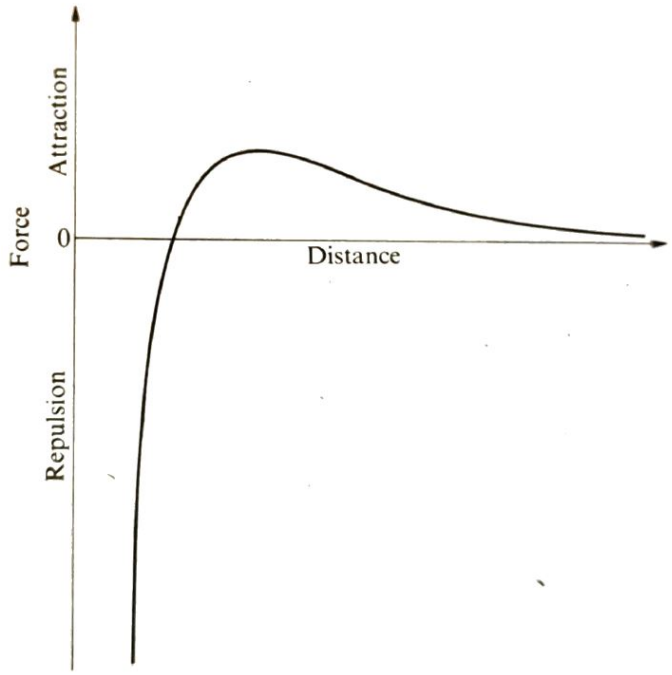

Figure 5.2.2: Schematic representation of the inter-molecular force between two molecules as a function of their distance,[6]

For very large distances the force between two molecules is effectively zero, while for much shorter distance, in the limit for which $r \to 0$ the force is repulsive. By summing up these two contributions the total curve is obtained, in which a maximum in the force (attraction) comes out.

The probability that two molecules collide is represented by the total cross section σ_T, whose value depends on the method chosen to model the molecules. The collisions among molecules in the gas phase can be modelled as pair collision within two particles: all the calculation will be carried out according to the elastic collision assumption, for which the total momentum and the total energy is preserved. To fulfil this aim, let's consider two molecules with masses $m_{1,2}$, characterized by pre-collision velocities $\boldsymbol{c}_{1,2}$ and post-collision velocities $\boldsymbol{c}^*_{1,2}$. The equations that govern this problem are the following

$$m_1\boldsymbol{c}_1 + m_2\boldsymbol{c}_2 = m_1\boldsymbol{c}^*_1 + m_2\boldsymbol{c}^*_2 = (m_1 + m_2)\boldsymbol{c}_m \tag{5.2.1}$$

$$m_1 c_1^2 + m_2 c_2^2 = m_1 c_1^{*2} + m_2 c_2^{*2} \tag{5.2.2}$$

where the eqn.5.2.1 refers to the momentum conservation and eqn.5.2.2 refers to kinetic energy conservation. It is trivial to realize that the center of mass, with velocity $\boldsymbol{c}_m$, is not affected by the collision at all (from eqn. 5.2.1: $\boldsymbol{c}_m = \boldsymbol{c}^*_m$).
Introducing the relative velocity $\boldsymbol{c}_r = \boldsymbol{c}_1 - \boldsymbol{c}_2$ before the collision, and $\boldsymbol{c}^*_r = \boldsymbol{c}^*_1 - \boldsymbol{c}^*_2$ after the collision, the velocities $\boldsymbol{c}_{1,2}$ and $\boldsymbol{c}^*_{1,2}$ can be expressed in terms of the relative velocities and the velocity of the center of mass, showing that these two velocities are anti-parallel. Declaratively, the velocities of the molecules before the interaction are reported:

$$\boldsymbol{c}_1 = \boldsymbol{c}_m + \frac{m_2}{m_1 + m_2}\boldsymbol{c}_r \tag{5.2.3}$$

$$\boldsymbol{c}_2 = \boldsymbol{c}_m - \frac{m_2}{m_1 + m_2}\boldsymbol{c}_r \tag{5.2.4}$$

Analogous equations hold for the post collisional velocities. By substituting these expression into eqn.5.2.2, one obtains

$$m_1 c_1^2 + m_2 c_2^2 = (m_1 + m_2)c_m^2 + m_r c_r^2 \tag{5.2.5}$$

$$m_1 c_1^{*2} + m_2 c_2^{*2} = (m_1 + m_2)c_m^{*2} + m_r c_r^{*2} \tag{5.2.6}$$

where $m_r = \frac{m_1 m_2}{m_1 + m_2}$ is known as reduced mass. Thus, before and after the collision not only the center of mass' velocity is constant but also the relative velocity $c_r = c^*_r$ in magnitude. It follows that to calculate the post collisional velocities it is sufficient to determine the change in the direction of the relative velocity vector $\boldsymbol{c}_r$. Hence, one can decide to look at the at the motion of the molecule m_1 with respect to the molecule m_2 or alternatively to look at the motion of the mass m_r relative to the scattering point. Therefore, two impact parameters b and χ are introduced and explained, fig. 5.2.3.

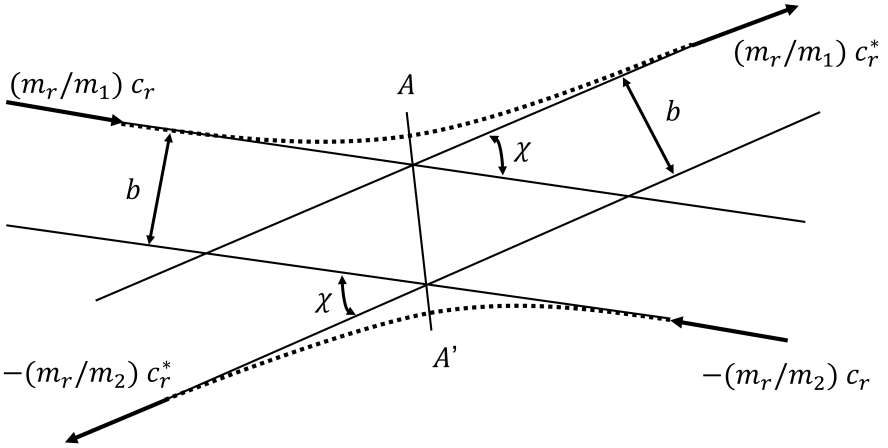

Figure 5.2.3: Representation of the trajectories of two molecules interaction: the parameter b and χ are defined, [6]

b represents the closest distance between the trajectory of the center of mass and the initial molecule trajectory, while χ is the angle between the perturbed and the unperturbed trajectories. Both of them will be useful in the definition of a total cross section.
Once the latter is calculated, if one consider a gas that occupies a certain volume V, the number of molecules per unit volume, i.e., number density, is n, it is possible to define the mean collision rate ν,i.e., the inverse of the mean free time, by summing up all the possible collisions per unit time over a certain volume occupied by a density Δn:

$$\nu = \Sigma(\Delta n \sigma_T c_r) \tag{5.2.7}$$

where $c_r = c_t - c$ is the relative speed between the molecule test t and the rest of the molecules whose density is Δn. By multiplying and dividing by n, one can recognize the average value over all molecules in the sample, identified by the bar:

$$\nu = n\overline{\sigma_t c_r} \tag{5.2.8}$$

Different models to calculate the total cross-section, and thus the collision rate, are studied.

Hard Spheres

The simplest model that can be introduced represents the molecules as non-deformable rigid spheres with diameter d: two molecules collide if their distance is lower than the diameter, hence the total cross-section is:

$$\sigma_t = \pi d^2 \tag{5.2.9}$$

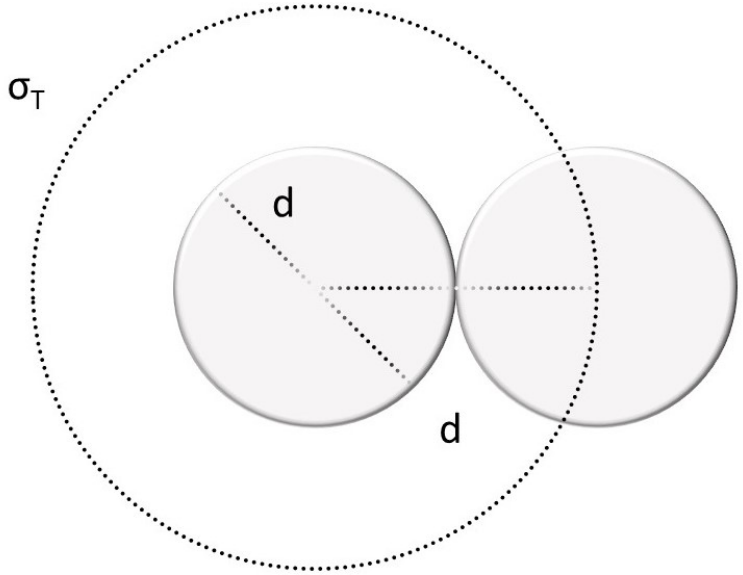

Figure 5.2.4: Cross Section interpretation for Hard Spheres model, representing two molecules of the same species and the same diameter d

The scattering from hard spheres is, thus, isotropic in the center of mass reference system.

Inverse power law model

A more refined model is represented by the *Inverse power law model* in which the Force F between two molecules is repulsive for small distances r, the coefficient η varies according to the molecules and the exact model considered.

$$F = \frac{k}{r^{\eta}} \tag{5.2.10}$$

This equation thus holds just when the molecules are sufficiently close to each other. It is important to notice that the *Hard Sphere model* is a limit case for $\eta \to \infty$. Exploiting the *Inverse power law model*, a general cross section can be calculated. To understand its expression a dimensionless impact parameter W_0 is introduced as:

$$W_0 = b \left(\frac{m_r c_r^2}{k} \right)^{\frac{1}{\eta - 1}} \tag{5.2.11}$$

where c_r and m_r were previously defined. It is possible to prove that the total cross section is:

$$\sigma_T = \pi W_{0,m}^2 \cdot \left(\frac{k}{m_r c_r^2} \right)^{\frac{2}{\eta - 1}} \tag{5.2.12}$$

where $W_{0,m}$ is an arbitrary cut-off maximum value for W_0 that is strictly related to the maximum value of angle χ.

Variable Hard spheres

While the inverse law model is a good representation of real molecules, though much complicated in its analysis, the hard sphere model excessively simplifies the physics, without taking into account that the cross section is actually dependent on the relative translational energy (i.e., $E_t = 1/2 m_r c_r^2$). By varying the temperature of the sample the collisions parameter should adapt too. Following these considerations, Bird introduced the Variable Hard Spheres (VHS) model in which the diameter d of the molecule is a function of the relative speed c_r. For example, following the inverse law with exponent μ, the diameter of the molecule becomes

$$d = d_{ref} \left(\frac{c_{r,ref}}{c_r} \right)^{\mu} \tag{5.2.13}$$

where $_{ref}$ denotes reference values for a particular temperature. Hence, in the cross section calculation the effective diameter d is introduced, which is a function of the relative speed with respect to a reference temperature condition. Overall, the total cross section for VHS model is

$$\sigma_T = \pi \left[d_{ref} \left(\frac{c_{r,ref}}{c_r} \right)^{\mu} \right]^2 \tag{5.2.14}$$

Variable Soft spheres

Another improvement is represented by the Variable Soft Spheres model (VSF), where instead of considering only isotropic scattering the possibility of anisotropicity is introduced. Hence, the scattering angle can be retrieved as:

$$\chi = 2 \cos^{-1} \left(\frac{b}{d} \right)^{\frac{1}{\alpha}} \tag{5.2.15}$$

where α is a parameter related to diffusivity: the VHS and the VSS models coincide when $\alpha = 1$.

5.2.2 Collision computation

Starting from the mean collision rate ν, eqn. 5.2.8, the collision probability is proportional to $\sigma_T \cdot c_r$. For example, since the *Inverse law* is one of the most general model, considering its cross section eqn.5.2.12, the total probability is proportional to:

$$\pi W_{0,m}^2 \cdot \left(\frac{k}{m_r} \right)^{\frac{2}{\eta-1}} c_r^{\frac{\eta-5}{\eta-1}} \tag{5.2.16}$$

for a fixed maximum angle χ, $W_{0,m}$ is constant and the probability is proportional to $c_r^{\frac{\eta-5}{\eta-1}}$: giving a direct method to choose collision pairs based on relative speed between molecules.
In particular for the hard sphere model, since $\eta \to \infty$, the probability is proportional

to the relative speed between molecules: this expression can be obtained substituting the value of σ_T given by eqn. 5.2.9.

$$\pi d^2 c_r \tag{5.2.17}$$

Analogous but more refined results can be obtained in case of VHS model, where instead of d and *effective* d is introduced. For each cell the maximum value of the probability $P_{max} = c_r(\sigma_T)_{max}$ is calculated and stored. At this point, two randomly chosen molecules are considered, if the probability of collisions is sufficiently high compared to the maximum one, the molecules are kept otherwise another couple is chosen, this is done through the *acceptance-rejection method* [6]. More precisely, while in the early development of this method a *Time Counter* was exploited [5], a more refined and fast one is the *No Time Counter* scheme. For each pair of molecules a *normalized* probability is calculated as

$$P_c = \frac{\sigma_T c_r}{(\sigma_T c_r)_{max}} \tag{5.2.18}$$

A set of random numbers R are generated and for each collision pair a number R_i is assigned: the collision probability P_c is then compared to the random number.
If $P_c < R_i$ the molecules won't collide, otherwise post collisional velocities $c^*_{1,2}$ are calculated exploiting the conservation of momenta and energy.
In order to estimate the macroscopic quantities the sampling of the microscopic quantities is performed. For example, the average mass density ρ is expressed as:

$$\rho = \frac{\Sigma_{i=1}^{N_p} m_i}{V_{cell} N_t} \tag{5.2.19}$$

where m_i is the mass of the particle, N_p the molecules that occupy the cell and N_t is the number of iterations of the computation.
In conclusion, for neutral molecules the different choice of the model affect the value of the cross section and thus the corresponding probability of the collision.

5.2.3 Gas-Surface interaction

Up to now, we have considered only the interaction among molecules, but as the gas expands it also has to interact with the surrounding environment. In this specific work, the gas interacts with the walls of the vacuum chambers or with the other elements that inevitably bother its expansion like the skimmer or portion of the same valve from which the gas leaks. The question that one would like to reply is, can we model the gas-surface interaction?
To properly address this question, it is necessary to understand how to model the gas-surface interaction when the system is at equilibrium, accordingly non-equilibrium condition will be a generalization of the former configuration.
If one consider the single molecule being in equilibrium with a surface, two models can be considered:

- *Specular Reflection*: the velocity vector of the gas can be projected onto the perpendicular and parallel direction to the surface. The parallel component will remain unchanged, while the perpendicular one will be reversed. This condition correspond to have a perfectly elastic collision.

- *Diffuse Reflection*: the velocity vector of the gas after the interaction has no link with the initial velocity, but the velocity distribution occupies the half plane of the space. To make a comparison with light sources, such surface is *Lambertian*. This condition occurs when the gas and the surface have the same temperature. In other words, the molecule impinges on the surface and reaches the thermal equilibrium with it, evaporating from the surface itself following a Maxwellian velocity distribution

A comparison between the two extreme situations is reported in fig. 5.2.5.

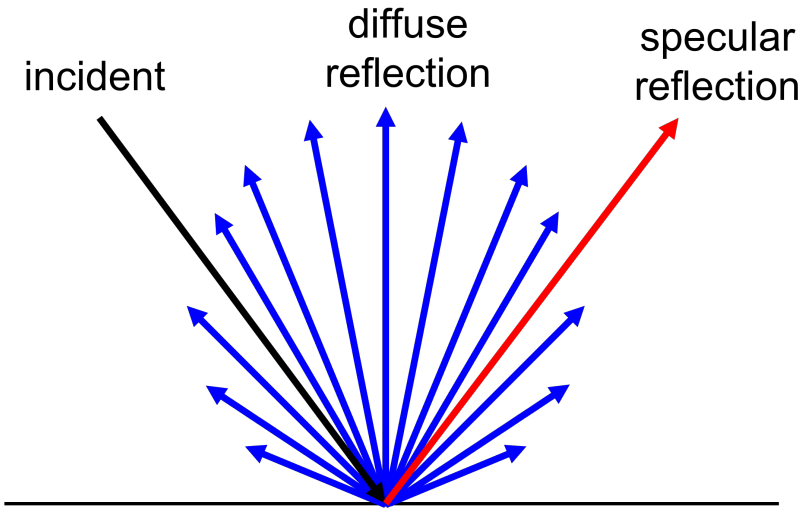

Figure 5.2.5: Scheme of the gas-surface interaction at equilibrium: comparison between *Specular* and *Diffuse* reflection

Though simple, both of these models are not accurately describing experimental gas-surface interaction, particularly when dealing with the interaction between gas and metal surfaces in high vacuum conditions. In fact, the molecular angular distribution is typically similar to a lobular shape [16]; for this reason the "accommodation coefficient"is introduced. It is usually defined as:

$$\alpha = \frac{E_i - E_r}{E_i - E_w} \tag{5.2.20}$$

where E represents the energy of the gas and the subscripts i identifies the *incident* energy, r the reflected one while w the energy of the molecule corresponding to complete diffuse scattering. This definition can be applied not only for the total energy but also for its normal and tangential components (obtaiing α_n and α_t respectively), as well as it can be extended also for the tangential and normal component of the momentum [37]. For the normal component:

$$\sigma_n = \frac{< n\vec{p} \mid \vec{v} \cdot \vec{n} >_i - < n\vec{p} \mid \vec{v} \cdot \vec{n} >_r}{< n\vec{p} \mid \vec{v} \cdot \vec{n} >_i - < n\vec{p} \mid \vec{v} \cdot \vec{n} >_w} \tag{5.2.21}$$

where n is the density of molecules, $\vec{p}$ is the momentum, $\vec{v}$ is the velocity, $\vec{n}$ is the normal to the surface and the average, identified by the bra-ket notation, is performed over the whole velocity space. The subscripts meaning is equivalent as before. Analogous expression can be retrieved for the the tangential component:

$$\sigma_t = \frac{< n\vec{p} \mid \vec{v} \cdot \vec{t} >_i - < n\vec{p} \mid \vec{v} \cdot \vec{t} >_r}{< n\vec{p} \mid \vec{v} \cdot \vec{t} >_i - < n\vec{p} \mid \vec{v} \cdot \vec{t} >_w} \tag{5.2.22}$$

where $\vec{t}$ represents the tangent to the surface. In this framework the Cercignani-Lampis-Lord (CLL) model exploits these concepts, assuming that the normal and tangential components of the momentum, σ_t and σ_n as uncoupled; furthermore, it treats the normal energy component α_n and the tangential momentum component σ_t as two independent parameters, while the other two parameters (α_t and σ_n depend on the combination). However, Bird proved that $\alpha_t = \sigma_t(2 - \sigma_t)$[3], hence in the DSMC software the two parameters that can be chosen are the normal and the tangential component of the energy accommodation coefficient, while the momentum components are directly fixed.
From the practical point of view, accommodation coefficients have been experimentally retrieved for various gas-surface interfaces at different temperature, speed and pressure conditions [3], such data will be used in the following.

[3]The proof of this formula needs the explanation of a heavy formalism in which the CLL model is build, which goes beyond the scope of this work.

5.2.4 DSMC - Boltzmann equation Relationship

As pointed out in section 5.2, the DSMC method is in close relationship with the Boltzmann equation, though their correspondence is not trivial and a further explanation should be performed.
The Boltzmann equation is a non linear integral-differential equation that describes the statistical distribution of particles under the assumptions of molecular chaos and instantaneous collisions among pairs of molecules. It can be derived using the tools of mechanical statistics, following the Liouville theorem. For a diluted gas with density n and velocity distribution function f (i.e., the probability that a particle in a certain position, at a certain time, has a given velocity), the Boltzmann equation is described as:

$$\frac{\partial(nf)}{\partial t} + \mathbf{c} \cdot \nabla_r(nf) + \boldsymbol{F} \cdot \frac{\partial(nf)}{\partial \boldsymbol{c}} = \int_{-\infty}^{+\infty} \int_0^{4\pi} n^2(f^* f_1^* - f f_1) c_r d\sigma d\Omega dc_1 \quad (5.2.23)$$

where $\mathbf{c}$ is the molecular velocity, $\boldsymbol{F}$ is an external force, c_r is the relative speed, while f and f_1 represents the distribution function of molecules with speed c and c_1, the sign, instead, represents the post-collisional values.
More in-depth, the term on the left hand-side of eq. 5.2.23 represents the evolution of the rate of nf in space and time, without taking into account any kind of collision: thus, the nf term would remain constant if $\boldsymbol{F} = \mathbf{0}$. This part of the Boltzmann equation is thus in direct contact with the first step of the DSMC procedure, though the difference is subtle: in the first case the density is related to the number of *physical molecules*, while in the DSMC procedure one has to rely on the concept of *simulated molecules* that represent on average a certain number of molecules.
The term on the right hand-side of eq. 5.2.23, instead, represents the binary collision between two molecules, where σ represents the total cross section of the event, that varies according to the adopted model. Regarding this last term, the main difference with respect to the DSMC method, relies on the fact that in the direct simulation the collisions are probabilistic and only those whose probability is sufficiently high are included.
In conclusion, DSMC cannot be simply seen as a solution of the Boltzmann equation, but rather a model of the gas flow that closely resemble the Boltzmann equation's terms and its assumptions.

5.3 Simulation Setup

In this section an overview on the parameters' selection and settings is shown, together with an estimation of the accuracy of the simulation.

5.3.1 Choice of the parameters

In order to start the simulation the main parameters to be chosen are reported in this section.

- The simulation geometry is defined: it is possible to choose between $2D$ space or $3D$ axially symmetry with parametric dimensions.
- For each space side, the boundary conditions must be indicated, such as "interface with vacuum", "interface with gas stream" or "periodic boundary condition" etc...
- The gas, or mixture of gasses, is defined, with attention on the model adopted for its collision.[4]
- The characteristics of the initial gas flow are pointed out: its number density, temperature and speed components.
- The surfaces that shape the gas flow are designed: their physical properties, which inevitably depend on the gas choice, are defined in this moment (e.g., their temperatures, the gas-surface interaction model etc...).

[4]Many gas properties are already printed out

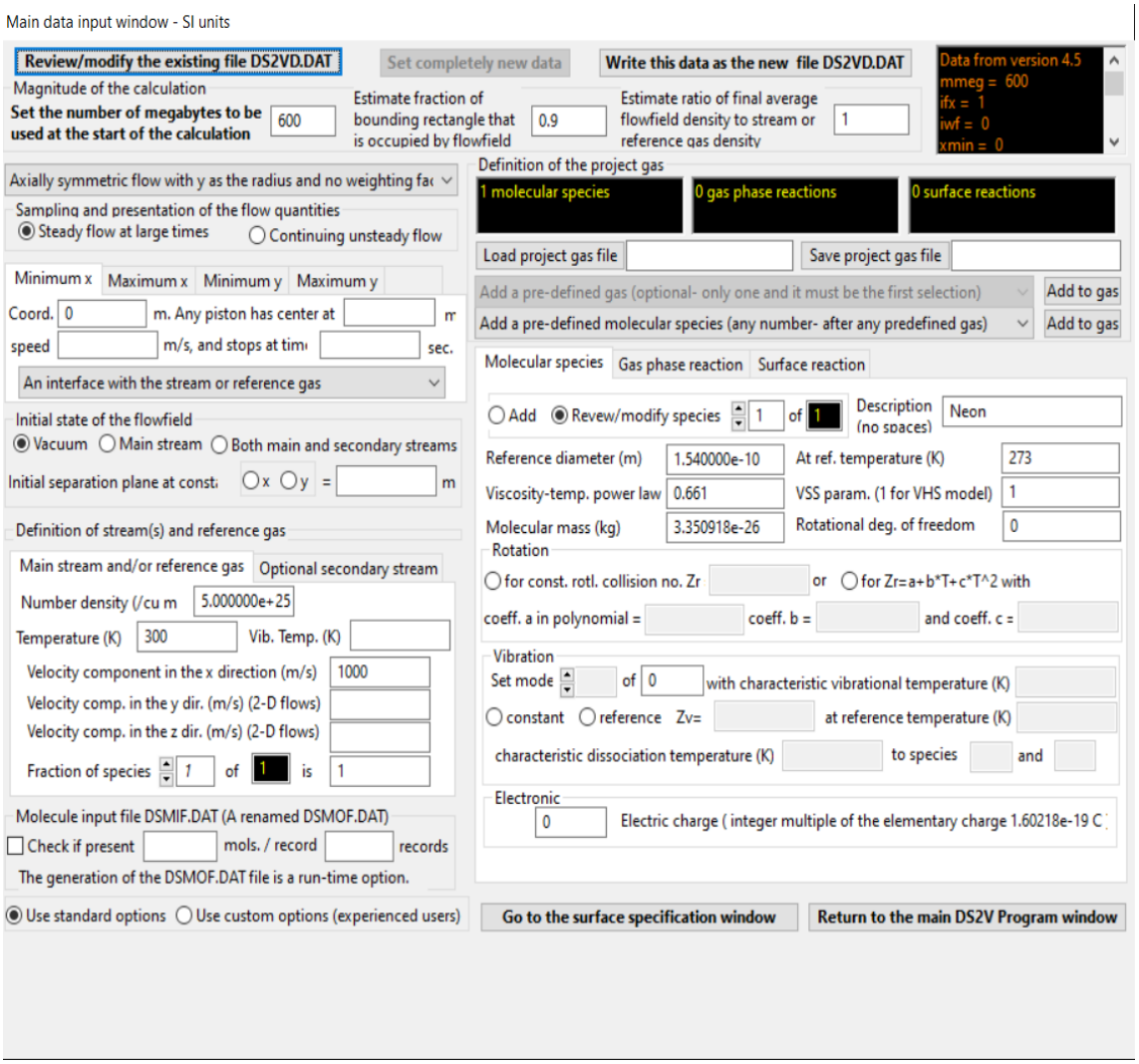

Figure 5.3.1: Main data input window of the DSMC software

At this point the simulation can start according to the above definitions.

5.3.2 Sources of error

After having analyzed the assumptions and the essential steps that characterize the DSMC method, a list of parameters to check to understand whether the simulation has been successfully performed or not is reported:

1. The cell size Δx is chosen: according to previous assumptions $\Delta x \approx \lambda/3$, where λ is the mean free path, this is required to prevent energy and momentum transport over large distances that would be unrealistic. Typically, this requirement is read as: the mean collision separation $(m.c.s)$ should be much smaller than the mean free path $(m.f.p)$ $(\frac{m.c.s}{m.f.p.} << 1)$

2. The time step Δt is defined: $\Delta t_{coll} \approx \Delta t_m/10$, in this way it is realistic to decouple the particles' movement and the collisions' computation.

3. The ratio between the number of *simulated particles* and *physical particles* is performed: in order to have a significant calculation the number of *simulated particles* should be in the order of 20 per cell.

While the simulation is going forward, all the spatial and temporal discretization assumptions are carefully checked at every iteration to understand if the output of the calculations are consistent with the physical constraints.

Chapter 6

DSMC Simulation

This chapter, dedicated to the application of the DSMC (version code 4.5.08) to our setup, is divided in two sections. The first part deals with the simulation of the gas jet properties at the output of the nozzle, without considering the skimmer interaction; in particular, both the spatial and temporal characteristics will be investigated varying the values of different parameters such as pressure, nozzle temperature etc... The second part, instead, considers the interaction with the skimmer and the variation of the gas properties due to its introduction: under suitable conditions the skimmer helps to achieve a well-confined beam, but it can give rise to unexpected complexities if it is not well aligned.
In both cases, only the carrier gas will be simulated due to its intrinsic simplicity compared to mixed species. The last section is dedicated to a short discussion of the behaviour of a mixture of a heavy molecules and a light gas.

6.1 Choice of the parameters

In order to start the simulation, the main parameters to be chosen are reported in this section. For standard conditions of pressure, gas type and temperature the main parameters that require a specification mainly rely on simple estimations. In particular each paragraph will deal with the estimation of a single parameter.

Input number density

In order to obtain a value of number density ($molecules/m^3$) at the input of the gas flow, the most simple hypothesis is to estimate it through the Perfect Gas Law. In particular for back-pressure of $P = 2bar = 2 \cdot 10^5 Pa$, at room temperature ($T = 300K$), the number of moles normalized to the volume is:

$$\frac{N}{V} = \frac{P}{RT} \tag{6.1.1}$$

where $R = 8.314 \frac{J}{molK}$ is the gas constant. For previous pressure values, the number of mol/m^3 is ≈ 80. In order to obtain the number of $molecules/m^3$, one needs to multiply for the Avogadro number $N_A = 6.022 mol^{-1}$, obtaining an estimation of

$$n = NN_A \approx 5.0 \cdot 10^{25} molecules/m^3$$

Velocity of the gas jet

For what concerns the estimation of the gas jet velocity, it requires a further analysis. In fact, it is not possible in the current situation to have an estimate relying on the formulae derived from fluid dynamics. Nevertheless, in prev sec. 4.1.2, for two different distances from the skimmer the gas jet expansion has been estimated as a function of the delay between the aperture time of the valve and the laser pulses. In particular, for a given distance between the skimmer and the valve, the delay τ is the difference between the time that a given pulse takes to reach the interaction region and the time that the gas needs to reach this point. If Δx_{laser} is the distance that the laser takes to arrive at a certain point in the vacuum chamber (which is fixed), and c is the speed of light, the first time can be written as

$$t_{laser} = \frac{\Delta x_{laser}}{c}$$

Instead the time that the gas takes to reach the interaction region can be defined as $\Delta x_{gas}/v_{gas} = \Delta x_{valve-skimmer}/v_{gas} + \Delta x_{skimmer-laser}/v_{gas}$, where the second part is fixed and the other can be varied. Hence the delay τ, for which the laser and gas pulses are synchronized is

$$\tau = t_{laser} - t_{gas} = \frac{\Delta x_{laser}}{c} - \frac{\Delta x_{gas}}{v_{gas}}$$

Hence, if two $\Delta x_{valve-skimmer}$ are chosen, two delays $\tau_{1,2}$ will be present that will depend only on the difference between $\Delta x_{valve-skimmer1,2}$. In mathematical terms,

$$v_{gas} = \frac{\Delta x_{gas,1} - \Delta x_{gas,2}}{\tau_1 - \tau_2} = \frac{\Delta X_{tot}}{\Delta \tau} \tag{6.1.2}$$

where, ΔX_{tot} is just the variation in the distance between the skimmer and the valve, since the $\Delta x_{skimmer-laser}$ is fixed. Following the conditions described above, and making the strong assumption of estimating only the central velocity of the gas jet, through the delay for which the gas jet presents its maximum, one can estimate v_{gas} as follow. For a distance between the valve and the skimmer $\Delta x_1 = 2mm$, the maximum $\tau_1 \approx 620\mu s$, while for a $\Delta x_2 = 12mm$, in the same other conditions, $\tau_2 \approx 570\mu s$, obtaining $v_{gas} \approx 100m/s$, as an order of magnitude.

Model adopted for the gas carrier

Since, only the carrier gas will be simulated, the gas modeling is well established. For a noble gas, the Hard Sphere model is adopted, while the viscosity-temperature law are listed as:

- Helium=0.657.
- Neon=0.661.
- Argon= 0.811.

Model adopted for the gas-surface interaction

Analogously, the values for the CLL model are listed, following the work done in [13], in which the coefficient increases as the molecule is heavier and matches the nozzle (or skimmer) material.

- Helium=0.4.
- Neon=0.8.
- Argon=1.

Geometry definitions

All the simulations are similar to each other in terms of geometry and symmetry. In fact, the geometry chosen is 3D axially symmetric with respect to the x axis. The radial coordinate will be defined as the y axis. Furthermore, the left side of the simulation perimeter is an interface with the gas stream, while all the other sides will be in contact with the vacuum making the approximation that the gas is carried out by the vacuum pump attached to the chambers. In the following the simulations, the most important figures are reported to clarify the geometry details (fig. 6.2.1, 6.3.1).

6.2 Simulation of the nozzle geometry

The first set of simulations that can be performed regards the exit of the gas from the nozzle (i.e., considering the oven's aperture shape). A 2D section of the full 3D geometry is reported in figure, 6.2.1. The gas will exit from the left hand side and will interact with the vacuum that is supposed to be on the right hand side of the nozzle.

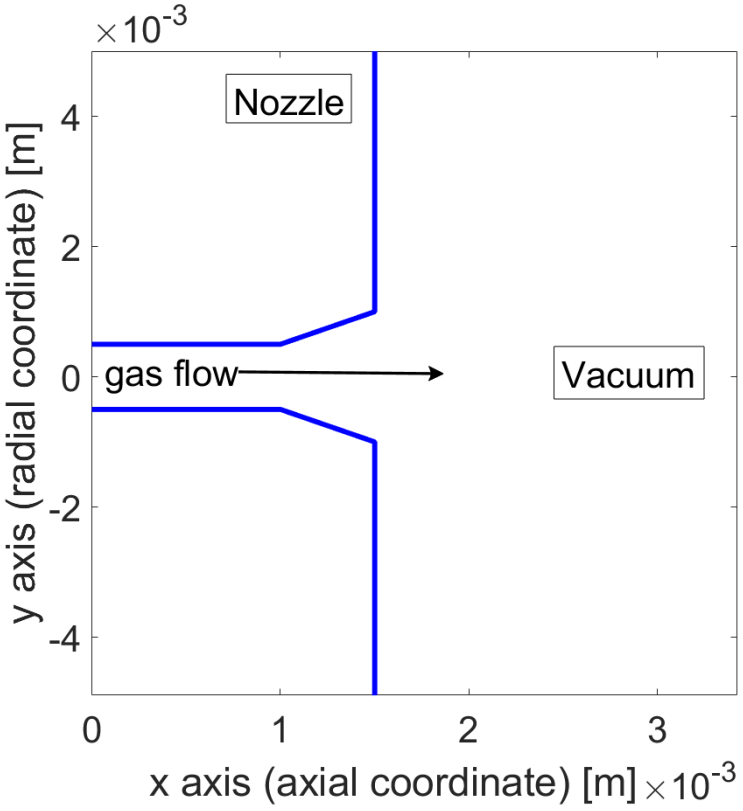

Figure 6.2.1: 2D section of the nozzle (blue line). The gas is flowing from left to right, where it expands in vacuum

It must be noticed, that the two axis are reported with different scale for graphical needs: in reality the shape of the nozzle appears to be much more spread in the radial coordinate.

6.2.1 Steady gas flow

First of all, I have performed a simulation using as parameters the standard working conditions of gas, pressure and temperature ($P_{input} = 2bar$ which corresponds to $10^{25} atoms/m^3$ as number density, $T = 300K$). In particular, the steady conditions are studied (the CW properties of the gas). In fig. 6.2.2, the number density is depicted in a 2D section and a logarithmic scale. In this condition, the flowfield is imposed to reach the steady conditions at large time.

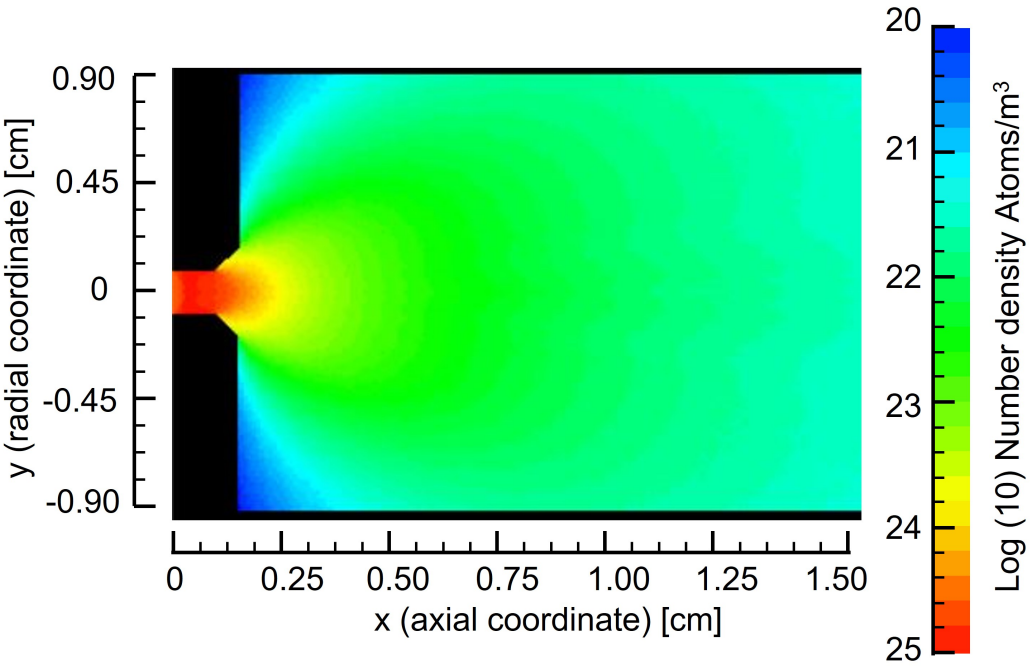

Figure 6.2.2: 2D section of the number density for Neon at 1 bar and 300 K at the exit of the oven aperture, after the Parker valve.

Qualitatively, the gas spatial shape appears to be very much spread and not confined at all in the radial coordinate. It is possible to affirm that we are not in presence of a supersonic gas-jet but rather we are dealing with an effusive and expanded beam. Furthermore, the decay is abrupt in the axial coordinate, as the color code legend helps identifying that after $1cm$ the number density has dropped from 26 to 23 $\frac{molecules}{m^3}$, corresponding to a pressure of hundreds of pascals.
It is possible to compare this first simulation with the one present to characterize the Even-Lavie valve (fig.6.2.3) [13].

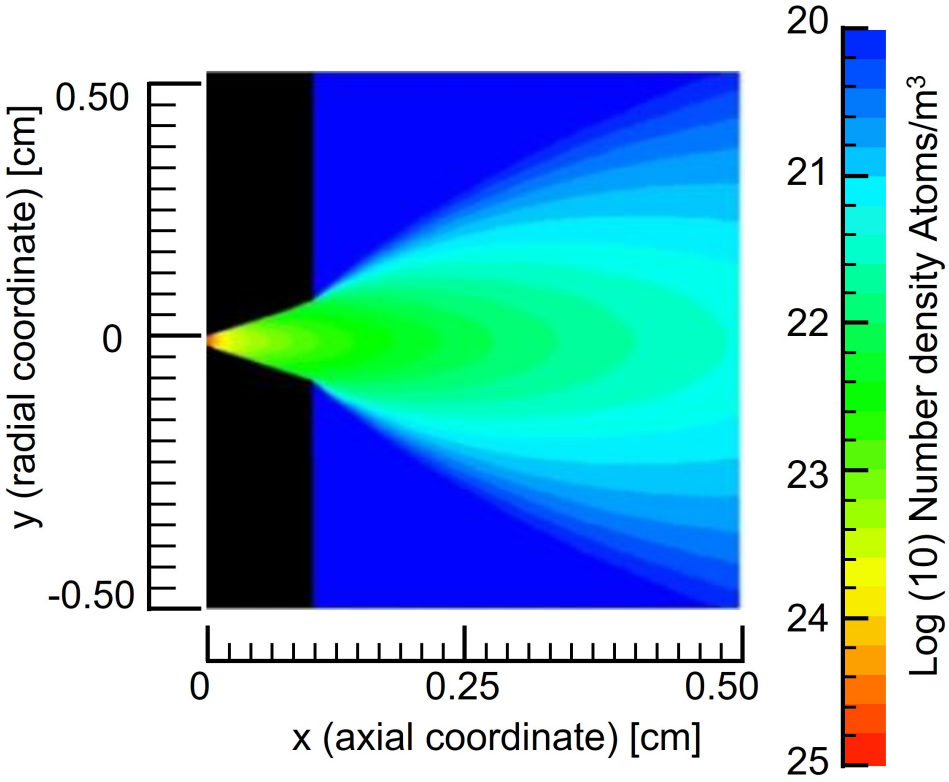

Figure 6.2.3: 2D section of the number density for Helium at 1 bar and 273 K of the Even-Lavie valve [13].

At a first glance, the radial expansions of the gas from these conical nozzles are way substantially different. In fact, the gas jet appears to be more confined with respect to the previous situation, even though the decay is comparable, if not greater, in the axial coordinate. This is probably due to the different shape of the nozzle. Even though they are both conical, the aperture at the exit hole appears to be substantially different. In fact, the Even valve presents a first channel of only $0.1mm$ of diameter and it opens up to $1mm$, instead the nozzle of the oven starts with a diameter of $1mm$ to reach only $2mm$. Hence, comparing these two values, it seems that the nozzle shape is imputable of the wrong gas-jet expansion.
Nevertheless, it can be studied if the change in pressure, the temperature of the nozzle, the gas species and other parameters can affect the spatial shape of the number density. In parallel, other relevant parameters to be studied are the velocity components of the molecules. In the next sub-sections all the different characteristics will be analyzed and discussed in details.

Dependence on the gas carrier

In order to understand if the gas species can affect the spatial shape of the gas flow, I have analyzed three carrier gases. In particular, since only light and noble gas are used experimentally, the simulations handle three gas species: Helium, Neon and Argon, where the parameters for the accommodation coefficients and the CLL model

are specified in sec. 6.1. In all cases the other parameters are fixed as in the standard conditions: even though it is true that the velocities of the gas will be modified by the gas mass, it can be assumed that as an order of magnitude the speed will not change much. This hypothesis will be analyzed in the next section when the aperture time of the valve will be simulated. In fig. 6.2.4 it is reported the decay of the beam density as a function of the axial coordinate.

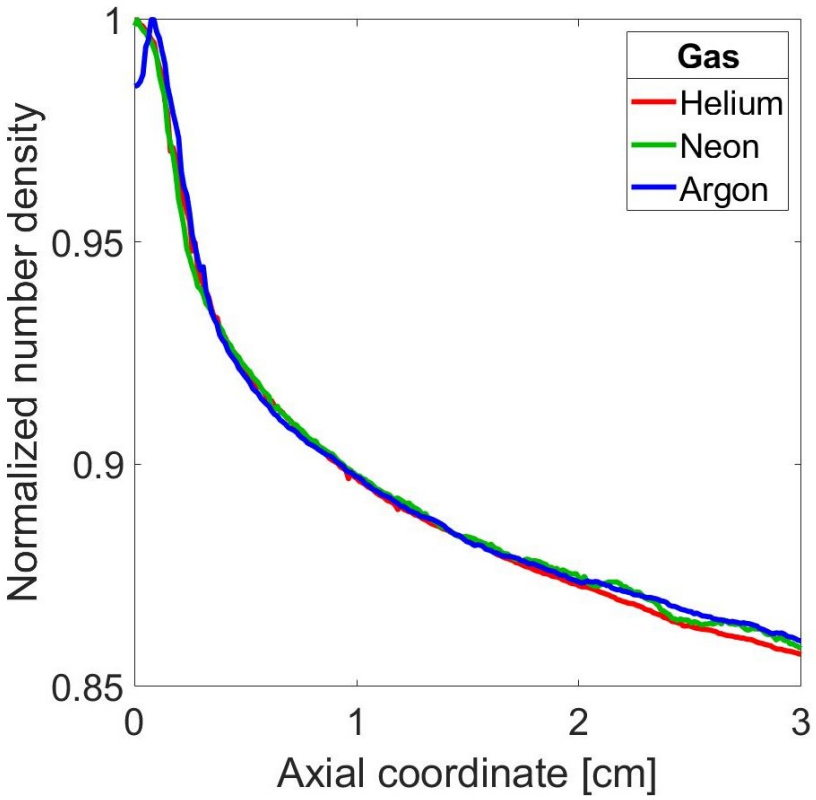

Figure 6.2.4: Normalized beam number density for different noble gasses (He, Ne, Ar) as a function of the axial coordinate (x), with input number density of $5 \cdot 10^{25} molecules/m^3$, initial speed of $100 m/s$, Temperature of $300 K$

It is clear that the decays are very similar in shape for all the three gases at large distance from the nozzle. The only difference that can be spotted regards the Argon case, where the decay is not monotonous as happens for Helium and Neon but shows a maximum after almost $1mm$. This can be related to the different accommodation coefficients which are very similar to Helium and Neon but slightly different for Argon. Furthermore, the CLL model accounts different coefficients for the three gases, as it increases if the mass of the gas matches the nozzle material. It has to be highlighted that only the shape of the gas decay has been studied: in order to do this, each number density curve has been normalized to the corresponding maximum value. For completeness, the 2D sections of the three simulations are reported in fig. 6.2.5: for $3cm$ distance in the axial coordinate: the radial expansion is almost the same in the three situations while small changes can be detected around the central part of the gas flow.

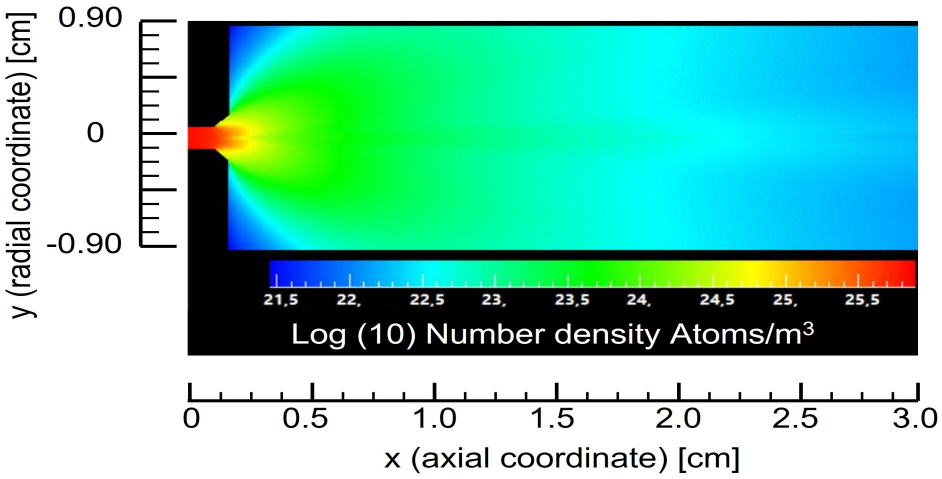

(a) Helium simulation

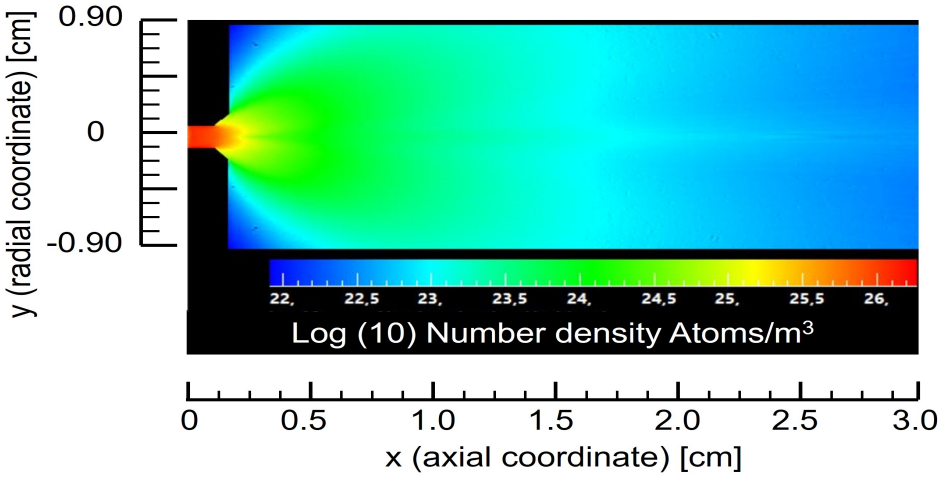

(b) Neon simulation

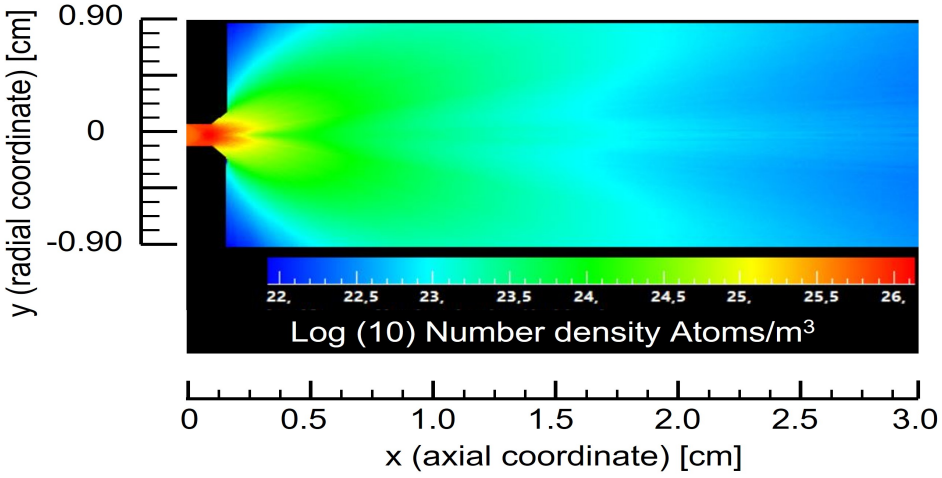

(c) Argon simulation

Figure 6.2.5: 2D number density section for Helium, Neon and Argon in standard conditions: input number density of $5 \cdot 10^{25} molecules/m^3$, initial speed of $100 m/s$, Temperature of $300 K$

It is thus clear that for distances larger than $1mm$ from the nozzle aperture it makes no difference to use as carrier gas Helium, Neon or Argon, at least from the spatial properties perspective.

Velocity distribution

At standard conditions, another parameter of interest is represented by the velocity distribution of the gas. One would like to have the central part of the gas flow to be sufficiently fast in order to carry the analyte in a confined cone that can be intercepted by the skimmer. At the same time, since the concentration of the gas is spread in a large solid angle, slower molecules will tend to sediment on the edges of the skimmer and the other components of the chamber. From the simulation point of view, two $2D$ sections of the simulations are reported in fig. 6.2.6. They both represent the same transverse section, hence the x axis represents the axial coordinate, while the y axis the radial coordinate. In the first image (fig. 6.2.6a),only the axial (x) component of the velocity vector is represented, following the legend shown below (i.e., blue represents velocity components equal to zero, while red represents the maximum velocity components). In the second image (fig.6.2.6b), only radial (y) component of the velocity vector is represented, with analogous consideration on the color code.

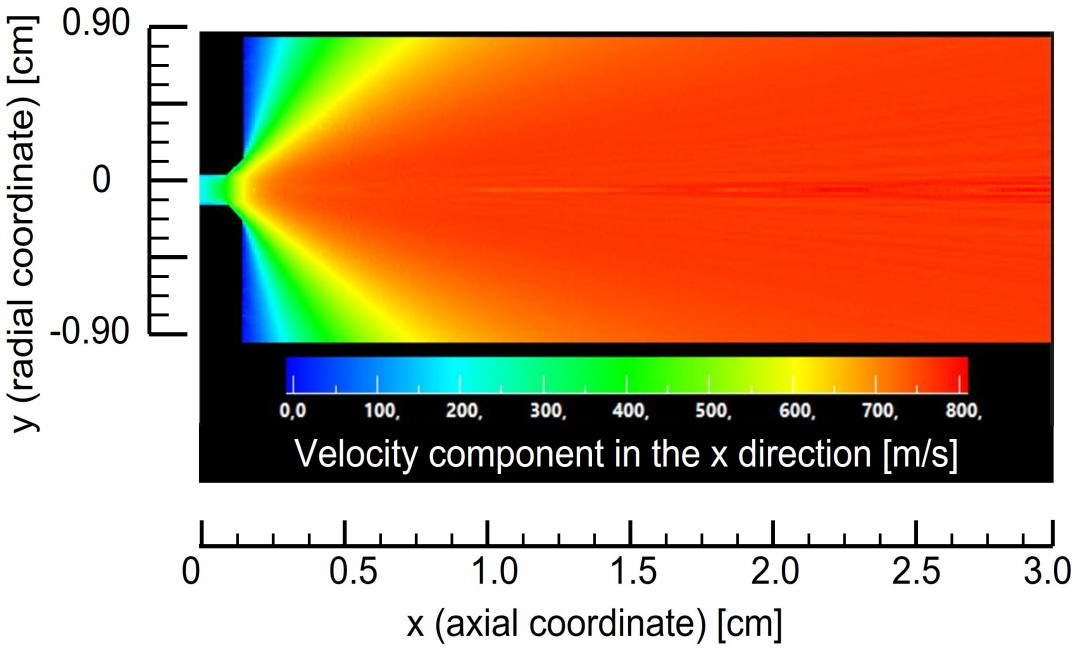

(a) Axial components of the gas velocity

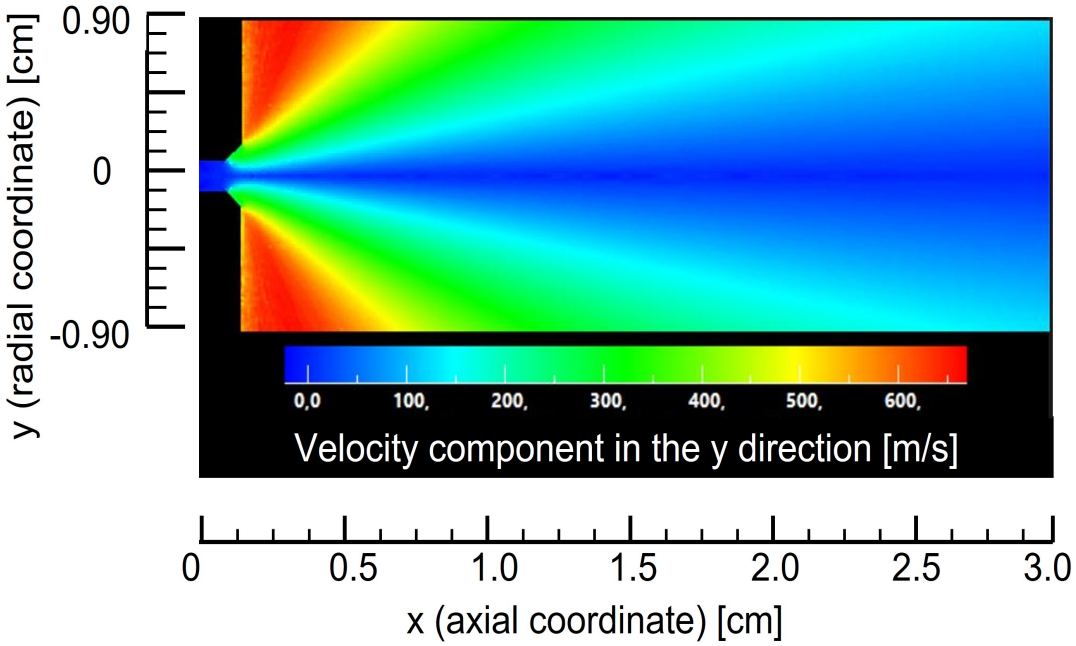

(b) Radial components of the gas velocity

Figure 6.2.6: 2D section of the nozzle, highlighting the axial (x) and radial (y) components of the gas velocity for Neon at standard conditions: input number density of $5 \cdot 10^{25} molecules/m^3$, initial speed of $100 m/s$, Temperature of $300 K$

In both cases the speed increases as the gas is moving away from the nozzle, due to the difference in pressure between the exit of the nozzle and the rest of the chamber that is assumed to be in vacuum. As expected, the molecules have a larger components along the axial coordinate while along the radial coordinate the fastest molecules are those close to the exit hole. This is consistent with the analysis of the number density done before.

Gas density distribution along the radial coordinate

From the numerical point of view it is interesting to understand the decay of the gas density in the radial direction. It is possible to notice that the decay is actually satisfying for very close distances from the nozzle (i.e., $0.1 mm$) but the spread, as one is able to move at larger distances, is extreme:

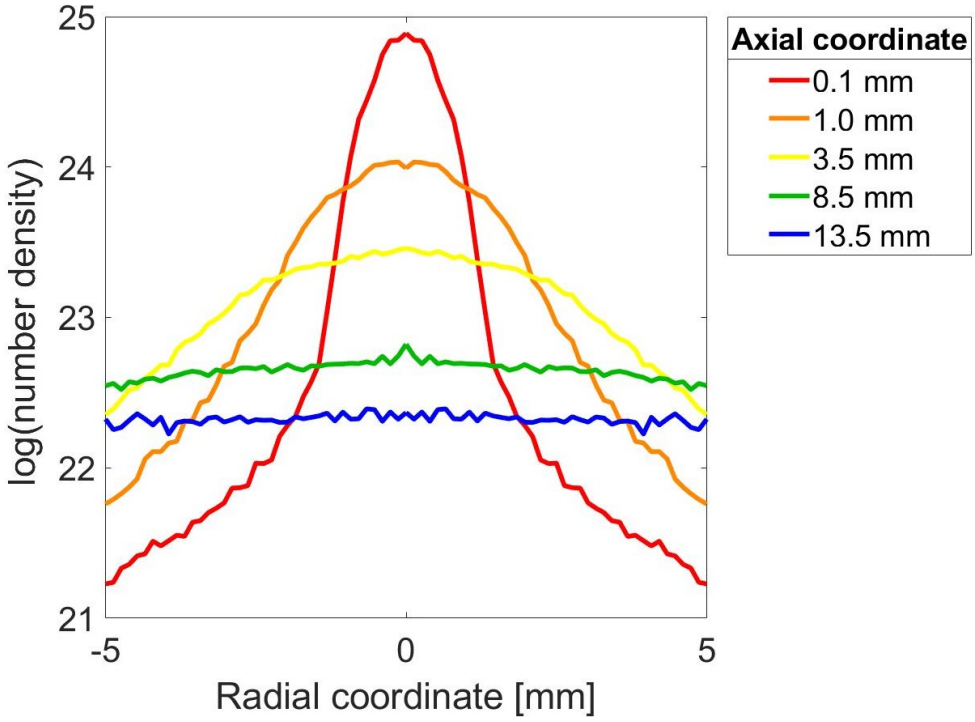

Figure 6.2.7: Number density (log-scale) as a function of the radial coordinate (y) for different distances from the nozzle aperture (starting from $0.1mm$ up to $13.5mm$), for Neon with an input number density of $10^{25} molecules/m^3$, initial speed of $100m/s$, Temperature of $300K$

This is a different situation with respect to the radial confinement experienced for the conical nozzle simulated by Even (fig. 6.2.3), for which the combination of a nozzle and a skimmer is welcomed.

Dependence on the back-pressure

In this section, I have studied the gas behaviour by varying the input pressure exiting from the nozzle. This parameter is related to the input number density: a large range of such values are analyzed. At room temperature, for $n = 10^{22}$ the corresponding pressure is just few pascals up to $n = 10^{26}$ which corresponds to almost 10 *bar* of pressure. In order to compare the different trends, the normalized number density, as a function of the axial coordinate, is plotted for all the input number density.

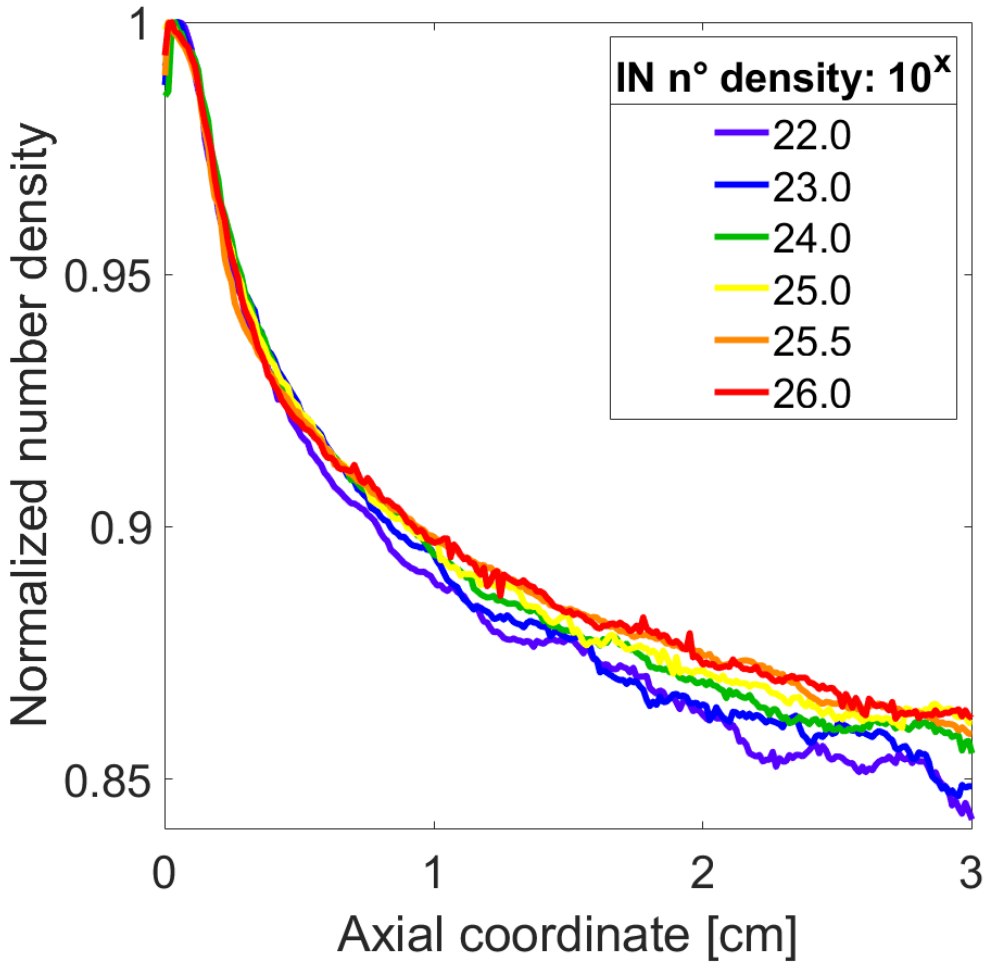

Figure 6.2.8: Number density (log-scale) as a function of the axial coordinate (x) for different input number density (starting from 10^{22} up to 10^{26}), using Neon at $300K$

The decay seems not to be affected by the input pressure for small distances ($< 0.5\ cm$), but it appears to be less decaying for larger pressures. However, it is difficult to link such behaviour to a physical interpretation even more when such differences appear to be modest. Hence, it can be stated that the change in pressure does not affect the spatial behaviour of the gas at the exit of the nozzle. Of course, larger gas pressure implies larger signals but the decay seems to be almost unaffected by the back pressure.

Variation of the nozzle temperature

The last parameter that I have varied in CW conditions is the temperature of the nozzle surface, since it can change according to the analyte that is needed to sublimate. In particular, while the gas is kept at room temperature, the nozzle can be heated-up to $500K$: for completeness, four different nozzle temperatures from 300 to $600K$ have been simulated.

The first analysis regards the axial distribution along the central part of the gas: it is clear from fig.6.2.9a that the central part of the gas flow is not affected by the temperature mismatch between the carrier and the nozzle.

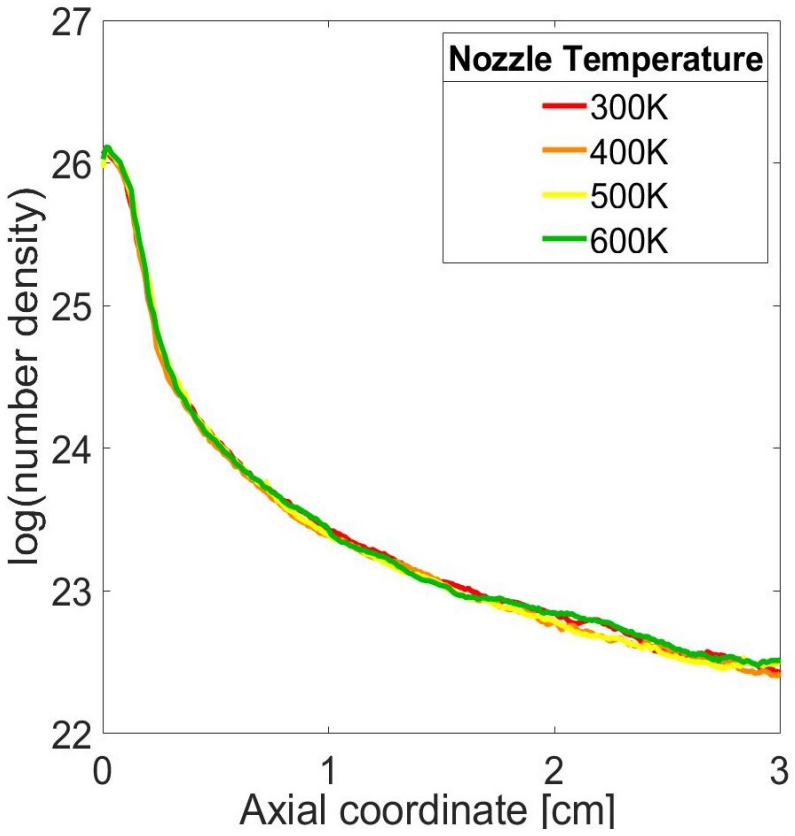

(a) Number density (log-scale) as a function of the axial coordinate (x) for different temperature of the nozzle surface (from $300K$ up to $600K$), using Neon at $300K$

A different condition is instead analyzed for the radial components of the number density, at a distance of $0.1mm$ in the axial coordinate, which shows a faster decay as the temperature mismatch is increased. However, this trend is not interesting since one is able to select only the central part of the gas flow, with a large skimmer up to $3mm$ of diameter can be taken. In both cases these simulations agree with what has been found experimentally: changes in the nozzle temperature do not affect the carrier gas flow. In particular, the DSMC software allow for exploring range of temperatures that were not tested experimentally, highlighting that there were not important variations.

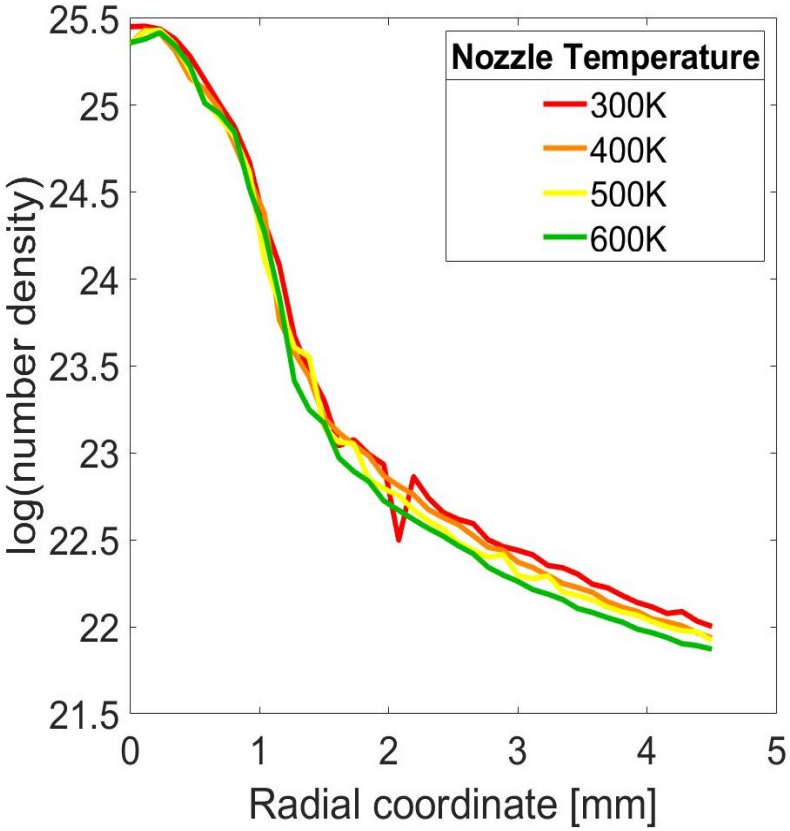

(b) Number density (log-scale) as a function of the radial coordinate (y) for different temperature of the nozzle surface (from $300K$ up to $600K$), using Neon at $300K$ at a distance of $0.1mm$ from the nozzle aperture

Figure 6.2.9: Number density (log-scale) as a function of the axial (x) and radial (y) coordinate for different nozzle temperature (from $300K$ up to $600K$), using Neon at $300K$

6.2.2 Unsteady gas flow (pulsed mode)

Up to now, only the spatial properties of the gas dynamics, in terms of number density or velocities components have been analyzed; nevertheless also the temporal properties of the nozzle need to be compared with what is expected from the experimental point of view. For this application, the "unsteady flow"parameter is set and an aperture time of $220\mu s$ has been selected, in order to match the requirements of the valve. In fact, this implementation is detrimental from the numerical perspective because the quantization error is more relevant and the results are far less precise than the steady condition, requiring also a larger computation time due to internal properties of the software. In particular, it is not possible to directly obtain the numerical results from the software and a post-processing extraction is needed. Furthermore, the images result to be more noisy than the steady conditions and the numerical values extracted fluctuate robustly. Thus an averaging has been performed to clean unwanted oscillations. In particular, considering an area with 9 pixels as side the results appear satisfactory without losing too fast variations. More particularly, I have implemented a MATLAB code to extract the data from the video, using dedicated image tools processing, averaging over a square of $9 pixels$, in the desired location. This code is reported in the appendix.

Temporal duration of the gas jet for different gas species

As done in the previous section, I have performed a comparison between three different noble gasses (He, Ne and Ar) but focusing on the temporal duration. For all the three cases an aperture time of $220\mu s$ has been set. The results are reported in the following figures.

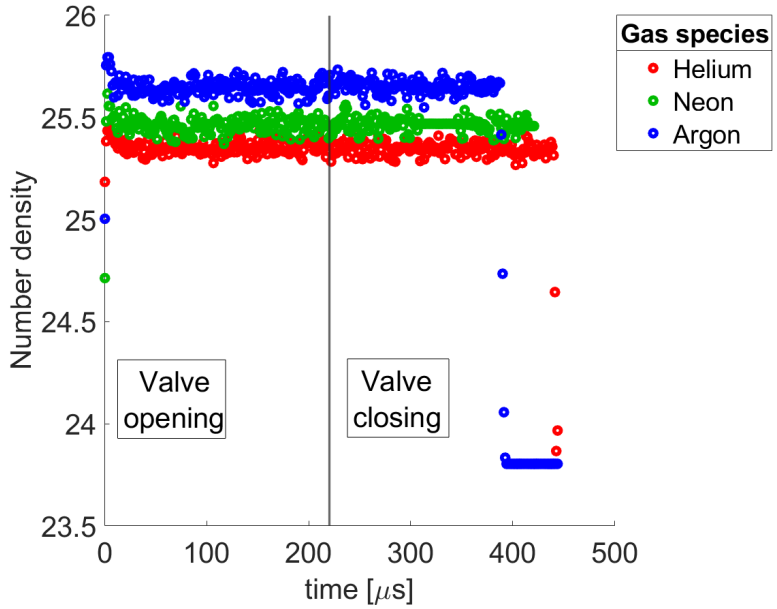

Figure 6.2.10: Temporal duration of the gas jet (He,Ne,Ar) at a distance of 1 mm from the exit of the nozzle, after the aperture of the valve at $t = 0$.

In all the three cases the duration of the gas flow is comparable, at this distance is around $400\mu s$: after a very sharp rise in time of few μs the flow is constant for all the duration of the aperture of the nozzle. In practice, there are no relevant differences in terms of temporal spread for the three species: although they have different masses, they share the same chemical properties and thus similar collision parameters. It is interesting to notice that the gas jet duration seems to decrease if the mass of the carrier gas increases, for the same values of pressure. This is actually counter intuitive, since one would expect that light gas would travel faster, causing less temporal spread. However, the difference in the temporal duration is of few tens of μs, hence would be imputable to be within the computational error.

Dependence on the back-pressure

As happens for the steady conditions, it is interesting to understand if different input pressures can affect the temporal duration of the gas jet. In order to simulate it, I have varied different number densities at the input. For simplicity, three number densities have been selected (log(n)=24, 25 and 26). All the curves shapes are exactly the same for what regards the rising edge, the constant flow and the sharp decay. Furthermore, the temporal duration is almost the same. On the contrary there is not a trend that associates the pressure with the duration, since the longest gas jet is represented by the middle value of exploited input number density. It seems that this characteristic is not affected by the value of back-pressure. Its variation can be imputable to the molecular speed which is probably affected by the difference in pressure ΔP between the channel and the expansion chamber. However, in these simulations this last parameter has not been varied due to the impossibility of predicting its value for different ΔP.

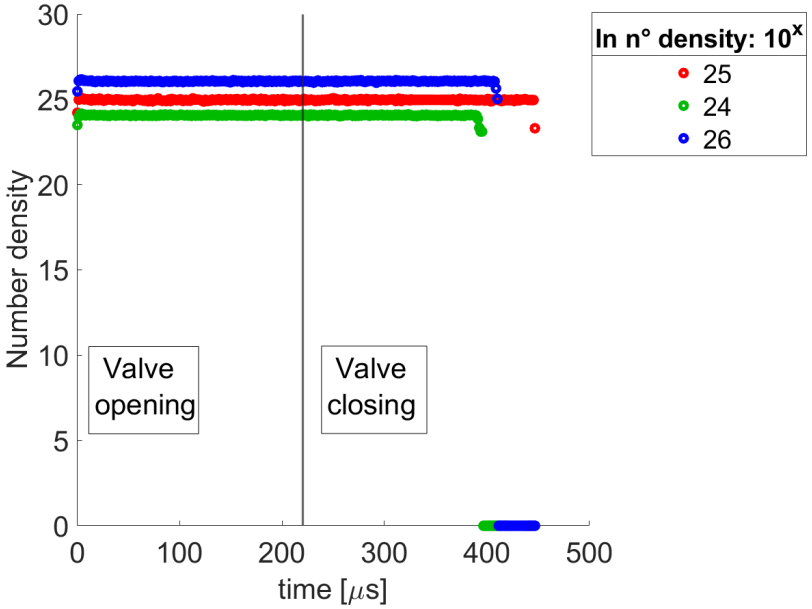

Figure 6.2.11: Time duration for different number densities $10^{24,25,26}$at a distance of 1 mm from the exit of the nozzle. The valve opens at $t = 0$

Comment on the unsteady condition

In this section, brief comments on the unsteady regime (or pulsed mode) are discussed. The comparison between the experiments and the simulations highlights that in both cases the beam is not well confined in time. At a distance of $\approx 4cm$ the experiments show that the beam has a $FWHM \approx 800\mu s$. An analogous analysis has been performed using the DSMC software. However, it is not possible to perform it at the same distances for computational reasons. At a distance of $1mm$, the temporal duration of the gas jet is about $400\mu s$, for back pressures ranging from $0.5bar$ to $2bar$. Yet, this duration would ensure to have a perfect match of the laser pulses with the gas jet, guaranteeing an ideal contrast of 1:0. However, being so close to the nozzle is impossible from a practical point of view. This difference can be imputable to different reasons:

- To reach larger distances the gas requires more time, for this reason the experimental values are bigger than the theoretical ones.
- In the experimental setup the gas jet is intercepted and partially blocked by the skimmer, in these simulations only the nozzle has been considered. The temporal dispersion should increase.

Experimentally, also different nozzle temperatures have been tested to understand if the gas jet duration would have been affected. However, since both in the CW simulations and in the experiments no particular differences have been highlighted for nozzle at room temperature or at higher ones (e.g., $200°C$), this configuration has not been explored in the pulsed mode. For what concerns the different gases, no comparison with the experiment can be performed. However, it is interesting to notice that the gas jet duration seems to decrease if the mass of the carrier gas increases, for the same values of pressure. This is actually counter intuitive, since one would expect that light gas would travel faster, causing less temporal spread. However, the difference in the temporal duration is of few tens of μs, hence would be imputable to be within the computational error. Analogous reasoning applies to the different input pressure, for which the maximum temporal duration is found for 10^{25} number density, the middle value of the explored range. Thus, it is not possible to derive any particular trend. These conclusions also highlight the limitation of these simulations in the unsteady regime and the subsequent poor data extraction.

Since no particular dependence on the temporal characteristics of the gas jet has been observed, in the following only the spatial properties of the gas jet will be analyzed.

6.3 Skimmer interference

Up to now, I have analyzed and discussed only the properties at the exit of the nozzle: however, before the interaction between the gas and the laser pulses a skimmer divides two parts of the vacuum chambers. Its presence may limit the intensities that can be obtained: its physical interpretation can be related to the interaction between the incident molecules and the reflected molecules by the skimmer surface that results in an increase in the random motion thus reducing the gas intensity [4]. The 2D section of the simulation space is represented in fig.6.3.1, where the nozzle is represented by the blue broken line, while the skimmer by the red one that is embodying the actual shape of the skimmer exploited in sec. 3.

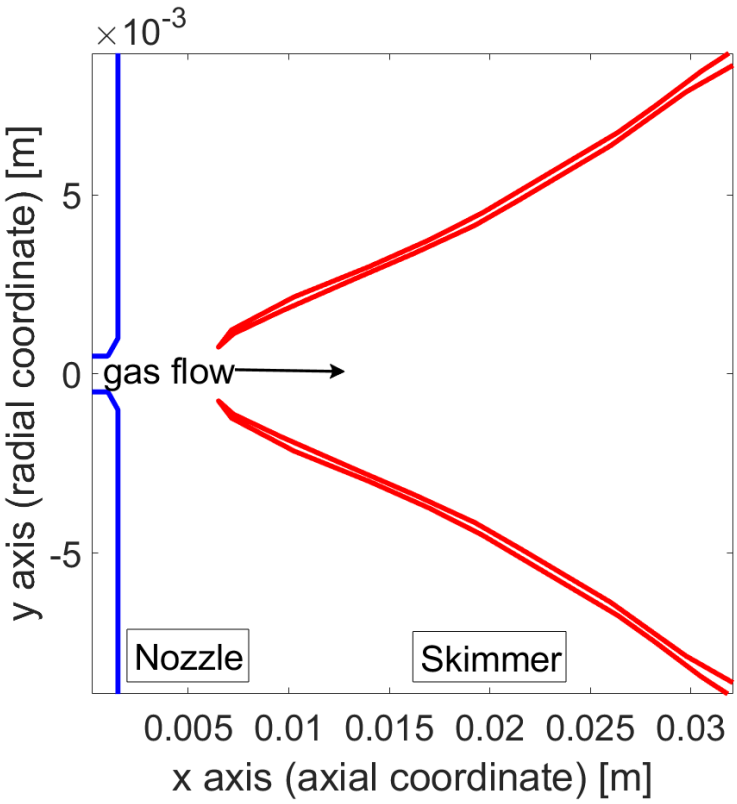

Figure 6.3.1: 2D section of the nozzle (blue curve) and skimmer (red curve) geometry, as it has been implemented for the DSMC simulations. The gas flows from left to right

First of all, one can study the properties of the gas jet for a fixed geometry (i.e., $2mm$ distance between the nozzle and the skimmer, $1.5mm$ of skimmer diameter and standard gas conditions) in comparison with the situation without the presence of the skimmer. What is interesting is actually understanding how the skimmer influences the decay of molecules along the axial coordinate (fig.6.3.2): in particular, it can be noticed that in the former situation the trend of the curve is constituted

by a sharp increase of the number density, followed by a slow decay. In the latter case there is no maximum but a monotonous decay toward a lower number densities is reported. This behaviour cannot be explained in easy terms however different conclusions can be drawn:

1. The two transmissions, with the skimmer and without it, are different. In fact, the skimmer partially blocks the impinging molecules: at the same distance, the density of molecules is lower of one order of magnitude with respect to the case of a simple expansion from the nozzle (i.e., one has to consider that the y-axis in the plot is in the logarithmic scale).

2. The difference at $x = 0$ in the two densities could be ascribable to the gas flow adaptation. These simulations do not show a particular time instant, but represent the gas after a theoretical infinite time. It means that, starting with the same input pressure (which corresponds to an input number density) in the two cases, the gas tends to adapt in different ways.

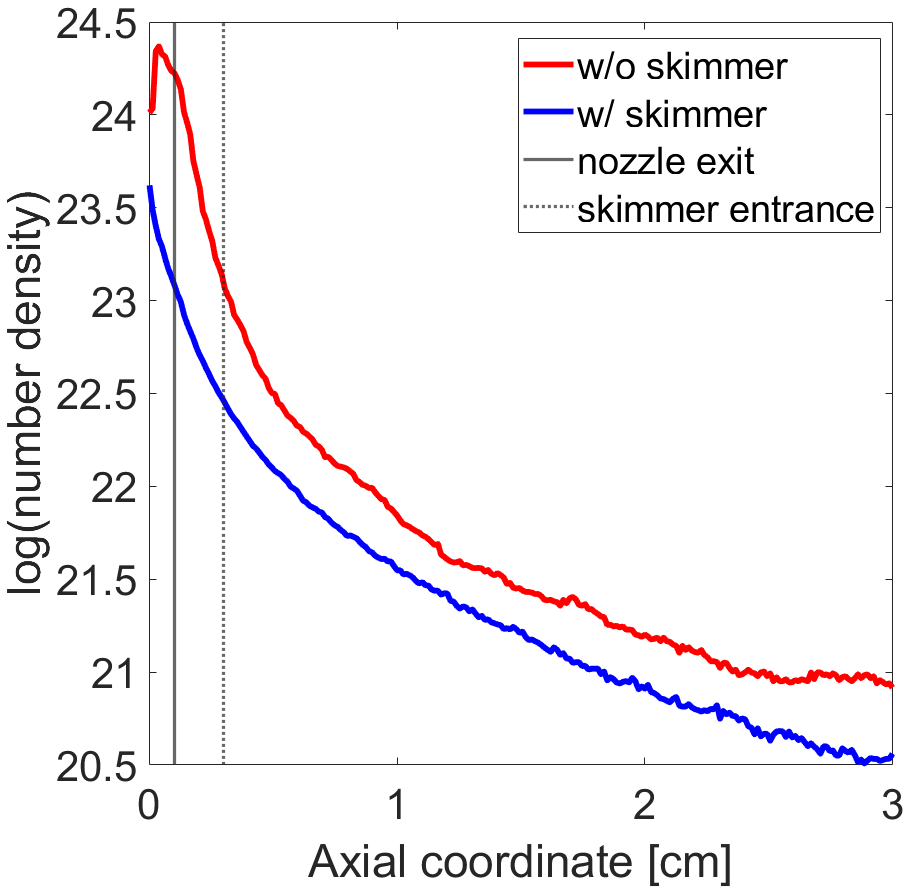

Figure 6.3.2: Number density (log scale) as a function of the axial coordinate (x) for two cases: the red curve represents the trend without the skimmer, the blue one takes into account the skimmer interference.

Another interesting characteristic is represented by the study of the Mach number (i.e, the velocity component normalized to the input velocity) along the axial and radial coordinates.

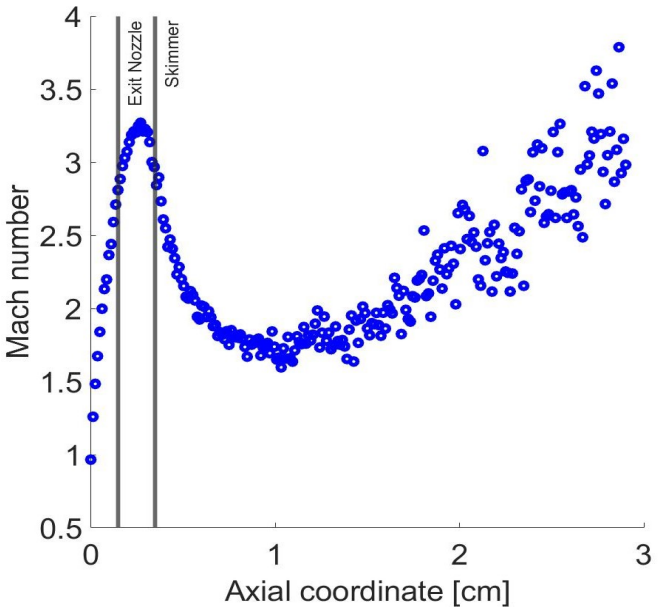

(a) Mach number function of the axial coordinate (x)

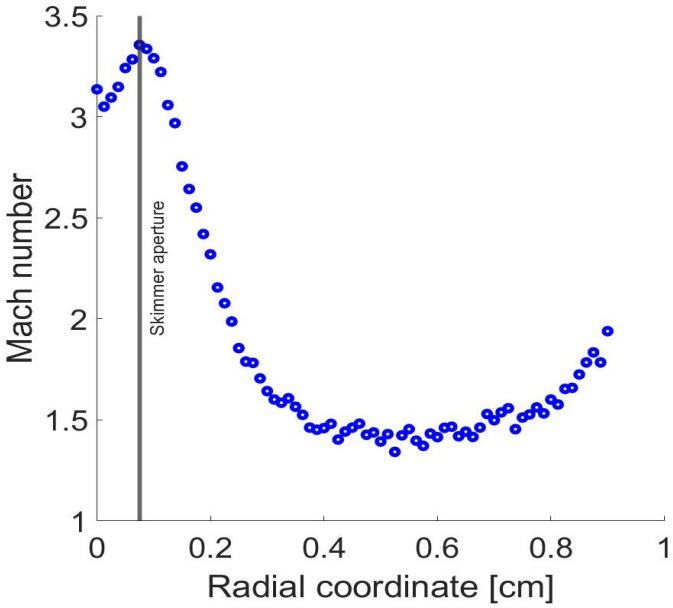

(b) Mach number function of the radial coordinate (y) at a distance of $1mm$ from the exit of the nozzle

Figure 6.3.3: Mach number behaviour along the axial (x) and radial (y) coordinate for Neon at $300K$, with an input number density of 10^{25}.

Both of these curves are consistent with the fact that the skimmer interference causes a detrimental interaction between reflected and incoming molecules: in the axial coordinate at the exit of the nozzle the molecules are further accelerated but before the skimmer entrance a maximum is reached due to the above mentioned interactions. The skimmer causes an abrupt decay of the velocities right after its entrance, only after $0.7mm$ the molecules are accelerated due to the difference in pressure between the chambers, since the last one has been modeled as the vacuum. Analogously, the skimmer shapes the velocity map in the radial coordinate, whose curves has been retrieved at an axial coordinate corresponding to right before the skimmer entrance, hence at almost $2mm$ from the nozzle aperture: the molecules are slowed down even more than before. This effect is particularly important not just for the carrier but for the molecules that the carrier gas transports: if they are slowed down too much, they can settle on the skimmer surfaces causing its clogging in reasonable time. Furthermore, this effect can be attributed to the skimmer interference because one would expect that the decay should be monotonous. In fact, if the gas is well spatially confined few molecules will escape along the radial coordinate and they will be just moving free at almost constant speed. However, the speed of the molecules is much attenuated: their interactions are stronger when approaching to the skimmer. Then, they are accelerated towards the vacuum both due to the difference in pressure and to a greater extent to the decrease number of collisions.

Dependence on the nozzle-skimmer distance

Since these simulations require a very high computational time (with a standard computer [1] even more than two full days) only few conditions can be explored in detail. One of the most important parameters that I have studied experimentally is the variation between the nozzle and skimmer distance.
In order to have a summarized vision, the skimmer transmission has been calculated for different skimmer-nozzle distances. This parameter has been calculated as

$$T = \frac{< n_{output} >}{n_{input}} \tag{6.3.1}$$

where n is the number density along the axial coordinate and the value at the numerator has been averages over few values to have a more stable result, trying to reducing the numerical errors.

[1] CPU: Intel(R) Core(TM) i5-9300H CPU @ 2.40GHz; RAM: 8,00 GB

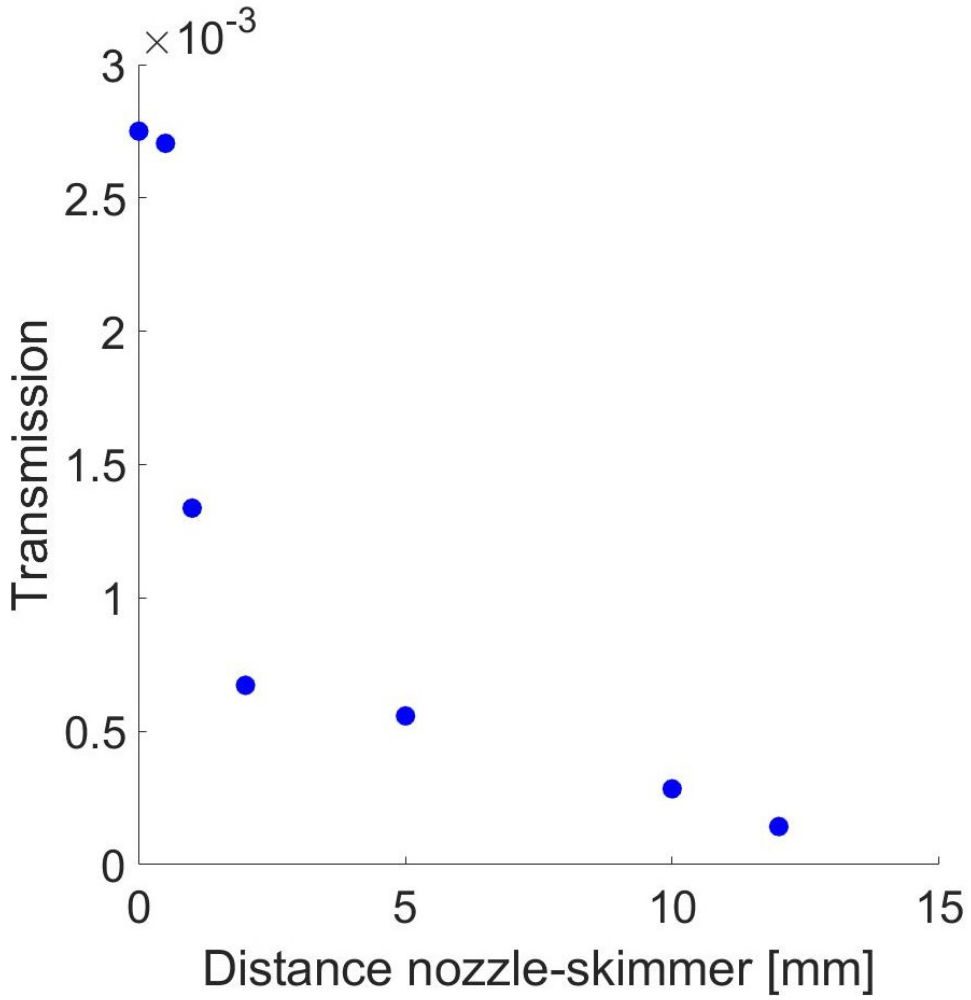

Figure 6.3.4: Skimmer transmission (eqn. 6.3.1) for different nozzle-skimmer distance (x-axis) for an input number density of 10^{24}

As one would have expected, the transmission is maximum for small distances and decreases as the distance is increased. Furthermore, for small values the transmission is not affected too much (i.e., between 0 and $0.5mm$, the results are comparable), it then follows a sharp decrease where a plateau region between 2 and $10mm$ is reached, while it continues its decline for large distances.
The transmission as a function of the nozzle-skimmer distance is consistent with the amplitude trend shown in 4.1.7 and 4.1.8: experimentally by increasing the distance between the valve and the skimmer, a sharp decrease of the transmission (and thus of the gas amplitude at the read-out card) is obtained for values of distances between 2 and $10mm$, while a slower decay is obtained for larger distances. Analogously, the sharp decrease is present in the data coming from the simulation but only up to $2mm$, while a sort of plateau region is shown after $5mm$. However, they both show a decreasing trend by increasing this parameter.

It would appear that no improvements are obtained if the skimmer is placed "far" from the nozzle, but actually it depends on the aim one wants to reach. While at the output the density of molecules decreases, the spatial properties along the radial coordinate are shaped by such distance which is a critical parameter.

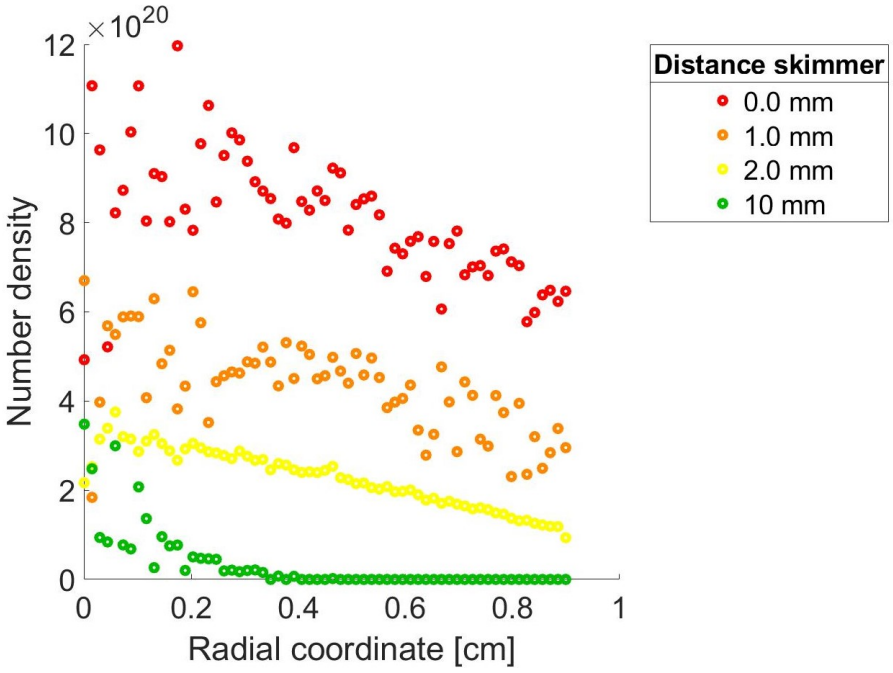

Figure 6.3.5: Number density as a function of the radial coordinate (y) at the output of the skimmer, for different nozzle-skimmer distances (ranging from 0 up to $10mm$)

In particular, the maximum signal is obtained for the closest distances but it appears to be almost flat and constant for a wide range. On the other hand, by increasing the nozzle-skimmer distance the signal is decreased more and more but the skimmer tends to intercept only a central part of the gas flow. For $10mm$ of distance, the radial expansion of the gas at the output of the skimmer is cut down after just $3mm$: this result is surprising and highlights the trade-off between the satisfying spatial beam shape and a proper signal. Increasing the distance between the nozzle and the skimmer is detrimental for the output intensity, but it is beneficial for the gas spatial confinement, reducing the radial expansion.
This plot can be compared to the experimental measurements performed for the spatial spread of the gas jet. In the experiment, by moving the laser pulses with respect to the entire structure (nozzle and skimmer) of $3.5mm$ only very small changes in the ion yield were detected. Unfortunately, it is not possible to explore further distances because of alignment issues. Hence, the gas has a radius of at least $3.5mm$. This plot also confirms that the decay in the radial coordinate is extremely slow. Even at the largest nozzle-skimmer distance, for which corresponds the most shrink gas jet, the radial expansion is about $3mm$, which is comparable to the previous experimental value.

Dependence on the input pressure

As it has been studied for the nozzle alone, I have studied different input pressure values to understand if the transmission presents different features. Due to its extreme long computational time, only two input pressures have been studied, corresponding to input number density of 10^{24} and 10^{25} $molecules/m^3$, since this is in the order of the real working pressure.

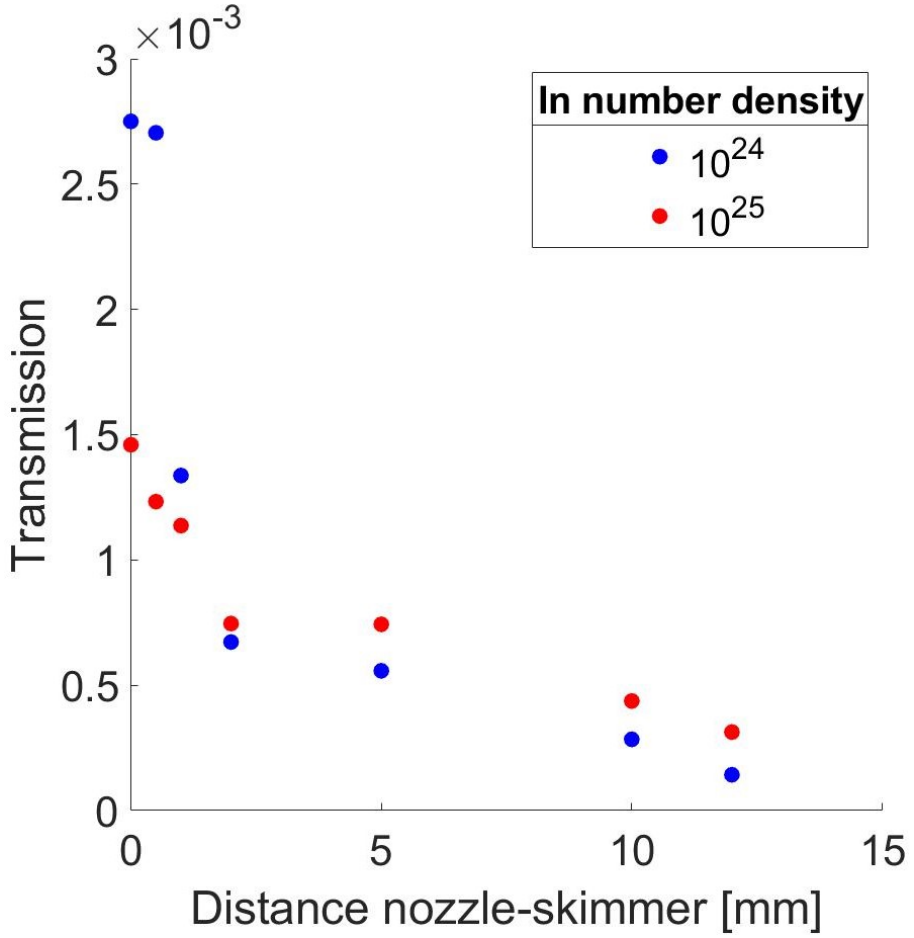

Figure 6.3.6: Comparison between skimmer transmission (eqn. 6.3.1) as a function of different nozzle-skimmer distances (ranging from 0 up to $12mm$), for input number density of 10^{24} and 10^{25}

For distances larger than $2mm$ the shapes of the transmission curves are almost the same even though for $10^{25} molecules/m^3$ input number density, the transmission is larger than in the previous case. This trend is inverted for distances lower than $1mm$, where the transmission is lower for the second case and the shape of the curve is slightly different. Nevertheless, the decrease at larger distances is evident and meaningful. Trying to give a physical interpretation to this phenomenon is one of the most difficult tasks, since it should link the gas flow at the output of the nozzle with the skimmer interference.According to literature it is found that the increase between the nozzle-skimmer distance does not imply a decrease in the transmission,

but rather passes through a maximum and only finally decreases [34]. This could be the explanation that with the current geometry we are not dealing with a supersonic gas-jet but rather with an effusive beam that is interacting with a blocking system that is not acting as a skimmer. Analogous consideration, as it has been done for fig. 6.3.4, can be extended for the comparison of the experimental trend.

6.4 Other geometries

I have proved that the skimmer should be placed further from the nozzle in order to achieve a confined beam in the radial coordinate, but the drop in intensity would be too detrimental probably due to the shape of the skimmer that is built for supersonic well-confined gas jet. In order to understand whether other geometries would help in achieving a confined beam, one could think applying the nozzle geometry identified by Even to the current setup [13]. In particular, the former shape presents an input hole of $0.1mm$ and an output hole of almost $0.9mm$. In this condition, considering an aperture of $1mm$, which is fixed in our setup, the exit aperture would be almost $1cm$: this is naturally unfeasible because it would imply a massive gas flow for such small vacuum chambers.
Instead, I have studied the condition of a fixed nozzle structure and a different shaping surface. In particular, to avoid a severe intensity drop, a simple aperture, consisting of a hole with a diameter of $4mm$ is studied. The increase in the diameter would help getting a larger transmission that, together with the changed shape, could help in preventing its clogging. For similarities, the collimator replaces the skimmer in its position where the transmission is still sufficiently high but not too much, in order to prevent damage if applied to the real experimental setup which presents the constraints on the vacuum chambers pump.
The decay along the axial coordinate is analogous to the corresponding situation and for this reason the plot is not reported. The transmission is in the order of $5 \cdot 10^{-4}$, in line with previous simulations with the skimmer with an entrance hole of $2mm$ at $2mm$ distance. What is interesting to study is actually the radial expansion of the gas before and after the collimator.

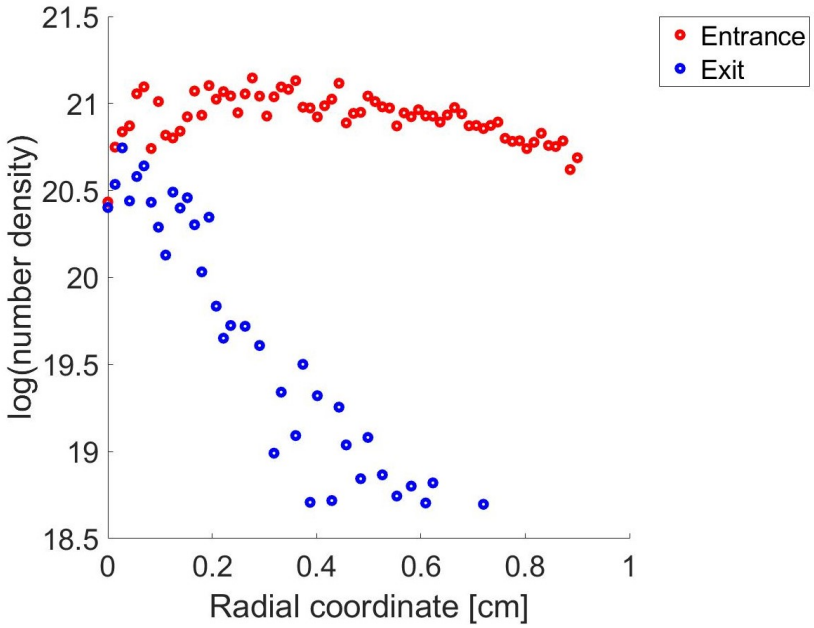

Figure 6.4.1: Radial behaviour of the log(number density) before and after the exit collimator with diameter of $4mm$

The confinement along the radial coordinate after the exit hole is surprising. One is able to obtain a spatial confinement of the beam maintaining a sufficiently high density of gas at the output. However, the problem is the deposition of molecules upon the collimator: the radial expansion of the gas before the exit hole is dominant and if the gas is light, as happens for the carrier gas, there would be no issues since it will be pumped out by the vacuum pumps; the problem arises when a heavy molecule is transported by the carrier gas due to the possibility of deposition along its surfaces and the subsequent clogging of the aperture hole.

6.5 Discussion on mixed gasses

Up to now, I have studied in detail only the carrier gas both in its time and spatial domains. The simulation regarding larger gas molecules, that will be the actual analyte of the experiment, is almost impossible to perform: for large molecules (like phenylalanine) there are not models that can represent them in a proper way, apart from considering them as large spheres, but this will be a too strong approximation inasmuch accommodation or CLL coefficients are not present in literature and there is no way to predict them. Moreover, the computational effort will increase more leading to unsatisfactory results. However, there are studies [34], that deal with the combination of light and heavy gas flow for which the light gas will have a larger transverse velocity component due to the collision with the heavy gas, diffusing out of the core of the beam. On the contrary, the heavy species will not be affected by the interaction of the light one and thus the gas properties can be traced back to the heavy species.

6.6 Conclusions

In this section I have analyzed the behaviour of the gas properties at the output of the nozzle and its interaction with the skimmer.
From all the simulations it appears that the nozzle design is wrong and it is not able, under any input pressure or temperature condition, to provide a supersonic gasjet. The simulations highlight that the gas flow is not completely effusive as a pinhole aperture would offer neither a well-confined beam as a real supersonic nozzle would supply. Rather it is a middle way toward the effusive and the supersonic regime. The temporal properties of the gas flow do not show anything interesting, this is probably due to the low resolution of the videos in the unsteady regime and the subsequent poor data that can be extracted.
Then, the skimmer interference has been analyzed: while the transmission is rather low for all the distances, it is interesting to notice that the spatial confinement can be achieved in the radial axis for nozzle-skimmer distances larger than $12mm$, however it is difficult to explore further geometries due to computational limits of these simulations. What appears clear, is that, rather than inspecting complex skimmer geometries and arrangements, the problem is earlier in the process and it is represented by the nozzle shape that is not able to provide any kind of exploitable conditions. For this reason, the skimmer, shaped to extract a supersonic gasjet and provide a differential pressure between two chambers, only mitigates the incoming gas flow without any tangible advantages.
The last simulation takes into account a collimator that replaces the skimmer in a similar position. The output gas properties are satisfactory but from an experimental point of view, its use might be limited by the deposition of molecules in its aperture. Nevertheless, in order to prove it an experimental measure should be carried out.

Chapter 7

Pump-Probe experimental proof

Based on the previous simulations and experimental proofs, the current geometry is not satisfying neither for the spatial nor for the temporal properties of the gas flow which cannot be consider as a gas jet but rather an effusive beam. It is thus useless the employment of a skimmer, at least from a fluid dynamics perspective, since no central core of the gas jet needs to be selected. The skimmer is only useful for an experimental point of view in order to prevent both the overload of the vacuum pump close to the MCP detector that needs to ensure a pressure lower than 10^{-6} $mbar$, thus maintaining a differential pressure between two chambers, and also to prevent the deposition of the analyte onto the electric lenses. Hence, the skimmer cannot be simply removed but a trade-off exists for its aperture diameter: if the diameter is too small the signal would be too low, but increasing its dimension would inevitably increase the powder deposition on the vacuum chambers surfaces and objects.
In the previous simulations, a collimator of diameter of $4mm$ has been analyzed, hence in this chapter the skimmer will be replaced by such structure that will be experimentally tested.
In particular, the dynamics of phenylalanine will be studied and compared to a previous work [9].

7.1 Experimental results

The exploited setup has been analyzed in sec. 3. In this chapter only the relevant characteristics are highlighted. In particular, as probe pulse, an IR pulse, with transform limited duration of $4.51fs$ and energy of $0.54mJ$ has been used, which is also exploited to generate, in Krypton, the XUV train pulses that are used as pump pulses. Both the spectrum of the IR, that is similar to that used by Calegari et. al [9], and the XUV spectrum are displayed in the following figures.

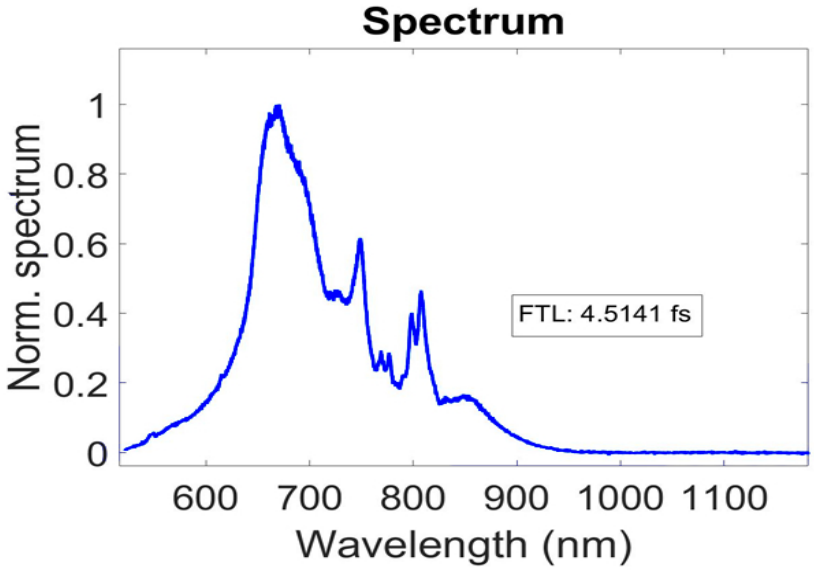

(a) IR (probe) spectrum acquired after the Hollow core fiber

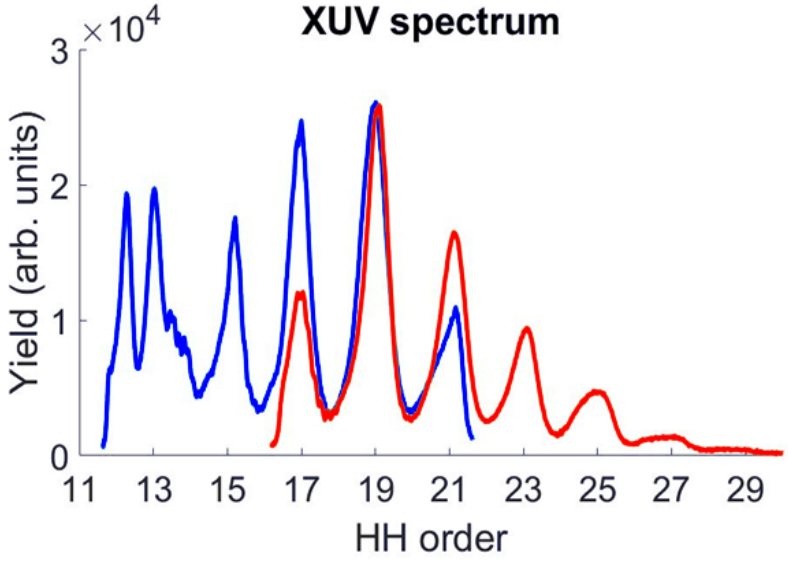

(b) XUV (pump) spectrum, generated in Krypton (at a pressure of $2.2 \cdot 10^{-3}mbar$)

Figure 7.1.1: Pump-probe spectra acquired for 30 seconds

In this experiment, Helium has been used as carrier gas, maintaining a back-pressure of $2bar$. In particular, due to the impossibility of obtaining a spatial and temporal confined gas jet, the effusive flow has been exploited in continuous regime. In this pump-probe experiment, the probe is delayed with respect to the pump. In order to wash out the noise, for every pump-probe delay, a single shot of the ion yield is acquired: first it is recorded the ion yield due the pump only (which represents the background) and then the ion yield due to the pump followed by the probe pulse (which represents the signal one wants to explore superimposed to the background). Hence, every delay is explored at every laser shot and the whole set of measurement is repeated for 11 times.
The oven has been heated up to 90° and for values of $2.29kV$ of MCP. Furthermore, the lens and drift electrode are kept at $2kV$, the repeller and extraction lenses at $155V$. In these conditions, the signal of the parent ion was in the order of few mV. To obtain a single point at a fixed delay, the area under the curve of the particular ion is calculated and then averaged among all the acquisitions. Briefly, only the dynamics of the immonium doubly charged ($m/q = 60$) will be shown, which is the one studied in sec. 1.1.2, that have been normalized with respect to the XUV only signal. In particular, the formula for the relative ion yield is:

$$\eta = \frac{< Area_{XUV+IR} > - < Area_{XUV} >}{< Area_{XUV} >} \tag{7.1.1}$$

where the $< ... >$ represents the average value and the Area stands for the area under the curve of the particular ion of interest. In fig. 7.1.2, only the long dynamics can be spotted: for negative delays the immonium doubly charged is not formed but a rise is present when the pump and probe pulses interact together with the sample. For larger positive delays a decrease in the relative yield is represented.

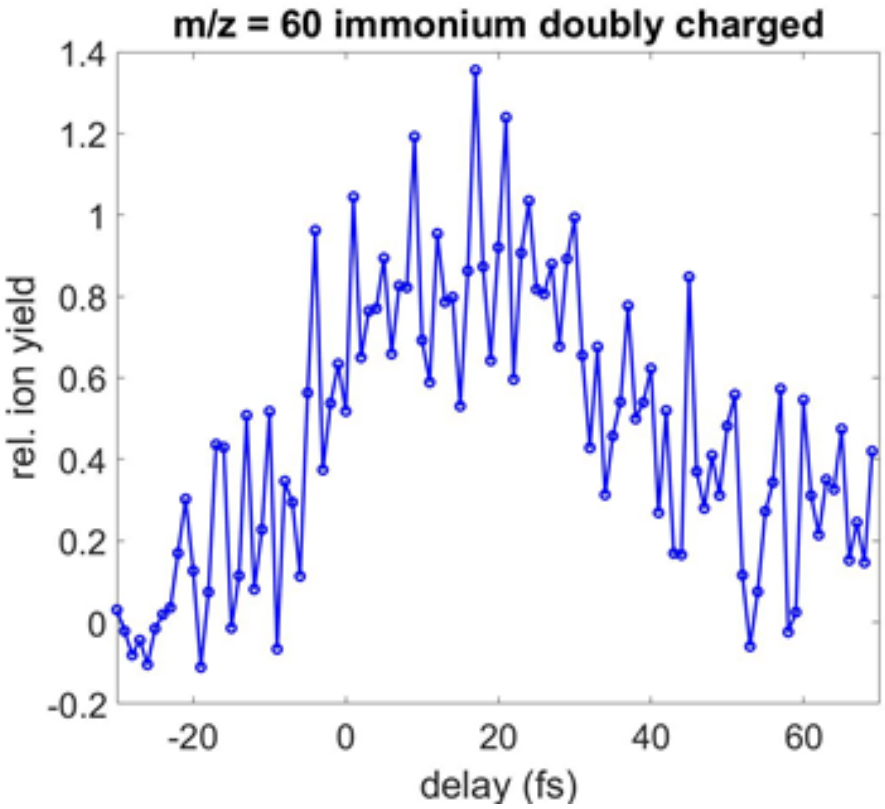

Figure 7.1.2: Pump-probe dynamics of the relative ion yield (eqn. 7.1.1) of the immonium doubly charged ($m/q = 60$) as a function of the pump-probe delay

The results of this experiment are undoubtedly promising even though there are partial differences compared to previous work, but this can be attributed to the different properties of the laser beams.
Even if the results have been surprisingly good, this setup solution cannot be adopted in the long term: in fact, after only few applications the signal showed an abrupt drop related to the collimator clogging. Unexpectedly, even with a $4mm$ aperture the molecules formed a lid shaped deposition that blocked other incoming molecules. This is actually not surprising, if one thinks about the radial expansion of the gas just at the entrance of the collimator and its straight walls that do not allow the correct disposal of unused molecules. As a final remark, instead of changing the geometry downstream the nozzle, it is better to focus on the root cause of the problem, which is represented by the nozzle shape.

Chapter 8

Conclusion and future perspectives

In this thesis work, I have characterized a molecular source for attosecond spectroscopy experiments and analyzed its fluid dynamics through computer simulations.
The experimental characterization has emphasized the main limitations regarding both the spatial and temporal profiles. The radial width has been estimated to be larger than $3.5mm$, revealing an unwanted effusive beam. Furthermore, the decay along the propagation is substantial. The temporal characteristics show that the valve is not able to generate a confined beam to be synchronized with the laser pulses at $1kHz$, revealing a FWHM in the order of $800\mu s$ for an aperture time of the valve of $220\mu s$.
The theoretical analysis has been performed using the DSMC software which has allowed rationalizing the origin of the problems related to the valve design. I have investigated the fluid dynamics of a gas jet by modelling the geometry of the Parker valve both for the CW and pulsed operation modes. A systematic study on the dependence of the molecular density on the skimmer position, input pressure and nozzle temperature has been performed. No significant improvements have been noticed under the conditions here examined, observing always an effusive beam, in line with our experimental observations.
In particular, the radial width improves by increasing the distance between the valve and the skimmer, obtaining, at $10mm$ of distance, a radius of $\approx 3mm$. Nevertheless, the amplitude signal decreases significantly, preventing, in principle, to transport high quantity of sublimated analyte. For what concerns the temporal characteristics, the time duration at $1mm$ from the nozzle the gas flow is almost constant for $400\mu s$, considering a time valve aperture of $220\mu s$.
My simulations suggest that the skimmer could be replaced by a collimator to improve the molecular density at the target and obtain a confined beam. This has been further explored experimentally, but the disadvantage is reflected on its clogging related to the deposition of heavy molecules upon its surface.
Future developments of this work are directed into a refinement of the simulations and its experimental validation. For what concerns the simulations:

1. Other software could be used to validate the current data and explore different conditions (i.e., the unsteady conditions for which the DSMC software poses the greatest challenge), one among all SPARTA (Stochastic PArallel Rarefied-gas Time-accurate Analyzer) Simulator, which is the most updated software.

2. In order to have a more realistic simulation of the problem, the complete geometry of the valve (including for example the components that precede it) could be tested.

Experimentally:

1. The shape of the nozzle seems to be the origin of the problems for both the temporal and spatial spread. A complete re-design should be studied to ensure the production of an effective supersonic gas jet. In this direction, comparing it to other supersonic valves, a miniaturization of some of its component could be beneficial.

The open challenges are many and an accurate exploration is required to stimulate the development of this field of physics.

Appendix

In this appendix the MATLAB code for extracting the data from the video simulation of the valve in unsteady flow (pulsed mode) is reported.

```
n=81; %number of frames
j=1;
frame={}
for i=(15*1):2:(2*(n-1)+15)
   name=strcat('scene00',num2str(i,'%03i'),'.tiff');

   frame{j}=imread(name);
   j=j+1;

end
figure()
imshow(frame{40})

%% scale estrapolate
x1=122;
x2=633;
yconst=420;
scala=frame{10}(yconst,x1:x2,:);

figure()
imshow(scala);
scalay=[1:x2-x1];
n1=19; %log n density start
n2=22; %log n density end
scala_riscalata=rescale(scalay,n1,n2);

xaxis=[1:n];
t1=0.5 %us
t2=53 %us
time= rescale(xaxis,t1,t2);
xtot=[1:n]';
%% choose pixel of interest
x= 629;
y= 149;
pixel_interest={};
for j=1:n
   pixel_interest{j}= frame{j}(y,x,:);
end
%corrisponding values
```

```
numb_density=zeros(n,1);
for j=1:n
    for i=1:size(scala_riscalata,2)
       if pixel_interest{j}(1,1,1)==scala(1,i,1) & ...
          pixel_interest{j}(1,1,2)==scala(1,i,2) & ...
          pixel_interest{j}(1,1,3)==scala(1,i,3)
        posizione=i;
        numb_density(j)= scala_riscalata(1,i);
       end
    end
end


fitobject = fit(xtot,numb_density,'gauss2')
plot(fitobject,1:n, numb_density)
xlabel('time')
ylabel('Number density')
title('pulsed valve (EVEN) as a function of time')

figure()
scatter(1:n,numb_density,'LineWidth',3.5)
xlabel('time [\mus]','FontSize',25)
ylabel('Number density','FontSize',25)
title('pulsed valve (EVEN) as a function of time (single pixel)')
pbaspect([1 1 1])
%% Average over 9 pixel
x= 629;
y= 145;
figure();
imshow(frame{40})
h = drawrectangle('Position',[x-5,y-5,9,9],'StripeColor','r');
%get the rectangle posistion
xtot= h.Vertices(2:3,1);
ytot= h.Vertices(1:2,2);
numb_density_mean=[];
for j=1:n
    m=1;
    numb_density_frame=[];
    for k=xtot(1):xtot(2)
        for l=ytot(1):ytot(2)
            pixel_interest= frame{1,j}(l,k,:);
            for i=1:size(scala_riscalata,2)
                if pixel_interest(1,1,1)==scala(1,i,1) & ...
                   pixel_interest(1,1,2)==scala(1,i,2) & ...
                   pixel_interest(1,1,3)==scala(1,i,3)
                posizione=i;
                numb_density_frame(m)= scala_riscalata(1,i);
                m=m+1;
                break
            end
        end
    end
end
numb_density_mean(j)=mean(numb_density_frame);
```

```
90 end
91
92 figure()
93 scatter(time, numb_density_mean,'LineWidth',3.5)
94 xlabel('time [\mus]','FontSize',25)
95 ylabel('Number density','FontSize',25)
96 title('pulsed valve (EVEN) as a function of time (average over ...
       9x9 pixel)')
97 pbaspect([1 1 1])
```

Bibliography

[1] Laura Abad Toribio et al. "Performance of a solenoid-driven pulsed molecular-beam source". In: *Review of Scientific Instruments* 66 (Aug. 1995), pp. 3826–3832. DOI: 10.1063/1.1145444.

[2] O. Aktas, N.R. Aluru, and U. Ravaioli. "Application of a parallel DSMC technique to predict flow characteristics in microfluidic filters". In: *Journal of Microelectromechanical Systems* 10.4 (2001), pp. 538–549. DOI: 10.1109/84.967377.

[3] Rader D. et al. *Measurements of Thermal Accomodation Coefficients. Sandia National Laboratories*. 2005.

[4] J. B. Anderson and J. B. Fenn. "Velocity Distributions in Molecular Beams from Nozzle Sources". In: *The Physics of Fluids* 8.5 (1965), pp. 780–787. DOI: 10.1063/1.1761320. eprint: https://aip.scitation.org/doi/pdf/10.1063/1.1761320. URL: https://aip.scitation.org/doi/abs/10.1063/1.1761320.

[5] G. A. Bird. "Direct Simulation and the Boltzmann Equation". In: *Physics of Fluids* 13.11 (Nov. 1970), pp. 2676–2681. DOI: 10.1063/1.1692849.

[6] G. A. Bird. "Molecular gas dynamics". In: *NASA STI/Recon Technical Report A* 76 (Jan. 1976), p. 40225.

[7] G. A. Bird. "The Direct Simulation Monte Carlo Method: Current Status and Perspectives". In: *Microscopic Simulations of Complex Flows*. Ed. by Michel Mareschal. Boston, MA: Springer US, 1990, pp. 1–13. ISBN: 978-1-4684-1339-7. DOI: 10.1007/978-1-4684-1339-7_1. URL: https://doi.org/10.1007/978-1-4684-1339-7_1.

[8] G.A. Bird. *Molecular Gas Dynamics and the Direct Simulation of Gas Flows*. Molecular Gas Dynamics and the Direct Simulation of Gas Flows v. 1. Clarendon Press, 1994. ISBN: 9780198561958. URL: https://books.google.it/books?id=Bya5QgAACAAJ.

[9] F. Calegari et al. "Observation of ultrafast electron dynamics in N2 molecules induced by attosecond pulses". In: *CLEO: 2013*. Optical Society of America, 2013, QF2C.5. DOI: 10.1364/CLEO_QELS.2013.QF2C.5. URL: http://www.osapublishing.org/abstract.cfm?URI=CLEO_QELS-2013-QF2C.5.

[10] C Calvert et al. "LIAD-fs scheme for studies of ultrafast laser interactions with gas phase biomolecules". In: *Physical chemistry chemical physics : PCCP* 14 (Feb. 2012), pp. 6289–97. DOI: 10.1039/c2cp23840c.

[11] Darko Dimitrovski et al. "Ionization of oriented carbonyl-sulfide molecules by intense circularly polarized laser pulses". In: *Physical Review. A* 83 (July 2010). DOI: 10.1103/PhysRevA.83.023405.

[12] André T. J. B. Eppink and David H. Parker. "Velocity map imaging of ions and electrons using electrostatic lenses: Application in photoelectron and photofragment ion imaging of molecular oxygen". In: *Review of Scientific Instruments* 68.9 (1997), pp. 3477–3484. DOI: 10.1063/1.1148310. eprint: https://doi.org/10.1063/1.1148310. URL: https://doi.org/10.1063/1.1148310.

[13] Uzi Even. ""The Even-Lavie valve as a source for high intensity supersonic beam"". In: *EPJ Techniques and Instrumentation* 2 (Dec. 2015). DOI: 10.1140/epjti/s40485-015-0027-5.

[14] JB Fenn et al. "Electrospray ionization for mass spectrometry of large biomolecules". In: *Science (New York, N.Y.)* 246.4926 (Oct. 1989), pp. 64–71. ISSN: 0036-8075. DOI: 10.1126/science.2675315. URL: https://doi.org/10.1126/science.2675315.

[15] François Gaie-Levrel et al. "VUV state-selected photoionization of thermally-desorbed biomolecules by coupling an aerosol source to an imaging photoelectron/photoion coincidence spectrometer: Case of the amino acids tryptophan and phenylalanine". In: *Physical chemistry chemical physics : PCCP* 13 (Mar. 2011), pp. 7024–36. DOI: 10.1039/c0cp02798g.

[16] Marc O. Hedahl and Richard G. Wilmoth. *Comparisons of the Maxwell and CLL gas/surface interaction models using DSMC*. NASA STI/Recon Technical Report N. Dec. 1995.

[17] F Hillenkamp et al. "Matrix-assisted laser desorption/ionization mass spectrometry of biopolymers". In: *Analytical chemistry* 63.24 (Dec. 1991), 1193A–1203A. ISSN: 0003-2700. DOI: 10.1021/ac00024a002. URL: https://doi.org/10.1021/ac00024a002.

[18] Eunji Jun. "All-Particle Multiscale Computation of Hypersonic Rarefied Flow for Mars Entry". In: Jan. 2010. DOI: 10.2514/6.2010-822.

[19] George Karniadakis, Ali Beskok, and Aluru NR. *MicroFlows and Nanoflows - Fundamentals and Simulation*. Jan. 2005.

[20] G.J LeBeau and F.E Lumpkin III. "Application highlights of the DSMC Analysis Code (DAC) software for simulating rarefied flows". In: *Computer Methods in Applied Mechanics and Engineering* 191.6 (2001). Minisymposium on Methods for Flow Simulation and Modeling, pp. 595–609. ISSN: 0045-7825. DOI: https://doi.org/10.1016/S0045-7825(01)00304-8. URL: https://www.sciencedirect.com/science/article/pii/S0045782501003048.

[21] Giacinto D. Lucarelli et al. "Novel beamline for attosecond transient reflection spectroscopy in a sequential two-foci geometry". In: *Review of Scientific Instruments* 91.5 (May 2020), p. 053002. ISSN: 1089-7623. DOI: 10.1063/5.0005932. URL: http://dx.doi.org/10.1063/5.0005932.

[22] Mauro Nisoli. "The Birth of Attochemistry". In: *Opt. Photon. News* 30.7 (July 2019), pp. 32–39. DOI: 10.1364/OPN.30.7.000032. URL: http://www.osa-opn.org/abstract.cfm?URI=opn-30-7-32.

[23] Mauro Nisoli et al. "Attosecond Electron Dynamics in Molecules". In: *Chemical Reviews* 117 (May 2017). DOI: 10.1021/acs.chemrev.6b00453.

[24] Günther Paltauf. "Photomechanical Processes and Effects in Ablation". In: *Chemical Reviews* 103.2 (Feb. 2003), p. 053002. ISSN: 0009-2665. DOI: 10.1021/cr010436c.

[25] Parker. *Series 9: Miniature High Speed and Pressure Liquid Dispense Valve*. URL: www.parker.com/precisionfluidics. (accessed: 01.09.2021).

[26] Yu.K. Pilipenko. "Molecular beams and jets". In: *JINR* 141980 (), pp. 1–6.

[27] Giuseppe Sansone et al. "Electron localization following attosecond molecular photoionization". In: *Nature* 465 (June 2010), pp. 763–6. DOI: 10.1038/nature09084.

[28] Haleema Shah. *How a 19th-Century Photographer Made the First 'GIF' of a Galloping Horse*. URL: https://www.smithsonianmag.com/. (accessed: 01.09.2021).

[29] W. Siu et al. "Attosecond control of dissociative ionization of O_2 molecules". In: *Phys. Rev. A* 84 (6 Dec. 2011), p. 063412. DOI: 10.1103/PhysRevA.84.063412. URL: https://link.aps.org/doi/10.1103/PhysRevA.84.063412.

[30] Stefan Stefanov. "On the basic concepts of the direct simulation Monte Carlo method". In: *Physics of Fluids* 31 (June 2019), p. 067104. DOI: 10.1063/1.5099042.

[31] TheProcessPiping. *The Process Piping*. https://www.theprocesspiping.com/introduction-to-needle-valve/, addendum = "Consulted July 27, 2021".

[32] Eleuterio Toro. "Riemann Solvers and Numerical Methods for Fluid Dynamics: A Practical Introduction". In: Jan. 2009. DOI: 10.1007/b79761.

[33] Yoichi Uehara et al. "High Resolution Time-of-Flight Electron Spectrometer". In: *Japanese Journal of Applied Physics* 29.Part 1, No. 12 (Dec. 1990), pp. 2858–2863. DOI: 10.1143/jjap.29.2858. URL: https://doi.org/10.1143/jjap.29.2858.

[34] J. P. Valleau and J. M. Deckers. "SUPERSONIC MOLECULAR BEAMS: II. THEORY OF THE FORMATION OF SUPERSONIC MOLECULAR BEAMS". In: *Canadian Journal of Chemistry* 43.1 (1965), pp. 6–17. DOI: 10.1139/v65-002. eprint: https://doi.org/10.1139/v65-002. URL: https://doi.org/10.1139/v65-002.

[35] Marc J. J. Vrakking. "An iterative procedure for the inversion of two-dimensional ion/photoelectron imaging experiments". In: *Review of Scientific Instruments* 72.11 (2001), pp. 4084–4089. DOI: 10.1063/1.1406923. eprint: https://doi.org/10.1063/1.1406923. URL: https://doi.org/10.1063/1.1406923.

[36] W. C. Wiley and I. H. McLaren. "Time-of-Flight Mass Spectrometer with Improved Resolution". In: *Review of Scientific Instruments* 26 (1955), p. 1150. DOI: 10.1063/1.1715212.

[37] M. S. Woronowicz and D. F. G. Rault. "Cercignani-Lampis-Lord gas-surface interaction model: Comparisons between theory and simulation". In: *Journal of Spacecraft and Rockets* 31.3 (May 1994), pp. 532–534. DOI: 10.2514/3.26474.

[38] R.N. Zare and R.D. Levine. "Mechanism for bond-selective processes in laser desorption". In: *Chemical Physics Letters* 136.6 (1987), pp. 593–599. ISSN: 0009-2614. DOI: https://doi.org/10.1016/0009-2614(87)80524-9. URL: https://www.sciencedirect.com/science/article/pii/0009261487805249.

[39] Ahmed Zewail. *Ahmed Zewail Nobel Lecture*. URL: https://www.nobelprize.org/prizes/chemistry/1999/zewail/lecture. (accessed: 01.09.2021).

[40] I. Znakovskaya et al. "Attosecond Control of Electron Dynamics in Carbon Monoxide". In: *Phys. Rev. Lett.* 103 (10 Sept. 2009), p. 103002. DOI: 10.1103/PhysRevLett.103.103002. URL: https://link.aps.org/doi/10.1103/PhysRevLett.103.103002.